High order harmonic generation at relativistic laser intensities

Vom Fachbereich Physik der Universität Duisburg-Essen zur Erlangung des akademischen Grades eines Doktors der Naturwissenschaften genehmigte

Dissertation

von

Konstantin Lobov

aus

Kiew

Referent: Prof. Dr. D. von der Linde

Korreferent: Prof. Dr. U. Teubner

Tag der mündlichen Prüfung: 03.04.2008

Abstract

This work is devoted to high order harmonic generation (HOHG) on steep plasma density gradients during the interaction of relativistic femtosecond laser pulses with solid density plasma. A qualitative change to the specular reflected HOHG mechanism has been observed when the intensity of the p-polarized excitation pulse increases beyond the relativistic threshold. It has been experimentally verified that harmonic generation takes place in the case of the s-polarized relativistic excitation beam. A wave mixing experiment has been carried out. The behaviour of HOHG efficiency as a function of the scale length is measured. The results of the first three experiments have been explained with the help of the “oscillating mirror” model and the “resonance” mechanism of HOHG which are presented in the first chapter. The recorded dependence of HOHG efficiency on the scale length is qualitatively in good agreement with the predictions of the particle in cell (PIC) simulations.

Acknowledgments

This work concludes one of the most important chapters in my life. However, writing this little section of acknowledgement seems to be much more difficult than I had expected. There are so many people who helped me out in many ways during my graduate school years, that listing them all on a piece of paper would be quite difficult.

First and foremost I should thank Professor Dr. ***von der Linde***. His commitment to mentoring students to become successful scientists in the field allowed me the opportunity to work in a fruitful environment. Without his help and advice, I would not be graduating this term. It was a pleasure for me to work in his group, which in the last few years has became a big second family for me.

I am grateful to my advisor Dr. ***Alexander Tarasevitch***. Alexander has been my mentor for the last five years and it has been a privilege for me to work with him. Whether he believes it or not, I tried my best to be a good student and to cause as little trouble as possible. His care, kindness and his own work pushed me to work harder, helped me to learn and to do what was necessary to perform my work. Without his endless patience and foresight I would never have finished this work.

I'd like to thank ***Michael Bieske, Bernd Proff*** and ***Roland Kohn*** for being my friends, and in particular for their support with software, mechanical and electronic components and devices.

Of course, I cannot forget ***Kay Eibl, Ivan Rajkovic***, ***Uladzimir Shymanovich*** and ***Konstantin Krutitsky*** who looked through this thesis and made numerous suggestions as to how to improve the style and language.

Further, I should show special gratitude to ***Uladzimir Shymanovich*** who held me from doing numerous follies.

I thank all members of the working group for being great colleagues and good friends.

Finally, I have always thought that I could measure someone's success by looking at how successful their friends are. If I still believe that, I am a very successful person and I hope to keep it that way.

Contents

List of Figures

Chapter 0 Introduction

High order harmonic generation (HOHG) in gases is a promising source of the coherent vacuum ultra violet (VUV) and soft X-rays radiation with the wavelength λ down to the nm region [6]. Thus, using the radiation source based on HOHG, the corresponding high spatial resolution can be reached.
In a number of publications HOHG on solid targets is predicted to be a promising tool for attosecond pulse generation [1-3], providing access to temporal resolution down to 10^{-18} s. Moreover, zeptosecond pulses with a pulse length in the order of the Bohr radius and an intensity of 10^{19} W/cm² can be produced according to the theoretical predictions reported in [4,5].
The goal of HOHG based radiation sources is that both high temporal and spatial resolutions can be achieved simultaneously by generation of short x-ray pulses. It is not difficult to imagine the large field of applications in science, medicine and industry for this kind of radiation source.

Impressive progress in laser technology over the last 30 years has played a significant role. The Chirped Pulse Amplification (CPA) technology developed in 1998 made it possible to reach laser intensities in the order of $I \approx 10^{19}$ W/cm² [8]. Nowadays, Table Top Terawatt (T^3) laser systems can be built even in small labs [9]. The Ti:Sa T^3 laser system generates radiation in the near infrared range $\lambda \approx 800$ nm. This radiation can be converted to short wave length radiation by HOHG.

Depending on the radiation intensity, a number of laser-matter interaction regions with qualitatively different physics can be distinguished. To define the first intensity region, the electric field strength of the radiation is compared with the electric field inside the atoms. In the case of hydrogen this field is in the order of 10^9 V/cm which corresponds to the laser intensity of about 10^{16} W/cm². The interaction of laser light with an intensity much weaker (at least three orders of magnitude) than 10^{16} W/cm² with matter can be described in the frame of the perturbation theory. In experiments with laser light intensities comparable to 10^{16} W/cm²,

the perturbation theory is not valid. With these intensities harmonics up to the 300th order are observed in noble gases [6].

To define the next intensity region it is convenient to introduce the normalized vector potential

$$a = \frac{eA}{mc}, \tag{0.1}$$

which is equivalent to the normalized electron quiver momentum P_{osc} of a single electron in the electromagnetic wave

$$a = \frac{p_{osc}}{mc}, \tag{0.2}$$

where A is the vector potential of the laser beam. e, m and c denote the electron charge, the electron mass and the speed of light, respectively.

The relativistic intensity region is defined by the condition: a >1. In the case a ≈ 1 the electron velocity in the laser field is comparable to the speed of light. Thus, the relativistic effects have to be taken into account. To the a = 1 corresponding irradiance is $I\lambda^2 \approx 1.37 \times 10^{18}$ Wcm^{-2}μm², where I is the laser intensity and λ is the wavelength.

The way to reach the relativistic laser intensities (10^{19} W/cm²) is to concentrate the pulse energy (in the order of 1 J) very strongly in all dimensions. This means that the beam has to be focused in a few wavelength spot and the pulse itself should consist of a few optical cycles.

For further consideration of the laser-plasma interaction it is important to distinguish between "overdense" and "underdense" plasma. Plasma is classified depending on the plasma frequency ω_p. This frequency is related to the electron density of the plasma n as follows.

$$\omega_p = \sqrt{\frac{4\pi e^2 n}{m}} \tag{0.3}$$

Using the relation (0.3) one can define the critical plasma density n_c, corresponding to the given laser frequency ω.

$$n_c = \frac{m\omega^2}{4\pi e^2} \qquad (0.4)$$

The plasma is called overdense if $\omega < \omega_p$ (or $n > n_c$) and underdense in the opposite case. In contrast to the underdense plasma - vacuum boundary, the surface of overdense plasma has a high reflection coeficient.

This work deals with coherent HOHG on solid targets. Because of the relativistic incident laser pulse intensity ($a \approx 1$) the thin layer of material on the target surface is already completely ionized before the maximum of a pulse reaches the target. Thus, the pulse itself interacts with highly ionized overdense plasma. HOHG experiments are done in reflection geometry (figure 0.I)

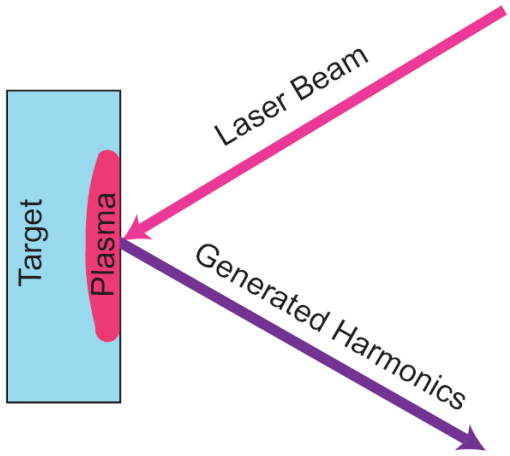

Figure **0.I** Scheme of HOHG experiments in reflection geometry

The physics of the laser-plasma interaction strongly depends on the scale length L[1]. This parameter is the characteristic length which describes how "fast" the electron density drops on the plasma - vacuum boundary. In the experiments discussed in this work the laser plasma

[1] The definition of the scale length L is given in chapter 1.

interaction time is short enough to assume the steep plasma density gradient towards vacuum $L << \lambda$.

During the last three decades significant results have been achieved in this field. First of all numerous experiments on HOHG have been demonstrated [10, 13, 14, 16, 17, 19, 20, 28]. In the same time the "oscillating mirror" model and the "resonant" mechanism which provide the basic understanding of HOHG in two different regimes (the relativistic and non-relativistic regimes, respectively) have been developed [10-14, 18, 21-26, 29]. Moreover with the introduction of the particle in cell (PIC) simulation code the detailed modelling of HOHG on a computer has been made possible [3, 10, 23, 24, 27]. Excellent quantitative agreement between experimental results, PIC predictions and the "oscillating mirror" model has been achieved [10].

HOHG from solid targets was observed for the first time with nanosecond pulses of a CO_2 laser in 1981 [28].

The generation of relativistic high order harmonics during the interaction of a p- and s-polarized, 2.5 ps laser pulse at 1053 nm with a solid target was experimentally verified for intensities up to 10^{19} Wcm^{-2} ($a \approx 2.5$) [17]. High order harmonics up to the 75th order (14.0 nm) were observed. However, because of the long pulse duration and insufficient contrast the laser pulses interacted with already diluted plasma. Thus, the generated harmonics were not collimated.

Supported by PIC simulations and using the 90 fs FWHM pulses with a peak intensity of $I \approx 10^{18}$ W/cm^2 ($a<1$), HOHG up to the plasma frequency were experimentally confirmed. But because of relatively moderate pulse intensity, the attempt to see HOHG with frequencies higher than plasma frequency was not successful [10].

Further experiments on HOHG were presented by A. Tarasevitch et al. [20]. Short laser pulses of 35 fs. and 120 fs. FWHM, with a peak intensity of 10^{18} W cm^{-2} were used to demonstrate the collimated harmonics. Harmonics up to the 45^{th} order were detected. A rapid decrease in the conversion efficiency with the increasing plasma scale length was observed.

The scale length dependence of HOHG efficiency was experimentally investigated [19]. The same dependence was considered with the help of the PIC simulation and the double pulse experiments with much higher resolution, in the range $0.04 < L/\lambda < 0.4$ [10]. Due to the non-

relativistic pulse intensity in latter experiment only part of the PIC predicted HOHG efficiency behaviour could be experimentally verified. Namely the plateau for $0 < L/\lambda < 0.1$ and dramatic decrease of harmonic efficiency with increasing scale length ($L/\lambda \approx 0.15$) was observed. In contrast, the subsequent increase of HOHG efficiency in the region $0.1 < L/\lambda < 0.35$ predicted by the PIC simulation was not verified by the experiment.
Similarly, HOHG with the s-polarized incident pulse could not be observed [10].

Considering the previous experimental results, in particular discrepancies between the analytical models and numerical PIC simulations on the one hand and the experimental results on the other, the necessity for additional experiments is obvious. As mentioned above the moderate intensity of the laser is the main reason for these partly unsuccessful experimental efforts to verify the results of the numerical calculations. Now, relativistic laser pulses with the desired "pulse quality"[1] are available, allowing the theoretical predictions mentioned above to be experimentally verified. Keeping this in mind, the aims of this experimental work are:

- to confirm experimentally the transition to the relativistic regime of HOHG in the case of the p-polarized laser pulse,
- to observe HOHG in the case of the relativistic s-polarized incident beam, and
- to verify the scale length dependence of HOHG efficiency theoretically predicted in [10].

This work consists of three parts.
The first chapter describes the theory of HOHG. The main concepts of the "oscillating mirror" model as well as of the PIC simulation are presented in this chapter. Further, the numerical PIC investigations of HOHG in the non-relativistic regime and the corresponding mechanism are discussed. The numerical (PIC) consideration of the scale length dependence of HOHG efficiency concludes the first chapter. The purpose of this chapter is to explain the basic processes taking place on the surface of the overdense plasma interacting with an intensive laser pulse.

[1] The notion "pulse quality" is explained in chapter 2.

The second chapter describes the 10 Hz. T³ laser system at the "Institut für Experimentelle Physik" (IEP) at the University of Duisburg-Essen. At the beginning of this chapter the T³ laser setup at the IEP is briefly described. Further, the pulses delivered by the laser system are characterised, and the possibility of second harmonic generation (SHG) is considered more closely. The discussion of the adaptive optics system as a part of the T³ laser concludes this chapter.

In the third chapter, the experimental setup, as well as the experiments themselves, together with the experimental results are presented. After a short description of the experimental setup, the experiments concerning HOHG mechanisms in the regimes below and above the relativistic threshold are presented. Further, the experiment providing strong evidence of HOHG during the interaction of the relativistic s-polarized laser pulse with a overdense plasma is discussed. This is followed by a description of the wave mixing experiment. The measured scale length dependence of HOHG efficiency is presented at the end of the third chapter.

Some of the experimental results are already published [16].

Chapter 1 Theory of HOHG

The interaction of a laser with overdense plasma, including collective electron motion, resulting in HOHG can be described by the detailed numerical "particle in cell" (PIC) simulation. In the PIC simulation, the plasma is modelled by the charged "macroparticles", which are the groups of electrons or ions. For a given incident electromagnetic field the equations of motion of the macroparticles combined with the Maxwell equations are numerically integrated.

In contrast to the PIC simulations, the "oscillating mirror" model provides an analytical description of HOHG. In the relativistic regime ($a > 1$) the predictions of the "oscillating mirror" model are in good agreement with the PIC results.

In the non-relativistic regime the "resonant" mechanism of HOHG explains the main observed features of the generated harmonics. Nevertheless the PIC simulations remain the main theoretical tool for providing a quantitative description of HOHG in the non-relativistic regime ($a < 1$).

In this chapter the theoretical description of HOHG is considered.
In the first section of this chapter the "oscillating mirror" model of HOHG is discussed. The second section deals with the numerical consideration of HOHG.

1.1 Oscillating mirror model of HOHG

The analytic description of HOHG while interaction of the relativistic laser pulses with the overdense plasma is provided by the "oscillating mirror" model, a detailed consideration of which can be found in [10 - 13, 21-23, 29,]. This approximation consists of two steps. The first step is to replace the collective electron motion by the motion of the layer with the critical density which has a high reflection coefficient. In the second step the light reflected from this oscillating boundary is calculated. In this section, only the phase modulation of the electromagnetic radiation reflected by the oscillating mirror is taken into account[1]. For further discussion it is useful to consider the special case of the mirror oscillation itself being driven by laser pulses with relativistic intensity. Thus, in this case two incident electromagnetic waves are involved: the "pump" to make the mirror oscillate, and the "probe" to be reflected on it (figure 1.I).

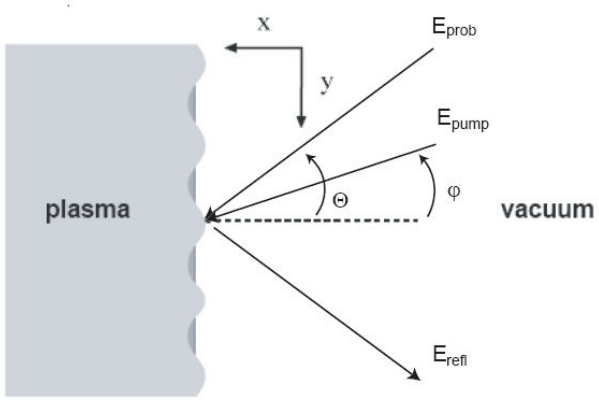

Figure **1.I** Schematic picture of the incident pump E_{pump} and probe E_{prob} beams on the plasma vacuum boundary. The generated harmonics are assumed to propagate in the direction of the reflected beam E_{refl}.

[1] HOHG by the nonlinear oscillating electrons, as well as the influence of the relativistic effects such as velocity dependent mass are not considered here. These effects are discussed in [11, 12, 30].

To get an idea on collective electron motion in the field of a linearly polarized, plane electromagnetic wave with the frequency ω_d and the angle of incidence φ (figure 1.I), it is useful to consider the motion of a single electron under the same conditions.
During one cycle of the field, the electron performs a famous "figure-eight" motion [12, 22, 31] see figure 1.II

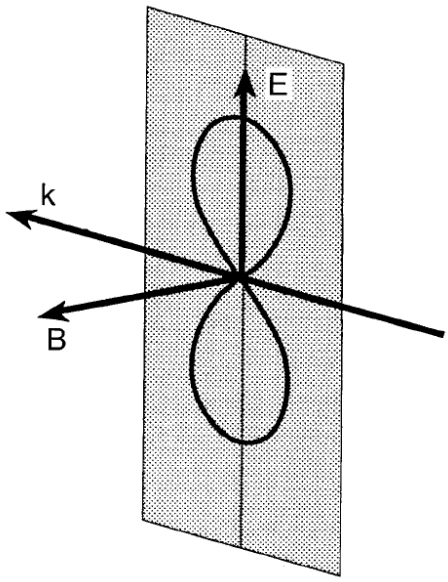

Figure **1.II** "Figure-eight" orbit of a free electron in a linearly polarized plane electromagnetic wave. Figure is taken from [12].

The transverse component of the motion (parallel to the polarization vector, or to the electric field **E**) is oscillating with the frequency of the driving electromagnetic field ω_d, whereas the longitudinal one (in the direction of the wave vector **k**) with $2\omega_d$. Note, that in the non-relativistic case ($a < 1$) the longitudinal component is small compared with the transverse one. Assuming that the collective motion of the electrons near the surface with the critical density is qualitatively similar to that of the single electron, the following conclusions concerning the frequency of the oscillating mirror can be made. Since the electron motion parallel to the critical density surface does not contribute to the oscillation of the mirror, only the electron motion which is normal to it is of interest.
In the case of s-polarized light only the longitudinal component of the "figure-eight" trajectory has a non vanishing projection on the surface normal, see figure 1.III b.

Consequently the mirror will oscillate with the same frequency as the longitudinal component of the "figure-eight" trajectory, namely $\omega_m=2\omega_d$ (Figure 1.IV right).

In the case of p-polarized light both components of the electron motion have non vanishing projection on the surface normal, see figure 1.III a. Thus, the electron boundary is driven at frequencies ω_d and $2\omega_d$ (Figure 1.IV left). Because of the non-relativistic case (a = 0.2) presented in figure 1.VI (left) the longitudinal component of the electron motion is negligible. Thus only the plasma density oscillations with the frequency ω_d can be observed.

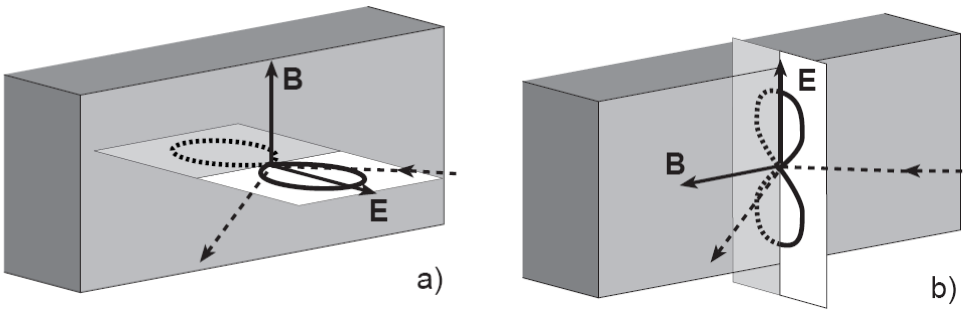

Figure **1.III** Directions of the electric and magnetic fields and the "figure-eight" orbit of an electron: a) for the p-polarized light, b) for the s-polarized light. The dashed arrows indicate the propagation direction of the incident and the reflected light. Figure is taken from [13].

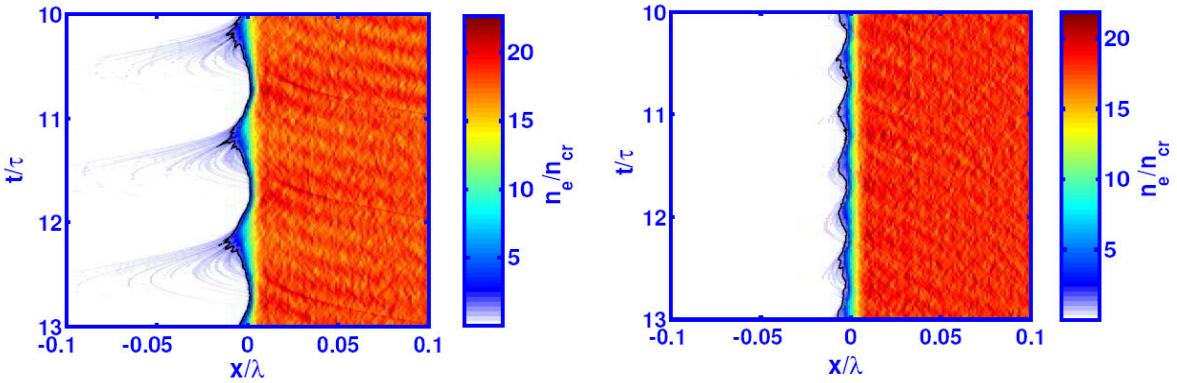

Figure **1.IV** PIC calculated temporal development of the electron density. The plasma oscillations are excited with the p-polarized (left) and the s-polarized (right) beams. PIC parameters are: $n/n_c = 18.6$, $L/\lambda = 0$, angle of incidence $\Theta = 45°$, a = 0.2 left and a = 0.5 right. The critical density layer is shown by the black line. The x axis is normal to the plasma surface, Time t is normalized by the optical period of the laser τ. Figure is taken from [10].

The equation of motion provides more detailed insight into the electron movement close to the plasma-vacuum boundary which is driven by the total electric and magnetic fields of the incident and reflected waves.

$$\frac{d(m\gamma \mathbf{v})}{dt} = -e\mathbf{E}_l - e\mathbf{E} - \frac{e}{c}\mathbf{v}\times\mathbf{H} = \mathbf{F}_p + \mathbf{F}_{em} \tag{1.1}$$

Here **v** is the electron velocity, $\gamma = (1 - v^2/c^2)^{-1/2}$ is the Lorentz factor, $\mathbf{E}_l$ is the longitudinal electric field and $\mathbf{F}_p$=-e $\mathbf{E}_l$ is the Coulomb force between the electrons and the ions. In the non-relativistic limit the absolute value of this force is $F_p = um\omega_p^2$. Here u is the electron excursion from the equilibrium position. Assuming $\omega_d << \omega_p$, the equation of motion (1.1) reduces to the equation of a driven harmonic oscillator

$$\frac{d^2}{dt^2}u + \omega_p^2 u = \frac{F_{em}}{m}, \tag{1.2}$$

which has a well-known solution $u(\omega_d)$

$$u(\omega_d) = \frac{F_{em}(\omega_d)}{m(\omega_p^2 - \omega_d^{\,2})}. \tag{1.3}$$

The resulting normalized oscillation amplitudes of the reflecting surface are:

$$\frac{u_0}{\lambda} = \frac{1}{\pi}\left(\frac{\omega_d}{\omega_p}\right)^2 a\,\tan\varphi\cos\varphi \tag{1.4}$$

in the case of p-polarized incident beam, and

$$\frac{u_0}{\lambda} = \frac{1}{\pi}\left(\frac{\omega_d}{\omega_p}\right)^3 a^2(\cos\varphi)^4 \tag{1.5}$$

for the s-polarization where φ is the angle of incidence.

Here the coordinate system is defined in a way, that x-direction is normal to the plasma surface (see figure 1.I) and the wave vector $\mathbf{k}_d$ of the pump beam is given by

$$\mathbf{k}_d=(k_d\cos\varphi, k_d\sin\varphi, 0) \tag{1.6}$$

To simplify the calculation in this section, the surface deformation u(t, y) in the x direction is assumed to be harmonic and is given by:

$$u(t, y) = u_0\sin(\omega_m(t-\frac{y}{c}\sin\varphi)) \tag{1.7}$$

The equation (1.7) takes into account a variation of the electromagnetic force parallel to the surface, which causes surface deviation in the form of a travelling wave in the y direction.

Having described the mirror oscillation, the reflection on it will be considered more closely. For the incident probe plane electromagnetic wave the geometry shown in figure 1.V is chosen.

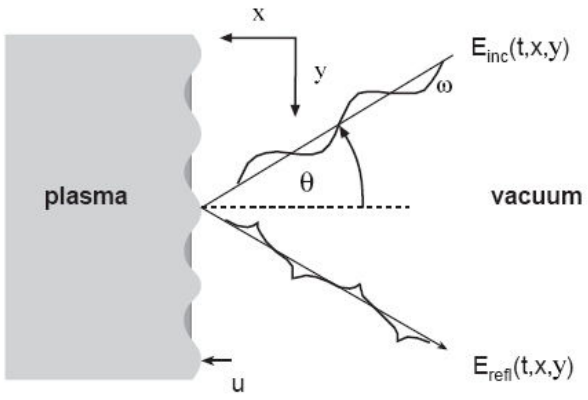

Figure **1.V** Schematic picture of the incident probe light E_{inc} on the plasma vacuum boundary. The reflected radiation E_{refl} propagates away from the plasma. Figure is taken from [13].

In this case, the electric field $E_{inc}(t,x,y)$ of the incident p-polarized wave is given by

$$E_{inc}(t,x,y) = E_0 \exp(-i\omega(t - \frac{x}{c}\cos\Theta - \frac{y}{c}\sin\Theta)) \tag{1.8}$$

The origin of the harmonics can be explained using two simplifying assumptions. First, the reflected beam can be described as a plane wave propagating in the specular direction. Second, the surface is totally reflective.
The electric field of the reflected wave can be obtained under the condition that the total electric field vanishes on the reflecting surface:

$$E'_{inc}(t,u(t,y),y)+E'_{ref}(t,u(t,y),y)=0 \tag{1.9}$$

This condition is valid in the frame moving with the mirror. The same condition transformed in the laboratory frame can be written in a form [21]

$$E_{ref}(t,u,\mathbf{v},y) = -\frac{1-\mathbf{v}/c}{1+\mathbf{v}/c} E_{inc}(t,u,y) \tag{1.10}$$

Note that the amplitude of the reflected beam is dependent on the velocity of the reflecting mirror $\mathbf{v}(t)$. Thus, the resulting electric field of the reflected wave is

$$E_{ref}(t,\mathbf{v},x,y) = -E_0(\mathbf{v})\exp(-i\omega(t + \frac{x}{c}\cos\Theta - \frac{y}{c}\sin\Theta - \frac{2u_0}{c}\cos\Theta\sin(\omega_m(t - \frac{y}{c}\sin\varphi)))) \tag{1.11}$$

Using the Jacobi expansion (1.12)

$$e^{-iz\sin(\omega t)} = \sum_{h=-\infty}^{\infty} J_h(z) e^{-ih\omega t}\,, \tag{1.12}$$

the expression for the reflected electric field E_{ref} can be written as follows:

$$E_{ref}(t,\mathbf{v},x,y) = E_0(\mathbf{v})\sum_{h=-\infty}^{h=\infty} J_h(\chi)\vartheta_h(x,y)\exp(-it(\omega + h\omega_m)) \qquad (1.13)$$

Here $J_h(\chi)$ is the Bessel function of the h^{th} order,

$$\chi = -\omega\frac{2u_0}{c}\cos\Theta \qquad (1.14)$$

and

$$\vartheta_h(x,y) = \exp(-i\omega(\frac{x}{c}\cos\Theta - \frac{y}{c}\sin\Theta) + ih\omega_m\frac{y}{c}\sin\varphi)\,. \qquad (1.15)$$

From the equation (1.13) it is clear, that the electric field of the reflected beam is a superposition of the copropagating plane waves with the frequencies $\omega+h\omega_m$. h is an integer. The polarization of the reflected beam remains the same as that of the probe electromagnetic wave.

In the special case, when one incident beam drives the mirror oscillations and is simultaneously reflected on it the following is valid:

$\Theta=\varphi$,
harmonics propagate in the specular direction,
$\omega_m = \omega$ in the case of p-polarized wave and
$\omega_m = 2\omega$ in the case of s-polarized wave.

It should be mentioned that oscillating surface charges, even without any probe beam, emit the p-polarized radiation at the multiple of the mirror oscillation frequency ω_m, [11, 12, 23].

Now we will consider the case when the wave vectors of the pump and probe beams are not parallel. In this case the generated harmonics are scattered on the travelling wave which is produced by the pump pulse on the plasma surface [29]. According to the calculation shown in [29] the diffraction angle α_h of the h^{th} harmonic is given by the "rainbow equation"

$$\sin\alpha_h = \frac{1}{1+\frac{h\omega_m}{\omega}}\sin\Theta + \frac{\frac{h\omega_m}{\omega}}{1+\frac{n\omega_m}{\omega}}\sin\varphi\,. \qquad (1.16)$$

According to the angular distribution (1.16) the direction of high order harmonics ($h \to \pm\infty$) approaches the specular direction of the pump beam.

$$\alpha_h \xrightarrow[h\to\pm\infty]{} -\varphi \qquad (1.17)$$

The positive (h>0) harmonics are scattered in the angular range between the angles of the reflected pump and probe beams, as shown in figure 1.VI. Moreover, the condition $0 \le |\sin\alpha_h| \le 1$ leads to the so-called shadowed orders. The shadowed orders are the orders h which do not appear. The interval of the shadowed orders is limited as follows:

$$-\frac{1+\sin\Theta}{1+\sin\varphi} < h\frac{\omega_m}{\omega} < -\frac{1-\sin\Theta}{1-\sin\varphi} \qquad \text{if } \varphi < \Theta \qquad (1.18\text{ a})$$

$$-\frac{1-\sin\Theta}{1-\sin\varphi} < h\frac{\omega_m}{\omega} < -\frac{1+\sin\Theta}{1+\sin\varphi} \qquad \text{if } \varphi > \Theta \qquad (1.18\text{ b})$$

One calculated example of the harmonic angular distribution of the probe reflected radiation is shown in figure 1.VI. The pump beam with λ=800 nm and intensity in the order of 3.5 10^{18} W/cm² is incident on the plasma surface at an angle of $\varphi = \pi/8$. The probe beam is taken at λ=260 nm with an intensity of 3.5 10^{14} W/cm² and the angle of incidence $\Theta=\pi/4$. The law of reflection is still valid for the reflection of the probe beam $|\alpha_0| = \Theta$.

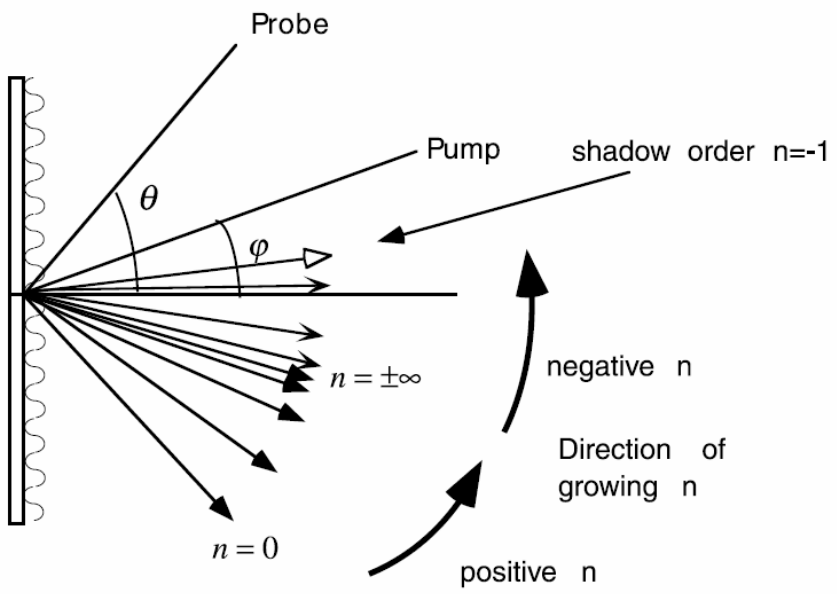

Figure **1.VI** Calculated angular distribution of the generated high order harmonics. The parameters of the incident beams are: pump beam λ = 800 nm, I = 3.5 10^{18} W/cm², $\varphi = \pi/8$; probe beam λ = 260, I = 3.5 10^{14} W/cm², $\Theta = \pi/4$. Figure is taken from [29].

The main features of HOHG in the relativistic regime can be summarized as follows.
In the relativistic regime HOHG described by the "oscillating mirror" model dominates. HOHG in this regime is based on the relativistic Doppler effect. In this regime HOHG occurs in cases of the s- and p-polarized excitation beams. The harmonics are generated in the region close to the plasma layer with the critical electron density. The spectrum of the generated high order harmonics is not limited by the plasma frequency ω_p. The propagation direction of the high order harmonics approaches the specular direction of the pump beam.

1.2 Numerical consideration of HOHG

This section is dedicated to the numerical treatment of HOHG.
At the beginning the main ideas and concepts of the PIC simulation are presented. Then HOHG in the non-relativistic regime is discussed. Finally, the scale length dependence of HOHG is considered more closely.

1.2.1 PIC simulations

Particle in Cell code (PIC) is a very powerful and direct numerical tool for researching and modelling laser-plasma interaction [23, 27]. In the PIC simulation collective behaviour of charged plasma particles is represented by a large number of charged "macroparticles" which obey the equations of motion. Macroparticles consist of a fixed number (100 – 1000) of electrons or ions.

In the numerical calculation the physical quantities such as charge or the strength of the electric field are calculated on the discrete greed positions in space x_i. The exact positions of the macroparticles x_j, in general, are different from the greed points positions. Thus, two sets of points in space have to be distinguished: the position of the space greed points x_i and the exact position of the macroparticles x_j.

The basic cycle of the PIC algorithm consists of four steps (figure 1.VII).

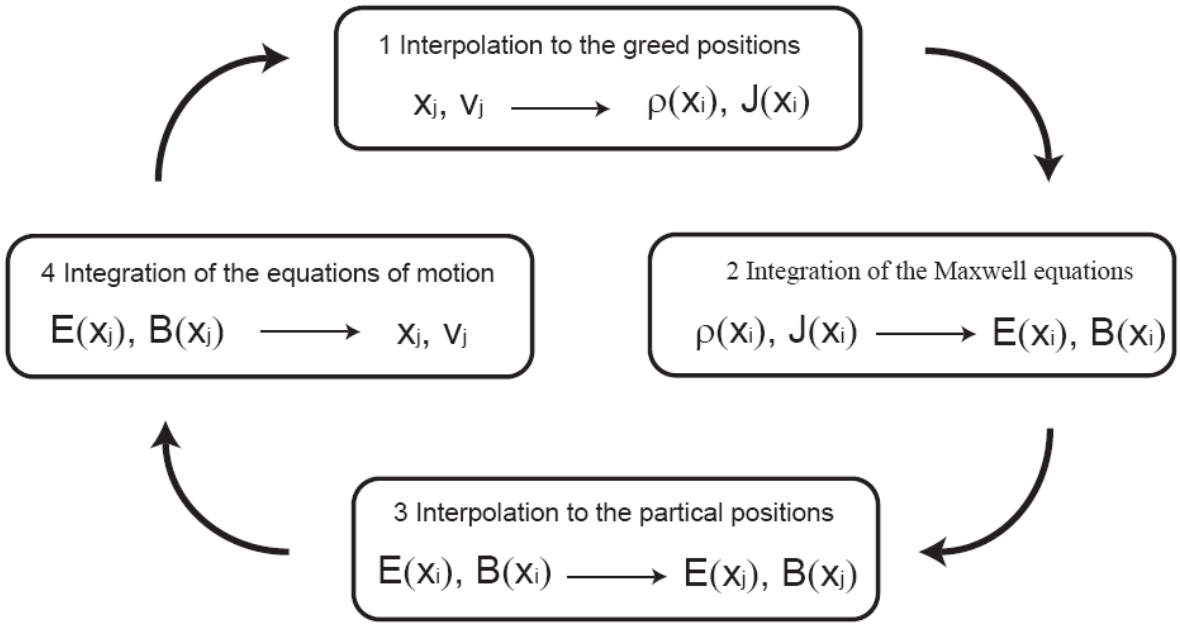

Figure **1.VII** Principal scheme of the basic PIC algorithm. x_j, v_j are the space coordinates and the velocities of the macroparticles, respectively. x_i is the position of the space greed points.

In the first step, the charge $\rho(x_j)$ and current $j(x_j)$ densities caused by the macroparticles are interpolated to the discrete i^{th} grid positions $\mathbf{x}_i$ in space.

In the next step the total electric $E(x_i)$ and magnetic $B(x_i)$ fields on the space grid are obtained by superimposing the fields of the incident electromagnetic wave and that generated by the macroparticles. The latter is calculated with the help of the Maxwell equations, using charge and current densities calculated in the first step.

Further, the fields are interpolated from the discrete space grid positions x_i to the macroparticles positions x_j.

In the last step the equations of motion are integrated to obtain the new positions x_j and velocities v_j of the macroparticles after small time interval Δt.

The time interval should be kept short enough to resolve the highest frequency of interest.

All physical effects on the scale smaller than the size of the space grid are neglected. Since a large number of electrons or ions are considered as a single macroparticle, only the collective behaviour of plasma is taken into account. The finite space resolution Δx and the demand for the numerical stability of the algorithm define the condition on the thermal velocity $\mathbf{v}_{th}$ of the macroparticles at the beginning

$$\mathbf{v}_{th} / \omega_p > \Delta x \qquad (1.19)$$

The expression on the l.h.s. of (1.19) is known as the Debye length ($\lambda_D = \mathbf{v}_{th} / \omega_p$). Debye length is the distance over which the electric field of an individual charge is shielded out by the response of the surrounding charges.

A significant reduction of the calculation time can be achieved using the symmetry properties of the problem. In the case of laser-plasma interaction at normal incidence the 6-dimensional (3 velocity and 3 spatial dimensions) problem in the phase space can be reduced to the 4-dimensional one, with 3 velocity and 1 spatial dimension. The more general situation of an arbitrary incidence angle can be reduced to the normal incidence using the Lorenz transformation [10, 11, 22, 23].

All PIC-simulation results used in this work were obtained by A. Tarasevitch and C. Dietrich exploiting the 4-dimensional PIC-code LPIC [10, 16,].

The geometry shown in figure 1.VIII was used in the PIC simulations.

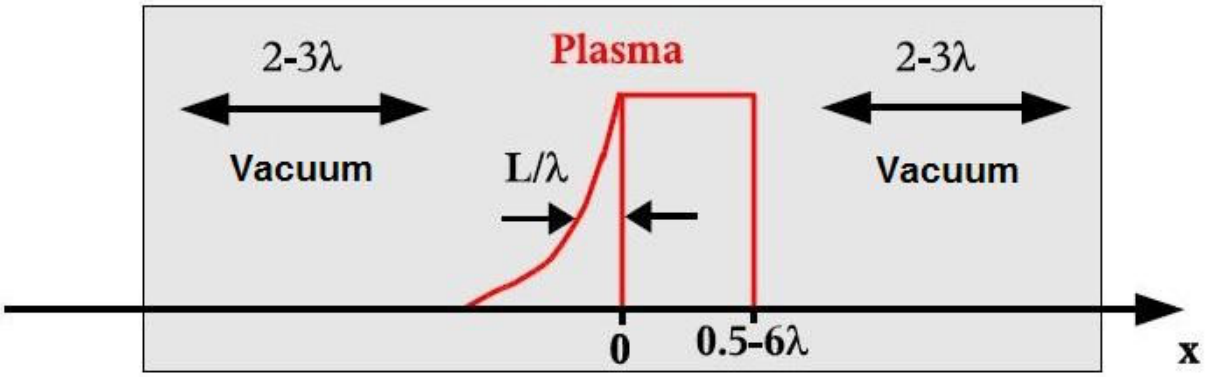

Figure **1.VIII** Geometry of the PIC simulation box with one spatial dimension. The leaser pulse propagates from the left towards the plasma. The plasma density profile is plotted in red. Figure is taken from [10].

In the simulation box (figure 1.VIII) which consists of a large number of cells the laser pulse propagates from the left towards already existing plasma. The plasma density profile (in figure 1.VIII red) includes homogeneous and inhomogeneous regions. The inhomogeneous region of the plasma is described by the exponential function

$$n = n_{max} \exp\left(\frac{x}{L}\right), \tag{1.20}$$

and is characterized by the scale length L. Here n_{max} denotes the maximal plasma density. The exponential density profile represents the self-consistent solution of the isothermal expansion of the plasma in vacuum [33]. The scale length parameter L can be written as:

$$L = \left(\frac{\partial n}{\partial x}\frac{1}{n}\right)^{-1} \tag{1.21}$$

The homogeneous layer of the plasma should be chosen thick enough to ensure that the excitation radiation does not penetrate through the plasma.

In general, considering the numerous HOHG publications based on, or using PIC calculations, and in particular the number of PIC results presented in this work, the importance of the PIC simulation in this field of physics does not need to be emphasized additionally.

1.2.2 Non-relativistic regime of HOHG

HOHG in the non-relativistic regime (a<1) by reflection of the p-polarized laser beam from an overdense plasma has been observed for more than 30 years [34-38]. The "oscillating mirror" model which provides good quantitative results in the relativistic regime[1] [10, 12, 23] can not explain HOHG in the non-relativistic case without additional assumption on the mirror oscillation and plasma density. In the non-relativistic regime the oscillations amplitude of the reflecting surface in the case of dense plasmas ($n/n_c > 10$) is negligible. Thus, the "oscillating mirror" model predicts no, or only weak HOHG [23, 25]. However, the experimental results and PIC simulations in this regime reveal strong HOHG in the case of the p-polarized excitation pulse. The detected and PIC predicted high order harmonics in this regime experience a cut off at the plasma frequency ω_p [10, 16, 37]. There is no evidence yet of HOHG in the case of excitation with the non-relativistic s-polarized pulse [23, 10].

In the year 1982 B. Bezerrides proposed the model of HOHG which is based on the non-relativistic electron fluid model [26]. He assumed the step-like plasma density profile, and calculated the analytical solution for the oscillation amplitude and the acceleration of the electron fluid element oscillating around the plasma boundary. In the next step the emitted radiation is calculated with the help of the Lamor formula. The spectrum of the calculated radiation reproduces nicely the typical properties of the spectra measured in HOHG experiments. The quantitative predictions are in a good agreement with the experimental results in the case of the low plasma density ($n / n_c \approx 5$). In dense plasmas ($n / n_c > 50$) the scale length ($L > 0$) has to be taken in to account.
Analysing the results of the PIC calculations C. Dietrich generalized the Bezerrides model to the case of the limited scale length and proposed the "resonant" mechanism[2] of HOHG [10]. The "resonant" mechanism of HOHG consists of two processes. In the first process the plasma electron density oscillations with the corresponding local plasma frequencies ω_{loc} are

[1] The transition from the non-relativistic to the relativistic regime of the HOHG depends not only on the normalized vector potential a, but also on the electron density n and the scale length L. The scale length dependence is considered in the sections 1.2.3 and 3.4. The condition a > 1 is only a rough estimation for this transition.
[2] In his thesis C. Dietrich refered to this mechanism as „Verstärkte Emission".

resonantly excited. In the second process these plasma density oscillations generate high order harmonic radiation.

For the illustration of the "resonant" mechanism of HOHG the flat plasma surface with $L << \lambda$ and $\omega < \omega_p$ irradiated by the non-relativistic p-polarized laser light at the incidence angle $\Theta = 45°$ is considered (figure 0.I). In the electric field of the incident electro-magnetic wave the electrons of the interacting plasma are periodically accelerated with the optical frequency of the laser ω. The movement of the relatively heavy ions, in comparison with the movement of the electrons is negligible. Thus, the ions can be considered here as a static positive background. The numerically calculated temporal development of the normalized electron density n is shown in figure 1.IX. The x axis is normal to the plasma surface and points in the direction of the high plasma densities. The time t is normalized by the optical period of the incident wave τ.

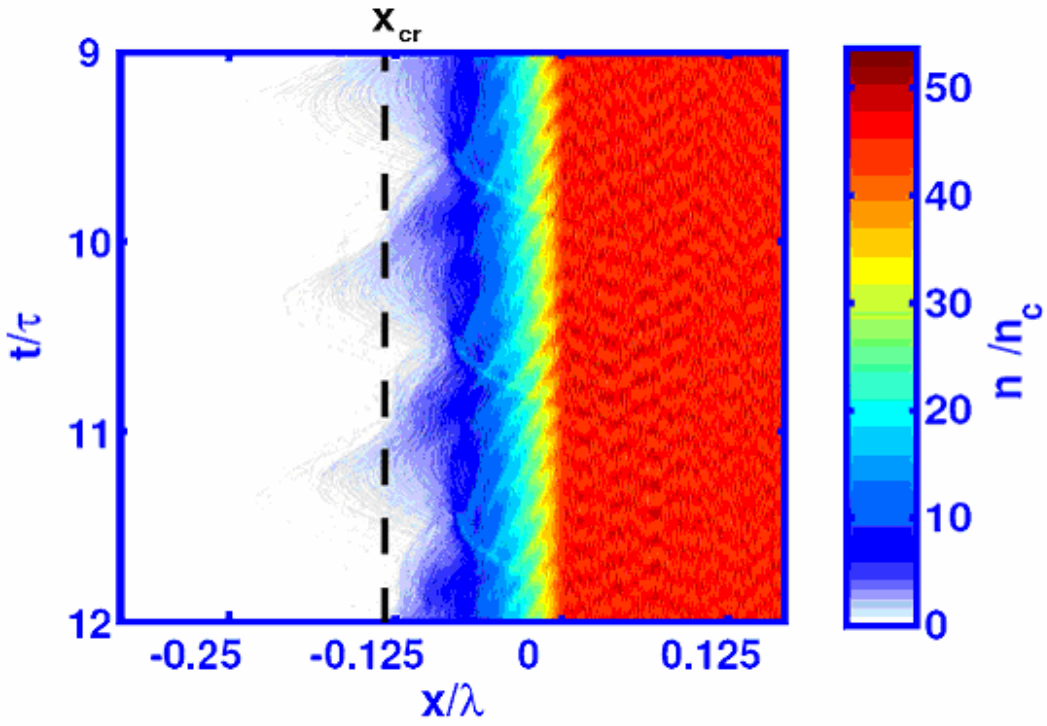

Figure **1.IX** Temporal development of the normalized electron density. The time t is normalized by the optical period τ. The plasma average position of the layer with the critical density is shown by the dashed line. The PIC parameters are: $n_{max}/n_c = 45.56$, $L/\lambda = 0.04$, $a = 0.3$, angle of incidence $\Theta = 45°$, p-polarized excitation pulse. Graph is taken from [10].

The occurred oscillation amplitude of the layer with the critical density $\delta x/\lambda \approx 0.04$ is comparable to the scale length parameter $L/\lambda = 0.04$. This oscillation causes the strong periodical compression and dilatation of the inhomogeneous plasma density region. This happens each period of the incident electromagnetic wave. The compression results in the generation of the strong positive longitudinal electric field E_x. Half a period later the plasma dilates resulting in the generation of the negative longitudinal electric field. The electrostatic fields at the different time points τ, together with the normalized electron density n/n_c are plotted in figure1.X. The time τ is normalized by the optical period of the laser field τ_0. The electric fields are normalised by the quantity $E_r = m\omega ce^{-1}$.

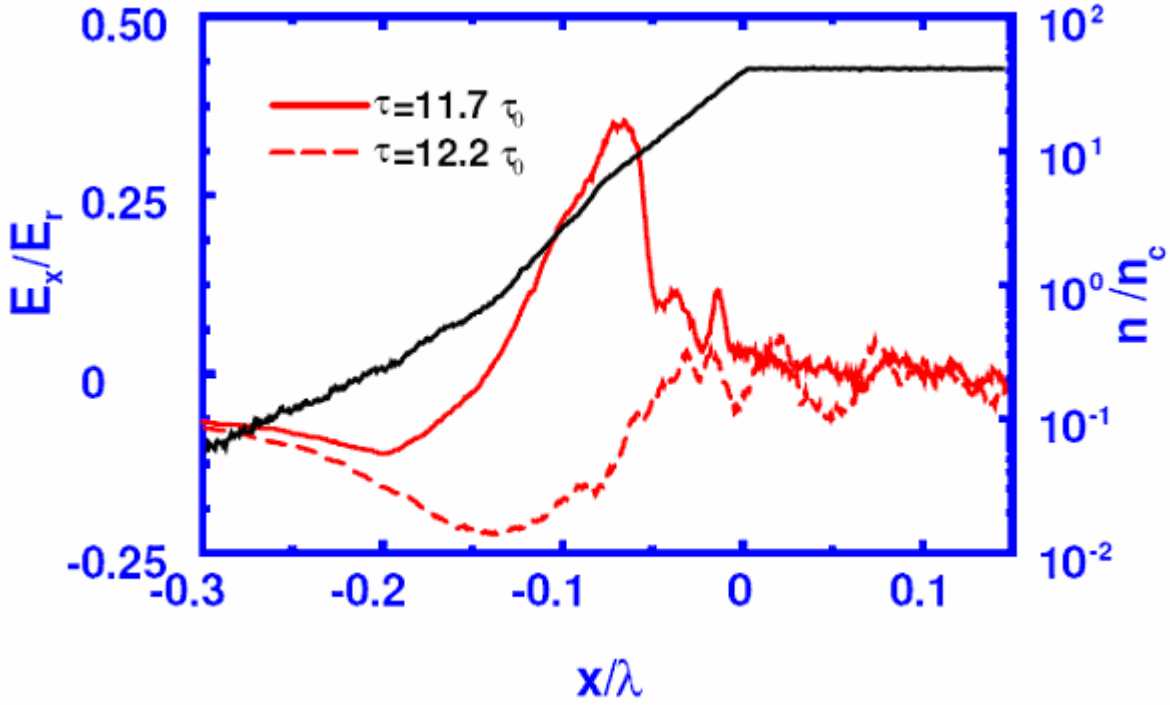

Figure **1.X** PIC calculated electrostatic fields E_x/E_r (red) at the time τ/τ_o=11.7 and τ/τ_o=12.2. The x-axis is normal on the plasma surface and points in the plasma direction. The parameters are: n_{max}/n_c =45.56, L/λ=0.04, a=0.3, p-polarized excitation pulse, angle of incidence Θ=45°. The electron density profile $n(x)/n_c$ is plotted in black. Figure is taken from [10].

The periodic electrostatic field excites the plasma oscillation in each point of the inhomogeneous plasma at the corresponding local plasma frequency ω_{ploc}. In particular, the

resonant plasma oscillations at the multiple of the laser frequency are efficiently excited ($h\omega = \omega_{h,ploc}$), where the constant "h" is a positive integer number.

The generation mechanism of harmonic radiation by the plasma oscillations in the inhomogeneous plasma region can be considered as a temporal reversal of the "resonance absorption" [39 - 41]. It can be shown, that in the case of inhomogeneous plasma ($\nabla n \neq 0$), under certain conditions, the transverse electromagnetic and longitudinal electrostatic waves couple to each other (see [41] and Appendix A1). In the density layer with the satisfied resonance $\omega_h = \omega_{h,ploc}$ and phase matching $\mathbf{k}_h = \mathbf{k}_{h,ploc}$ conditions it provides an efficient way of converting a localized electrostatic (plasma) wave into the electromagnetic one with the optical frequency ω_h, i.e. the generation of the h^{th} harmonic. $\mathbf{k}_h$ and $\mathbf{k}_{h,ploc}$ are the wave vectors of the h^{th} harmonic and the local plasma wave, respectively.

Thus according to the "resonant" mechanism of HOHG the incident electromagnetic wave compresses and dilates periodically the plasma with the frequency ω. This compression results in the longitudinal electric field which excites the plasma oscillations throughout the density profile. In particular the plasma oscillations with the local plasma frequency being in resonance with the optical wave $h\omega = \omega_{h,ploc}$ are strongly excited. The plasma waves in turn generate the high order harmonic with the corresponding frequency $\omega_h = \omega_{h,ploc}$.

The same mechanism[1] was described by F. Quéré et al. [25] from a different point of view.

In conclusion of this section the important features of the discussed (non-relativistic) regime of HOHG are summarized. HOHG described by the "resonant" mechanism dominates in the non-relativistic regime. The origin of HOHG can be associated with the nonlinear plasma density motion and the current enhancement at the local plasma frequency. In contrast to the relativistic regime, harmonics are generated in the plasma layers with $n > n_c$. Detailed numerical investigations reveal that each high order harmonic (h^{th}) is generated in a layer with the corresponding local plasma frequency $\omega_{h,ploc} = \omega_h$ [10, 25]. Because of $\omega_{loc} \leq \omega_p$, the frequencies of the generated harmonics are limited by the plasma frequency $\omega_h \leq \omega_p$. Further, according to the PIC calculation and the mechanism discussed above, no HOHG in the non-relativistic regime occurs in the case of the s-polarized excitation beam [10, 25].

[1] F. Quéré referred to it as the coherent wake emission (CWE) mechanism.

1.2.3 Scale length dependence of HOHG

The dependence of HOHG on the normalized scale length L/λ was extensively investigated experimentally and with the help of PIC simulations [10, 16]. In these works the set of PIC parameters is matched to the real experimental conditions, making a direct comparison of the PIC results with the experimental data possible[1]. Further consideration of HOHG dependence on the scale length in the case of the p-polarized excitation pulse is based on references [10 and 16].

In this work the exponential electron density profile on the vacuum plasma boundary is assumed, see (1.20). In the plasma interaction with the intense (a =0.3), p-polarized laser light two scale length regions with qualitatively different mechanisms of HOHG can be distinguished.

HOHG in the cases of three different scale lengths: column a) L=0, column b) L=0.02 and column c) L=0.2 is illustrated by the results of the PIC simulation (figure 1.XI). The upper and middle panels show the spatial distribution of the electron density oscillations and of their Fourier spectra, respectively. The lower panel depicts the corresponding harmonic spectra. The red circles (bottom right graph) represent the spectrum calculated with the help of the "oscillating mirror" mode for the $s / \lambda = 0.06$. The plasma density increases from zero up to the solid density for $x / \lambda \geq 0$. The dashed lines mark the position of the layer with critical electron density (middle graphs) and of the plasma frequency (bottom graphs), respectively.

[1] The electron density used in PIC calculations in [10] is: $n/n_c=45.56$, and in [16] is $n/n_c=49$,

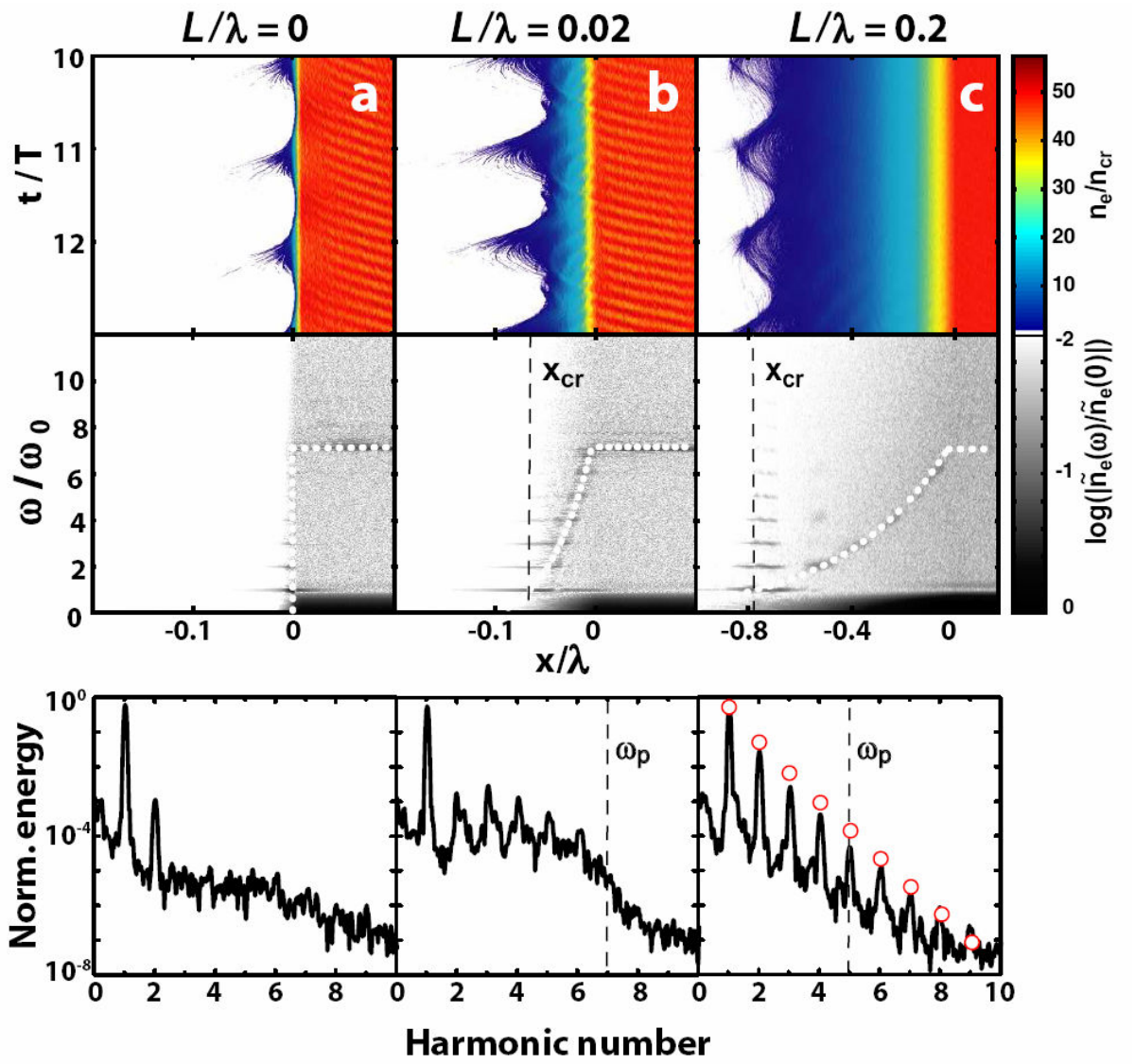

Figure **1.XI** Electron density (top), spectra of the electron density (middle), and harmonic spectra (bottom). PIC parameters are: a = 0.3, $n/n_c = 49$, p-polarized excitation beam. The red circles (bottom right graph) represent the spectrum calculated for a harmonically oscillating mirror with $s/\lambda=0.06$. The dashed lines indicate the critical surface (middle graphs) and ω_p (bottom graphs). White dotted lines represent the local plasma frequency $\omega_{ploc}(x)$. Figure is published in [16].

The results of the numerical investigations of HOHG dependence on the scale length can be summarized as follows.

L = 0

In the limit of $L \to 0$, the electron density profile can be described by a step function. The modulation of the plasma surface is quite weak because the restoring forces in the high density plasma are exceedingly strong (figure 1.XI, left column, upper graph). Thus, the "oscillating" mirror mechanism is inefficient.
There are also no plasma layers with the local critical density corresponding to the harmonics of the incident wave. Thus, the "resonant" mechanism of HOHG does not work. In this case HOHG is inefficient (figure 1.XI, left column, bottom graph). The harmonic sources are centered in the plane x = 0 (figure 1. XI, left column, middle graph)

$0 \le L/\lambda \le 0.09$:

For this scale length region the oscillation of the surface electrons is strongly anharmonic (figure 1.XI, middle column, upper graph). The amplitude of the oscillation s_0 is comparable to the scale length L. Further, the sources of the different harmonic frequencies are located at layers with the corresponding local plasma densities (figure 1.XI, middle column, middle graph). The spectrum of the harmonics exhibits the typical for the non-relativistic regime of HOHG cut-off at the plasma frequency ω_p (figure 1.XI, middle column, bottom graph). Thus, in this scale length region HOHG in the non-relativistic regime dominates. In this case it is also useful to compare the scale length with the penetration depth of the laser wave in the plasma which is defined by the skin depth δ.

$$\delta = \frac{c}{\omega_p} = \frac{\omega}{\omega_p}\frac{\lambda}{2\pi}. \qquad (1.22)$$

The normalized skin depth is consequently:

$$\frac{\delta}{\lambda} = \frac{\omega}{\omega_p}\frac{1}{2\pi} \tag{1.23}$$

The normalized skin depth ($\delta/\lambda = 0.023$) in this region is comparable with the scale length L. Here the plasma density is assumed to be $n/n_c = 49$ and consequently $\omega/\omega_p = 1/7$.

$L/\lambda \approx 0.9$

At this intermediate scale length only weak harmonics are generated. The efficiency of HOHG drops by orders of magnitude (figure 1.XII). Here HOHG in the non-relativistic regime is suppressed because the light can not penetrate deep enough into the plasma.

$0.09 \leq L/\lambda \leq 0.35$

In the last investigated scale length region the electron density modulation appears to be nearly harmonic. Remarkable is the relatively large oscillation amplitude of ca. 6% of the laser wavelength (figure 1.XI, right column, upper graph). The locations of harmonics generation are now centered around the plasma layer with the critical density (figure 1.XI, right column, middle graph). The PIC calculated spectrum is very similar to the spectrum provided by the "oscillating mirror" model (figure 1.XI, right column, bottom graph). Thus, in this scale length region the relativistic regime of HOHG dominates.

The calculated scale length dependence of the fourth and fifth harmonics efficiency are shown in the graph 1.XII. For $L/\lambda < 0.8$ the "resonance" mechanism of HOHG dominates. The efficiency grows slowly with L. This mechanism is suppressed around $L/l \approx 0.09$, because the light can no longer penetrate deep enough into the plasma. As a result, the harmonic efficiency drops and reaches a minimum. With a further increase of L, the relativistic mechanism comes into play and dominates for $L/\lambda > 0.1$, being only weakly dependent on the scale length.

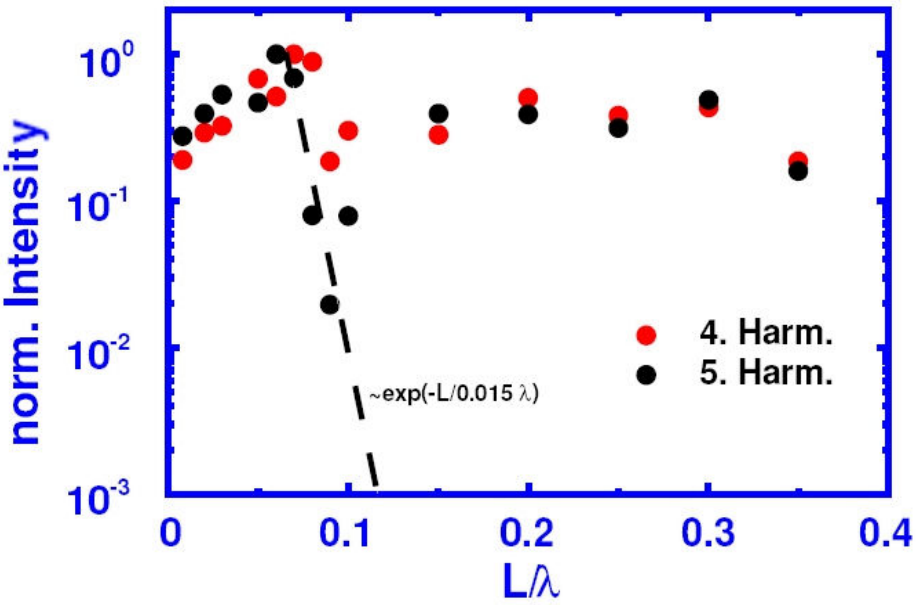

Figure **1.XII** PIC calculated dependence of the fourth and fifth harmonic on the normalized scale length. Parameters are: n/n_c=45.56, a=0.3 and the angle of incidence is 45°.Figure is taken from [10].

In this section two scale length regions with qualitatively different mechanisms of HOHG for the used set of parameters are identified.

In the first scale length region ($0 \leq L/\lambda \leq 0.09$) the "resonant" (non-relativistic) mechanism of HOHG dominates. In the second scale length region ($0.09 \leq L/\lambda \leq 0.35$) the "oscillating mirror" (relativistic) mechanism of HOHG dominates. In the intermediate scale length position ($L/\lambda \approx 0.1$) HOHG is suppressed.

Chapter 2 T³ laser system at the IEP

At the beginning of this chapter the 10 Hz Table Top Terawatt (T^3) laser system at the "Institut für Experimentelle Physik" (IEP) at the University of Duisburg-Essen is briefly described. After that the pulses delivered by the laser system are characterized. Further, the possibility of the second harmonic pulse generation is considered more closely. Then, the measurements of the laser stability are presented. Finally the adaptive optics system is discussed in more detail.

2.1 Overview and characterisation of the T³ Laser

The Ti:Sa 10 Hz multi terawatt laser at the IEP is a typical chirped pulse amplification system (CPA) [8, 9] schematically shown in figure 2.I. The main idea behind the CPA laser system is to increase the pulse duration before the amplification in order to decrease the peak intensity in the amplifier. The pulse duration is increased by a device called a "stretcher" which adds the controlled, positive dispersion to the laser pulse. The "chirped" pulse is then amplified by the amplification system. After amplification the pulse duration is decreased nearly to the initial duration by another device, called a "compressor" which adds the negative dispersion to the pulse. In an ideal case the dispersion introduced by the "compressor" compensates the dispersion added to the pulse by the "stretcher" and amplifier. The advantage of the CPA laser system is the relatively small peak intensity in the amplifier. It allows the pulse distortions caused by the nonlinear effects in the amplifier to be minimized and prevents damage to the optical components in the amplifying system.

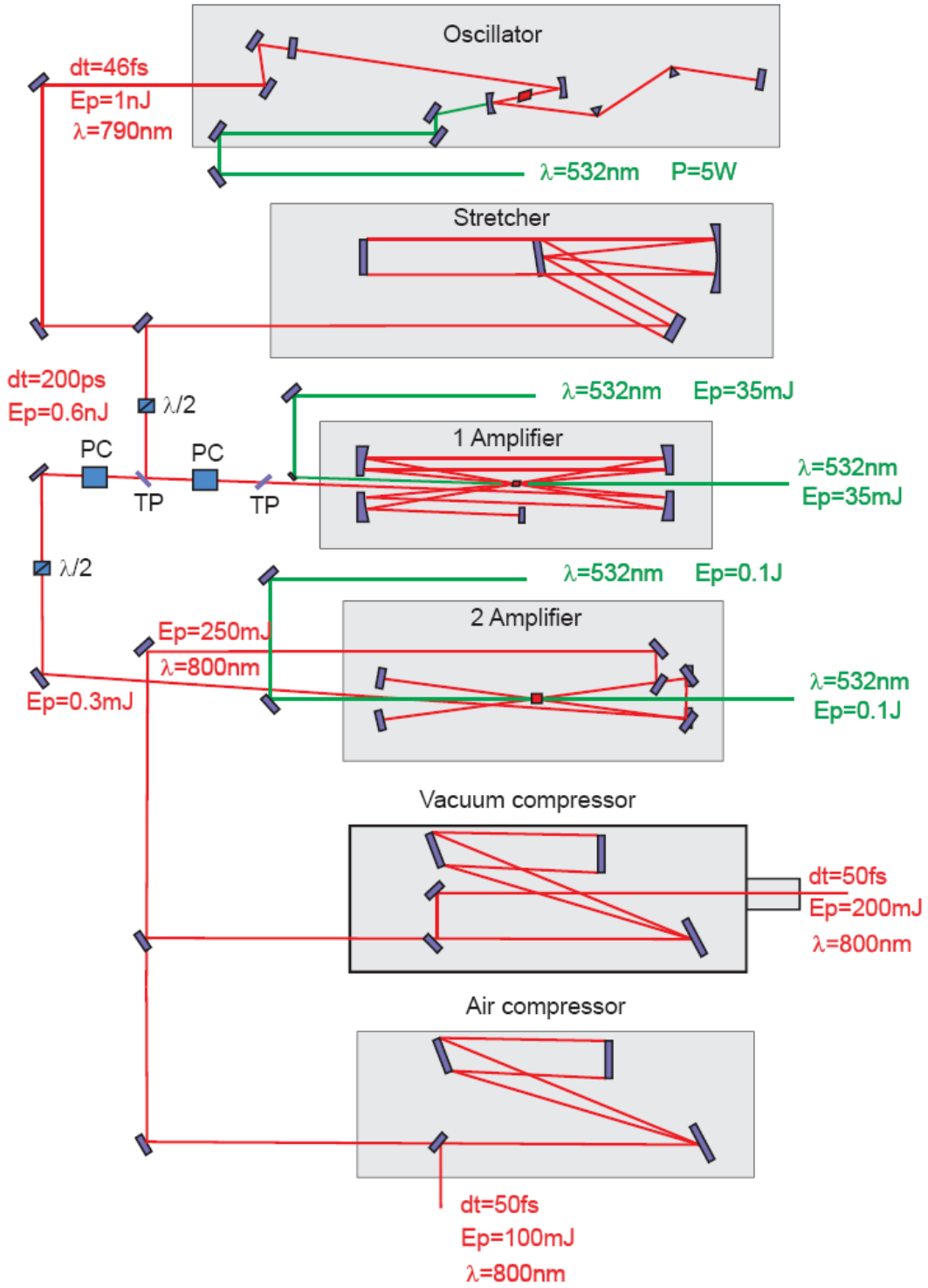

Figure **2.I** The principle scheme of the 10 Hz T³ laser system at the IEP.

dt	pulse duration (FWHM)	PC	Pockels cell
Ep	average pulse energy	TP	Thin film polarisator
P	average CW power		

The main components of the laser system are shown in figure 2.I.

The hard Kerr-lens mode locked Ti:Sa oscillator (see Appendix A2) is the core of the laser. It produces a train of pulses with the repetition rate of 80 MHz. The average power of the oscillator is approximately 400 mW. The spectral bandwidth of a generated radiation is 21 nm FWHM, which is centred at 800 nm (see figure 2.II). The bandwidth limited duration of the pulse is estimated to be 45 fs FWHM. A detailed estimation of the bandwidth limited pulse duration can be found in appendix A3. The measured pulse duration of 46 fs FWHM is close to the bandwidth limited pulse duration. The contrast of the pulses is better than 10^{-8} at 1 ps before the pulse maximum (figure 2.III). The notion "contrast" is explained in section 2.2. The pulse "quality" of the whole laser system is not better than that of the pulses generated by the oscillator. This means that the shortest pulse duration as well as the highest contrast of the T³ laser system are already defined by the oscillator pulses.

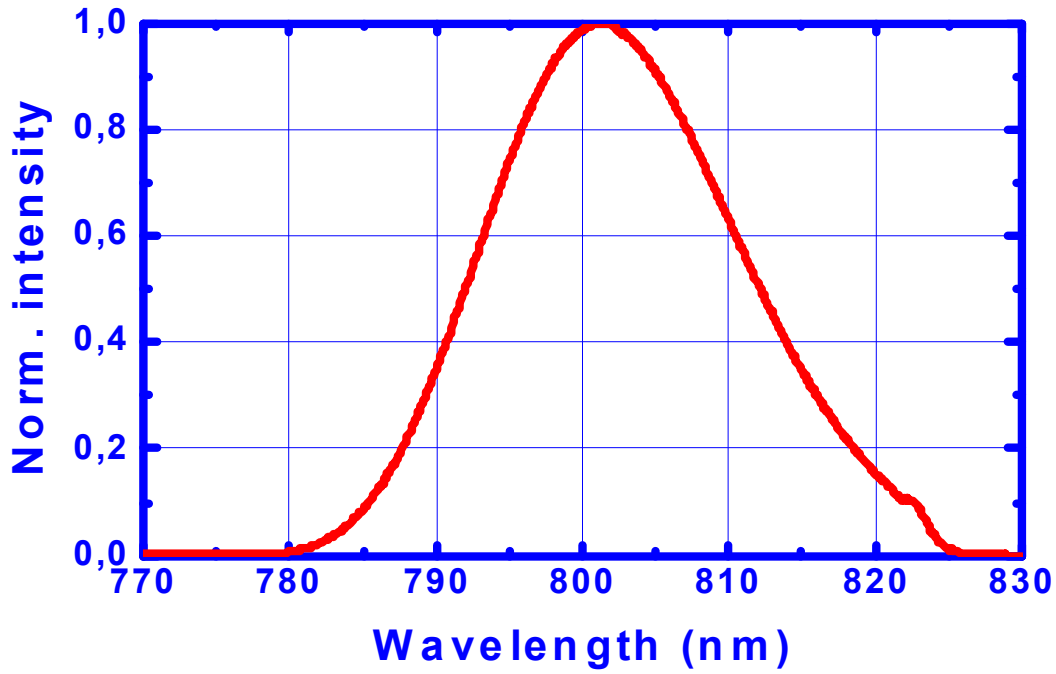

Figure **2.II** Spectrum of the pulses generated by the oscillator.

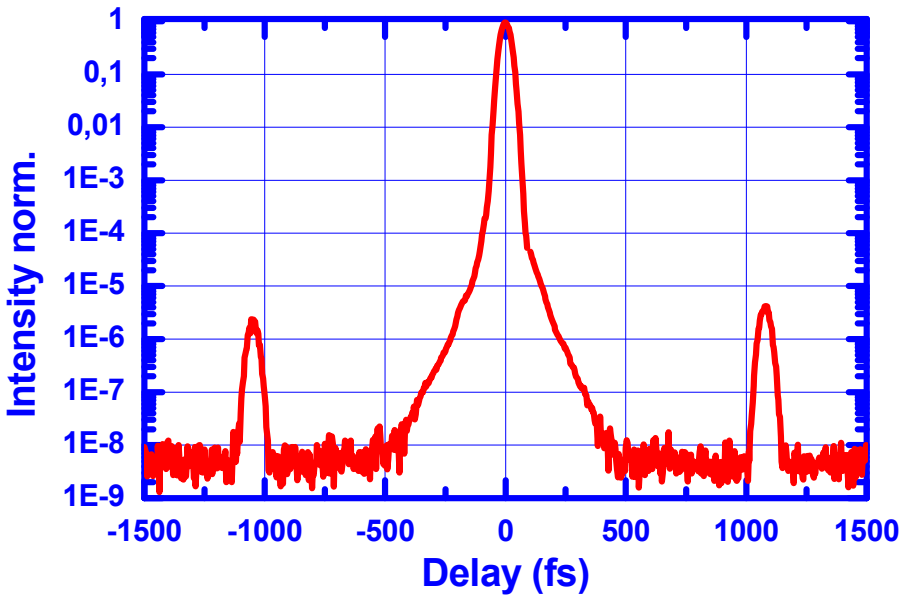

Figure **2.III** The second order autocorrelation function of the pulses generated by the oscillator

Two artificial peaks appearing in the autocorrelation function (figure 2.III) at ca. 1.1 ps before and after the main pulse are reflections from the surfaces of the nonlinear crystal, which is used in the autocorrelator. The autocorrelators of the second and third orders are briefly described in appendix A4.

Before amplifying the pulses are extended in the stretcher up to the duration of ca. 200 ps. The stretcher is a device which adds the controlled positive phase dispersion to the pulse. As a result the blue components of the pulse spectrum are delayed with respect to the red components. The principle schemes and the short description of the stretcher and the compressor can be found in appendix A5.

For further amplification, the single pulses with a repetition rate of 10Hz are selected from the initial pulse train by an optical switch which consists of Pockels cell and thin film polarisators. This device also prevents the amplified pulses from propagating back to the oscillator.

The amplifier of the T³ laser system consists of two multipass amplification stages separated by an additional optical switch. In both stages the Ti:Sa crystals are used as active media.

In the first amplification stage the pulses are amplified from ca. 0.6 nJ to 0.5 mJ and the resulting gain is of the order G ≈10^6. In the second amplification stage pulses are amplified up to 250 mJ (the gain is G ≈10^3). The resulting gain of the whole amplifier is G ≈10^9.

After amplification the pulses are compressed nearly to the original pulse duration. The condition required for the best possible recompression is the undisturbed spectrum during the stretching, amplification and recompression of the pulses, i.e. no modulation of the spectral amplitude should occur. The spectrum immediately after the oscillator and that of the amplified and recompressed pulses are compared in figure 2.IV

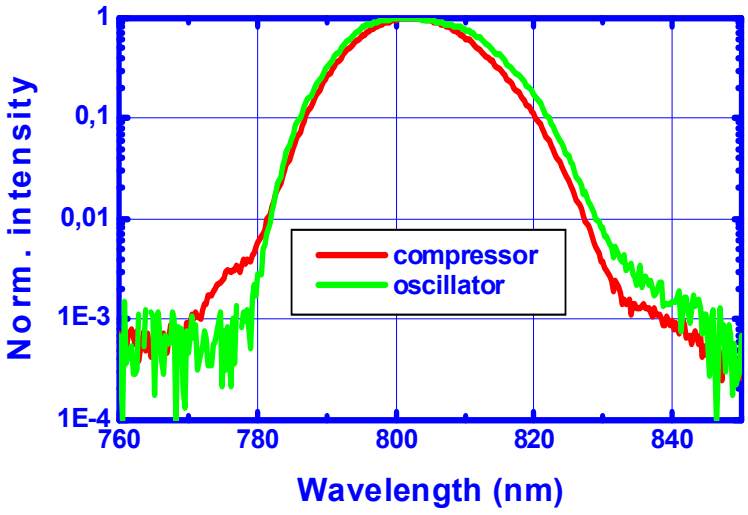

Figure **2.IV** Spectra of the pulses immediately after the oscillator (green curve) compared with that after the recompression (red curve).

No modulations appear in the measured spectrum after compression (figure 2.IV red curve). Moreover, figure 2.IV reveals the narrowing of the spectrum after the amplification. Consequently, the bandwidth limited pulse is longer. In this particular case the bandwidth limited pulse duration is changed from 45 fs FWHM before amplification to 47 fs FWHM after compression.

In the stretcher and compressor of the laser system the gratings are used as dispersive elements. With the help of the grating based stretcher and compressor, it is possible to tune independently the dispersions of the second and third orders. Thus in the ideal case these

devices are adjusted in such a way that the dispersions of the second and third orders vanish [45].
The 10 Hz laser system at the IEP is equipped with two compressors. Depending on the pulse energy one or another compressor is used. With the help of a beam splitter, both compressors can be used simultaneously to provide two pulses with independently tuneable pulse duration. The first compressor is designed for pulses with moderate intensities. The second compressor is placed in a vacuum chamber to prevent the gratings from being burned and to avoid self-modulation in the air at high peak intensities. Due to the limited efficiency of the diffraction gratings, approx. 70% of the energy passes through the compressors.

After the vacuum compressor an adaptive mirror is installed to improve the wave front distortions of the laser beam. It allows us to produce nearly diffraction limited focus. The adaptive optic at the IEP is discussed at the end of the second chapter (section 2.5).

2.2 Characterization of the 800 nm pulse

Not only the energy and the pulse duration but also the "quality" of the laser pulses is essential for HOHG experiments on solid targets.

Because of the dispersion of the fourth and higher orders the stretched and amplified pulses can not be recompressed exactly to the original shape or duration. As mentioned in section 2.1, the conditions for the best possible pulse recompression are the undisturbed spectral amplitude and vanishing dispersions of the second and third orders. In real lasers some radiation appears a few ps. before and after the pulse maximum, the so-called "wings" of the pulse. The intensity of that radiation is characterised by the contrast. The contrast is the intensity at some fixed time normalized by the peak intensity of the pulse, usually 1ps before the pulse maximum. The contrast can be measured by recording the autocorrelation function. In our case according to the measured autocorrelation function of the third order, the contrast is approx. 10^{-7}, see figure 2.V. The small peak at 2 ps in front of the main pulse is caused by the reflection on the surfaces of the nonlinear crystal in the correlator. The working principle of the autocorrelator of the third order is given in appendix A4.

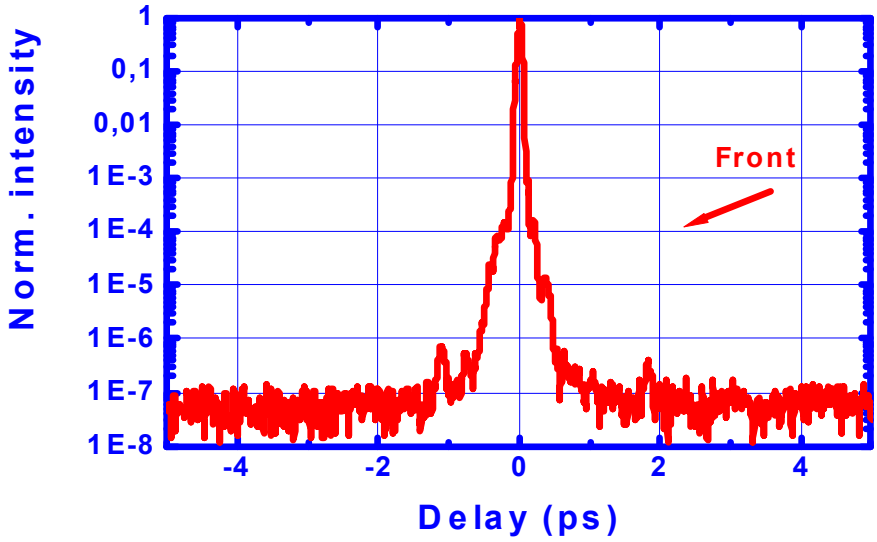

Figure **2.V** Autocorrelation function of the third order of the amplified pulse.

Besides the spectral amplitude modulation and the dispersion there are two additional effects resulting in the appearance of the "wings". The first effect is the limited transmission coefficient of the optical switches which are mentioned in section 2.1. Part of the radiation penetrates even through the "closed" optical switch. The resulting intensity level of this radiation, immediately after the optical switch, is measured to be in the order of 10^{-7} [46]. This radiation is not amplified, because it does not overlap temporally with the pump pulses. This means that the intensity of this radiation normalized by the intensity of the amplified pulses is of the order 10^{-15}.

Another possible reason for the appearance of the "wings" is the amplified spontaneous emission (ASE) [47]. The estimated level of the ASE normalized by the peak intensity of the laser system at the IEP is 10^{-9} [46]. Thus, both effects are negligible.

The spectrum of the amplified pulse is presented in figure 2.VI. The bandwidth of the spectrum shown in figure 2.VI is 20 nm FWHM. The corresponding calculated band width limited pulse duration of 47 fs FWHM is very close to the measured pulse duration of 50 fs FWHM.

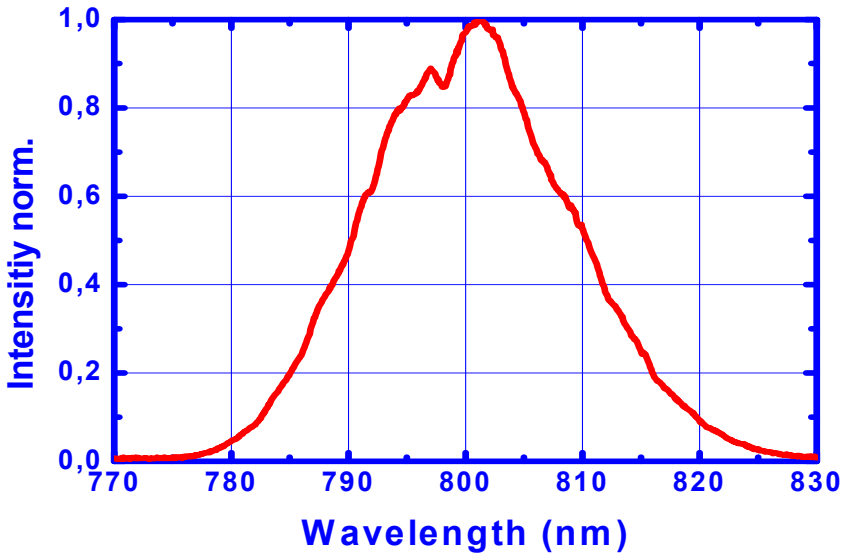

Figure **2.VI** Measured spectrum of the amplified pulse

In conclusion of this section the main pulse parameters are summarized:

Middle wavelength:	800nm
Spectral bandwidth:	20 nm FWHM
Pulse duration:	50 fs FWHM
Pulse energy (max.):	200 mJ
Contrast at 1 ps:	10^{-7}
Polarization:	linear, horizontal.
Beam diameter:	25 mm FWHM

2.3 Generation and characteristics of second harmonic pulses

In this section the conversion of the laser pulse to the second harmonic (SH) is discussed. The discussion starts with the motivation of the SH pulse generation. Further, the normalized vector potential of the SH pulse is estimated. The measured spectrum of the SH pulse is presented and the corresponding bandwidth limited pulse duration is compared with the duration of the numerically calculated SH pulse. In conclusion of this section the main SH pulse properties are summarized.

For the laser-plasma interaction experiments discussed in the third chapter, the normalized vector potential and the "quality" of the laser pulses are of crucial importance. As was shown in the previous section, the contrast of the pulses provided by the 10 Hz Ti:Sa laser is ca. 10^{-7}. On the target surface the intensities of 10^{19} W/cm^2 are expected. Since the ionization threshold for most of the solids is in the order of 10^{12} W/cm^2, the matter could be ionized long before the pulse maximum arrives. In this case the laser pulse itself could interact with already dilute plasma instead of a solid matter. The conversion to the second harmonic can mend the pulse quality [48].
Using the relation:

$$I_{2\omega} \propto I_{\omega}^{2} \qquad (2.1)$$

it is easy to estimate the contrast of the second harmonic (SH) pulse in an ideal case to be $(10^{-7})^2 = 10^{-14}$. Here I_ω and $I_{2\omega}$ are the intensities of the fundamental and of the SH beams, respectively. Thus, the roughly estimated intensity of the SH radiation at 1 ps before the pulse maximum ($I_{2\omega} < 10^{19-14} = 10^5$ W/cm²) is insufficient for the formation of the plasma. In this case the interaction of the laser pulse with the diluted plasma instead of the solid matter can be excluded. However, it should be mentioned here that the relation 2.1 is based on a number of simplifying assumptions, which are not valid in the case of ultra short pulses (USP) at relativistic intensities.

The theory of the second harmonic generation (SHG) as a part of the three wave interaction process is well developed and understood. It can be found in standard books on non-linear optics [31, 49]. Analytical solutions exist for the plane monochromatic waves in the case of low intensity and conversion efficiency. For USP with a spectral bandwidth of several tens of nm, 20 nm in our case, and an energy conversion efficiency of 10% to 50% these solutions are not valid. Moreover, the peak intensity of the pulses is extremely high. Thus not only the influence of the second order nonlinear susceptibility $\chi^{(2)}$ but also of the third order susceptibility $\chi^{(3)}$ has to be taken into account. The $\chi^{(3)}$ nonlinearity gives rise to self-phase modulation. The combined action of the susceptibilities of the second and third order causes the cross-phase modulation. Besides, the group velocity mismatch between the fundamental and the SH pulses, can not be neglected in the case of the fs pulse conversion to the SH. The influence of these effects on the USP SH generation is discussed in [49, 53 - 57]. The corresponding coupled differential equations can be found in [55].

For the estimation of the normalized vector potential "a" of the SH pulse the modified relation (0.1) is helpful.

$$a^2 = I\lambda^2 b^{-1} \qquad (2.2)$$

Here $b \approx 1.37\ 10^{18}$ W cm^{-2} μm² is a constant [10].
To evaluate the intensity on the r.h.s. of the relation (2.2) the energy conversion efficiency and the pulse duration have to be figured out. The measured energy conversion efficiency as a function of the pump pulse energy is presented in figure 2.VII.

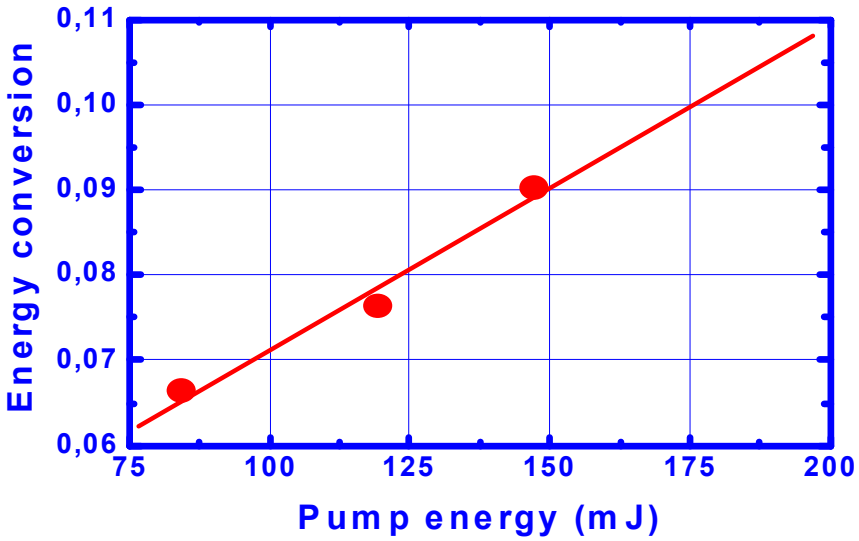

Figure **2.VII** Measured energy conversion efficiency of the 50 fs pulses at 800 nm to the SH in the 0.8 mm KDP crystal.

According to figure 2.VII, approx. 10% of energy conversion efficiency of the 200 mJ laser pulse to the SH can be assumed ($E_{2\omega}$ = 20 mJ).

The envelope of the SH pulses which are generated in the 0.8 mm thick KDP crystal is calculated numerically with the help of the code provided by the SNLO [58] using the following parameters:

Angle of incidence	Θ_c	45°,
Group velocity of the fundamental pulse	v_0	c / 1,526,
Group velocity of the SH pulse	v_2	c / 1,550,
Refractive index	n	1,502,
Effective susceptibility	d_{eff}	0.28 (pm/V),

The fundamental pulse is assumed to be Gaussian with a duration of 50 fs FWHM.

The result of numerical integration is shown in figure 2.VIII. The corresponding pulse duration Δt is 45fs FWHM.

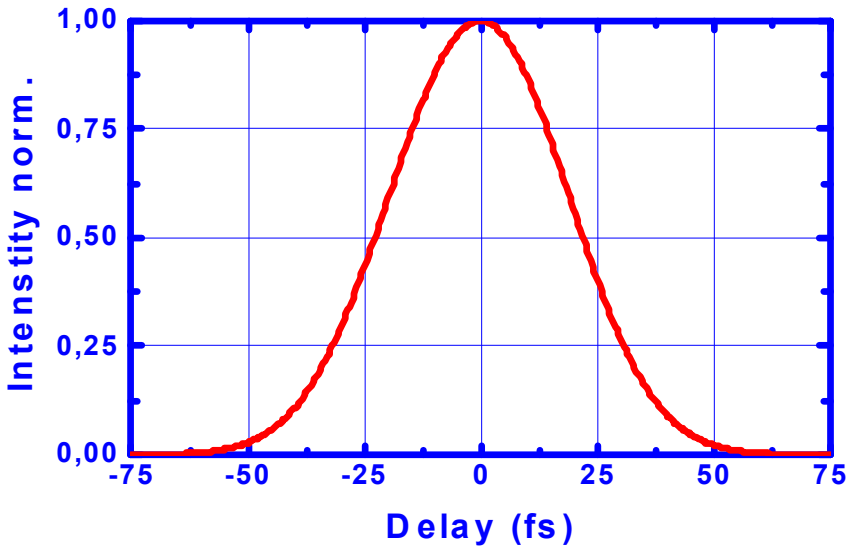

Figure **2.VIII** SH pulse shape provided by the numerical integration with the help of the SNLO code [58]. The Interaction parameters are: incidence angle Θ_c=45°, group velocity of the fundamental and SH pulses v_0 = c/1.526 and v_2 = c/1.550, refractive index n=1.502, effective susceptibility d_{eff} = 0.28 (pm/V). The fundamental pulse is assumed to be Gaussian with a 50 fs FWHM.

The measured spectrum of the SH pulse is shown in figure 2.IX. The bandwidth limited SH pulse duration corresponding to this spectrum (45fs FWHM) is equal to the numerically calculated one.

Using this data (λ=0.4μm, $E_{2\omega}$=20 mJ, Δt = 45 fs) the normalized vector potential of the focused SH radiation on the target surface can be estimated according to the relation 2.2 ($a^2 = E_{2\omega}\lambda^2 / 2\Delta t A b$) to be a ≈ 2. For this estimation half of the pulse energy is assumed to be focused in a spot ($A = \pi d^2/4$) with the diameter d = 0.9 μm, which is the FWHM of the

intensity distribution[1] in the focal plane. The estimated normalized vector potential is well within the relativistic range.

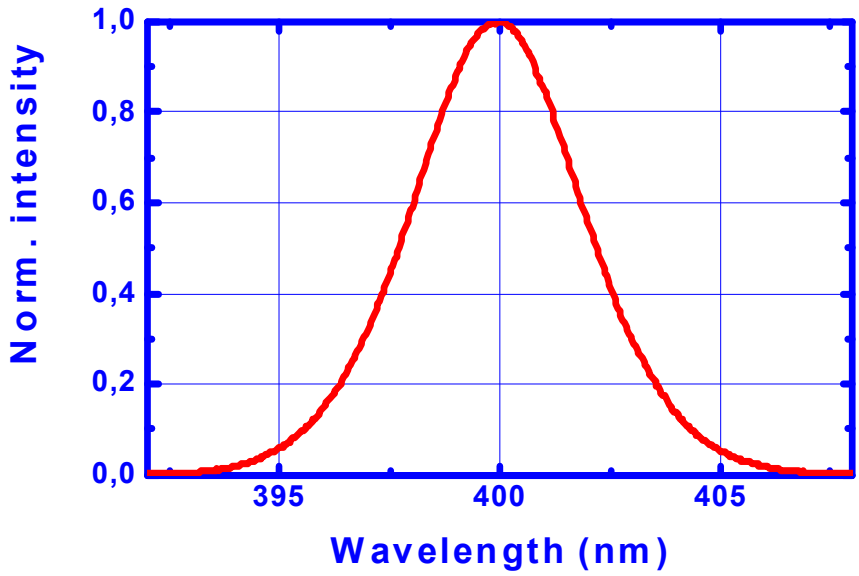

Figure **2.IX** Measured spectrum of the SH pulse

In conclusion of this section the main parameters of the SH pulses are summarized:

Middle wavelength:	400nm
Spectral bandwidth:	5,2 nm FWHM
Pulse duration:	45 fs FWHM
Pulse energy (max):	20 mJ
Polarization:	linear.

[1] The calculated intensity distribution in the focal plane is given in figure 3.IV.

2.4 Stability of the laser system

To achieve reliable and reproducible experimental results the properties of each laser pulse has to be precisely controlled. Thus stability is the essential feature of the laser system. Since the experiments on HOHG usually run for 10 hours and longer, the long term stability of the laser system plays an important role. On the other hand the pulse-to-pulse stability is important for single pulse experiments. Two types of laser stability are of crucial importance for the experiments described in the third section: a) pointing stability and b) energy stability. The experimental results presented in this section were achieved by U. Shymanovich [7] using the "air" compressor of the laser system.

a) Pointing stability describes the angular shift of the laser beam during some fixed time t. This kind of stability is important for experiments which require focusing of the pulses onto a target. The angular shift of the laser beam can result in a misalignment of the experimental setup. To investigate the pointing stability the laser beam was focused with the help of a lens (focal length is 1m). The position of the focal spot ("centre of gravity") was recorded for each laser pulse with the help of a charge coupled device (CCD) placed in the focal plane of the lens. The measured positions of the focal spots for a sequence of 500 laser pulses are shown in figure 2.X.
The measured pulse-to-pulse pointing instability of the laser pulses is ca. 35 microradian (RMS). This value is comparable to the divergence of the laser radiation (for λ = 800 nm and for the diameter of the beam D = 2.5 cm FWHM the divergence of the radiation is λ/D = 32 microradian).

Further, the angular drift of the laser beam on a long time scale was measured. Figure 2.XI shows the position of the focused laser beam during a period of 2.5 hours. The measured positions were averaged over 500 pulses.

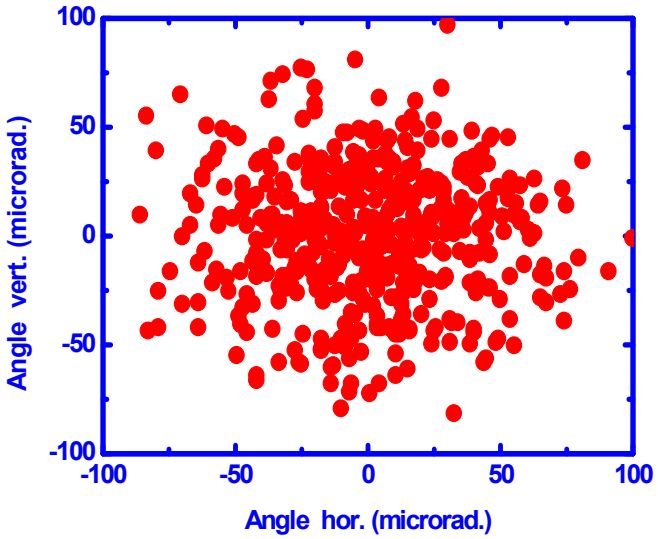

Figure **2.X** Pulse-to-pulse pointing stability of the laser system.

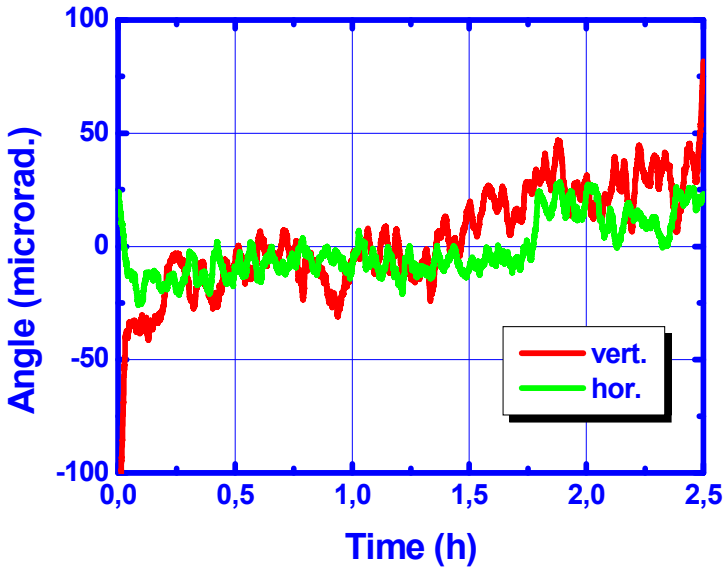

Figure **2.XI** Angular shift of the laser beam over 2.5 hours horizontally (green curve) and vertically (red curve)

Figure 2.XI reveals an excellent long time scale pointing stability (less than 100 microrad) of the 10 Hz. T³ laser system at the IEP.

b) The pulse energy stability is an important characteristic of the laser system. Long scale temporal dependencies of the fundamental and the SH laser pulse energies (averaged over 500 pulses) are shown in figure 2.XII.

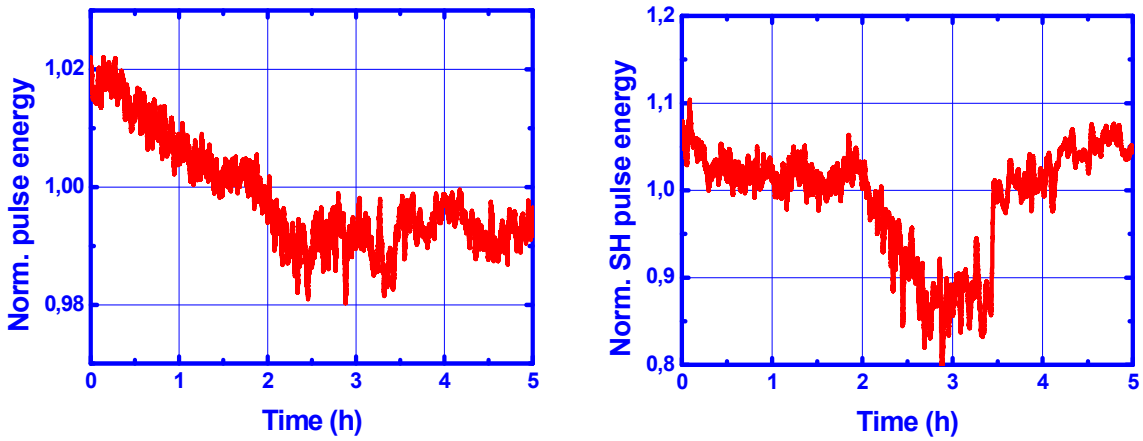

Figure **2.XII** Energy instability of the laser system over 5 hours: left fundamental pulse; right SH pulse.

Figure 2.XII reveals the fundamental and the SH pulse energies being stable during hours of continuous operation of the laser system within ~3% and ~10%, respectively. The standard deviations of the fundamental (800 nm) and the second harmonic (400 nm) signals for a sequence of 500 laser pulses were ~2.5 % and ~7 %, respectively.

The standard deviation of the SH is more than twice larger than that of the fundamental pulses. Since SHG is a non-linear process in which the intensity of the SH is proportional to the square of the fundamental beam intensity, the small changes in the intensity of the fundamental beam should lead to approximately twice larger changes in the SH beam intensity. The reasons for the relatively high instability of the SH pulses could be the pulse-to-pulse variations of the pulse duration and/or fluctuations of the beam profile.

The stability of the laser system is mostly influenced by the changes in the environment temperature. The measurements presented here were done for typical temperature drifts of approx. one degree.

The measurements described in this section avouch that the laser system can be used for experiments requiring high accuracy standards.

2.5 Adaptive optics

Using the T³ laser system described in this chapter, diffraction limited focus is the condition required for the realisation of experiments at relativistic laser intensities.

As reported in section 2.3, the fundamental pulse is converted to the SH in order to provide the pulse with the desired contrast. The SH is generated with the help of a thin (0.8 mm) KDP disk with the diameter of 5 cm. It is very difficult to produce the KDP platelet with such dimensions and the required optical surface quality. Insufficient KDP surface quality results in the disturbed (not flat) wave front of the generated SH pulse. In their turn, the wave front aberrations make it impossible to reach the diffraction limited focal spot size. Some of the well-known wave front aberrations and their mathematical representation can be found in appendix A6. The adaptive optics system makes it possible to improve a disturbed wave front.

We use the commercial adaptive optics system (delivered by the firm Night N (opt) Ltd) which consists of the Shack-Hartmann wave front sensor, bimorph deformable mirror and control unit. This system works in a loop regime. The cycle of the loop consists of three basic steps. First, the wave front aberrations are detected with the help of the wave front sensor. Then, the necessary deformations of the adaptive mirror are calculated in order to compensate the measured wave front aberrations. Finally, the curvature of the adaptive mirror is adjusted.

In the Shack-Hartmann sensor an array of lenses is used for the detection of the wave front. The positions of the particular focal spots depend on the wave front curvature, see figure 2.XIII. These positions are detected with the help of a CCD camera.

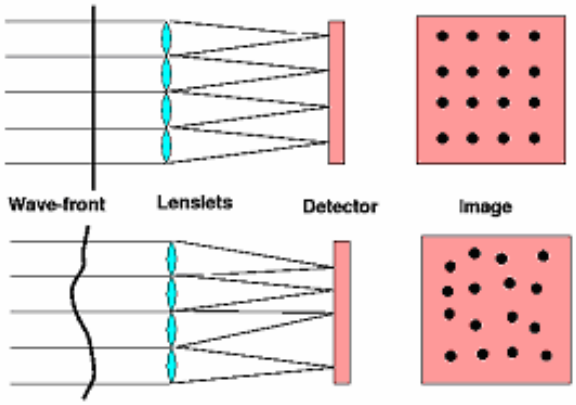

Figure **2.XIII** Working principal of the Shack-Hartmann wave front sensor

Comparing the positions of the focal spots with that of the reference beam which is assumed to be with the flat wave front it is possible to calculate the wave front of the measured beam.

Our deformable mirror consists of a glass substrate with a dielectric mirror coated on it, two piezo discs and 32 electrodes glued on them, see figure XIV. Putting high voltage on the electrodes the desired deformation of the mirror can be produced.

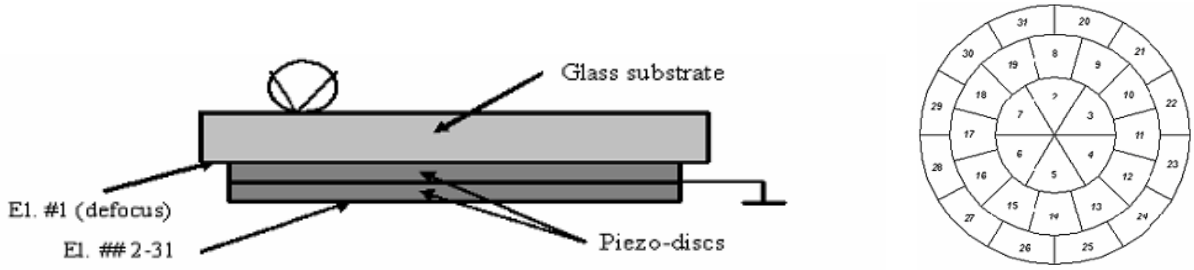

Figure **2.XIV** Left: schematic structure of bimorph deformable mirror at the IEP. Right: electrode scheme of the deformable mirror.

Additionally, some specifications of the adaptive optics system at the IEP are listed below:

Wave front sensor:		Deformable Mirror:	
Optical band width (nm)	400 - 1000	Number of electrodes	32
Beam diameter (mm)	20 – 64	Max repetition rate (kHz)	3.8
Lens array	40X40	Max. reflectivity at 780nm (%)	99.9
Max. repetition rate(Hz)	30	Optical band width (nm)	720 -840
		Aperture (mm)	50

Usually the adaptive optic system works in the following scheme, see figure 2.XV (A). After reflection from the deformable mirror the laser beam is split into two parts. One part illuminates the wave front sensor. Another part is used for the experiments.

For our setup a different scheme of the adaptive optic system was proposed by A. Tarasevitch, see figure 2.XV (B). After reflection from the deformable mirror the laser beam is converted to the SH in a KDP crystal. Further, the fundamental beam is blocked. The SH beam is split into two parts. The wave front sensor is illuminated by the first part of the SH beam. Another part of the SH beam is used for the experiments.

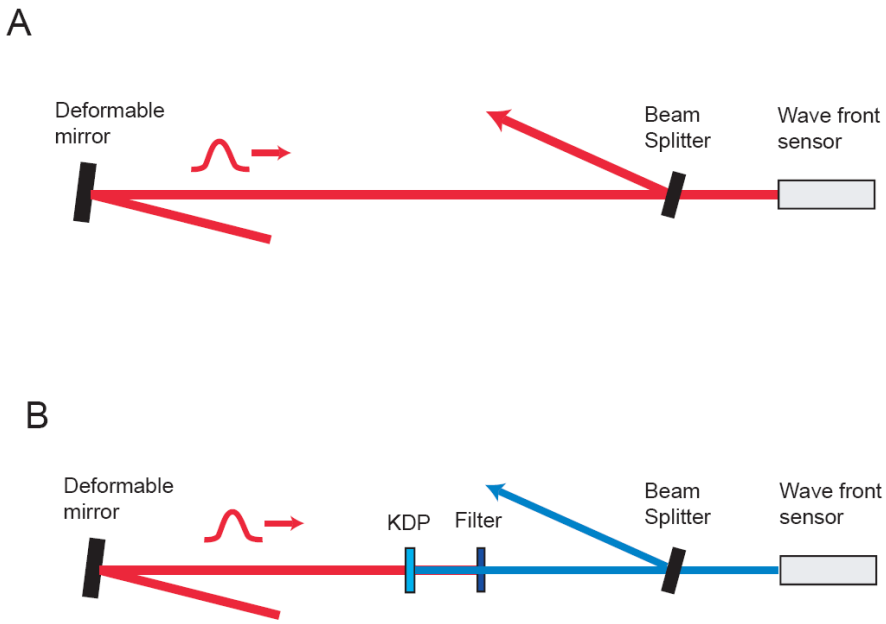

Figure **2.XV** Scheme of the usual adaptive optics setup (A) and the scheme of the adaptive optics setup which is used in the experiments (B).

To check our scheme of the adaptive optics setup one additional experiment is performed. The experimental setup is illustrated in figure 2.XVI. After reflection from the deformable mirror the fundamental pulse is converted to the SH one in the 1.2 mm thick KDP crystal. In this experiment the SH pulse duration is not important. Thus the thicker KDP crystal is used to achieve the higher conversion efficiency. Two dielectric mirrors M1 and M2 (figure 2.XVI) with the reflectivity R_{800}=2% for the fundamental and R_{400}=100% for the SH beam separate the SH beam from the fundamental one. Further, the SH beam is divided into two beams by an uncoated suprasil wedge. The transmitted part of the SH beam is focused with the help of a

lens (focal length 5 m) on the CCD. The reflected part of the SH beam is analyzed in the wave front sensor.

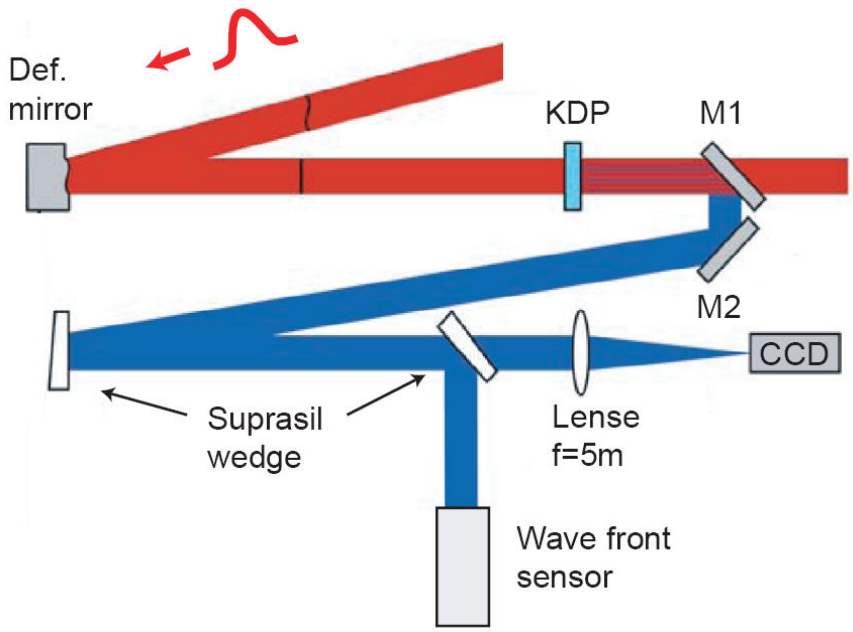

Figure **2.XVI** Scheme of the experimental setup. Figure is taken from [59].

The measured intensity distributions in the focal plane of the lens in cases without and with the wave front correction are presented in figure 2.XVII.

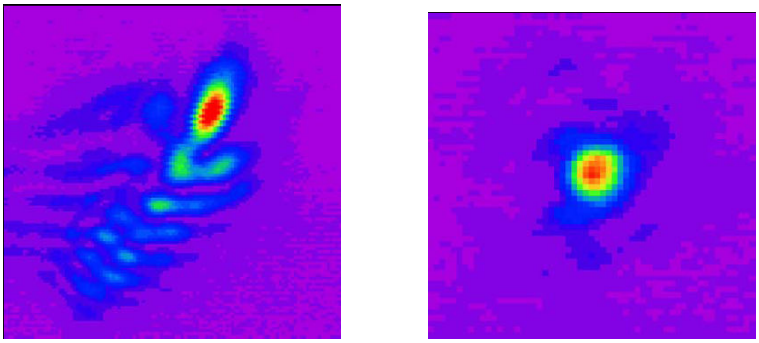

Figure **2.XVII** Intensity distribution in the focal plane of a lens (focal length is 5 m) at 400 nm without the adaptive optic system (left) and with the adaptive optics system (right).

In contrast to the irregular intensity distribution in the focal plane of the lens measured without adaptive optics (figure 2.XVII left), the improved one is nearly round (figure 2.XVII right). The diameter FWHM of the improved focal spot is 1.5 times the diffraction limited one. Since the energy of the corrected beam is concentrated on a much smaller focal spot an intensity increase by the factor of approx. 210 is observed.

With the help of this system the diffraction limited focus is nearly achieved. The result of this experiment proves the ability of the adaptive optics system using our scheme to improve the disturbed wave front.

The adaptive optics system at the IEP is discussed in more detail by A. Wloka [59].

Chapter 3 HOHG experiments

At the beginning of this chapter the experimental setup is described. Then the experiments on HOHG with laser intensities below and above the relativistic threshold (a = 1) are presented. The “wave mixing” experiment is discussed further. Finally, the experiment concerning the scale length influence on HOHG efficiency is considered.

3.1 Experimental Setup

For the experiments discussed in this chapter, laser pulses with relativistic intensities are required. To avoid the beam distortions due to nonlinear effects in the air, the vacuum compressor of our laser system described in section 2.1 is used. For the same reason the experimental setup itself as well as all optical elements between the compressor and the experimental setup are installed in vacuum chambers. Thus, on our optical table three vacuum chambers are placed: the compressor chamber, the adaptive optics chamber and the experimental chamber, which are connected to each other with vacuum pipes (figure 3.I).
This section is divided in two parts. Firstly, the setup of the adaptive optics chamber is presented and discussed. Secondly the setup of the experimental chamber is described in detail.

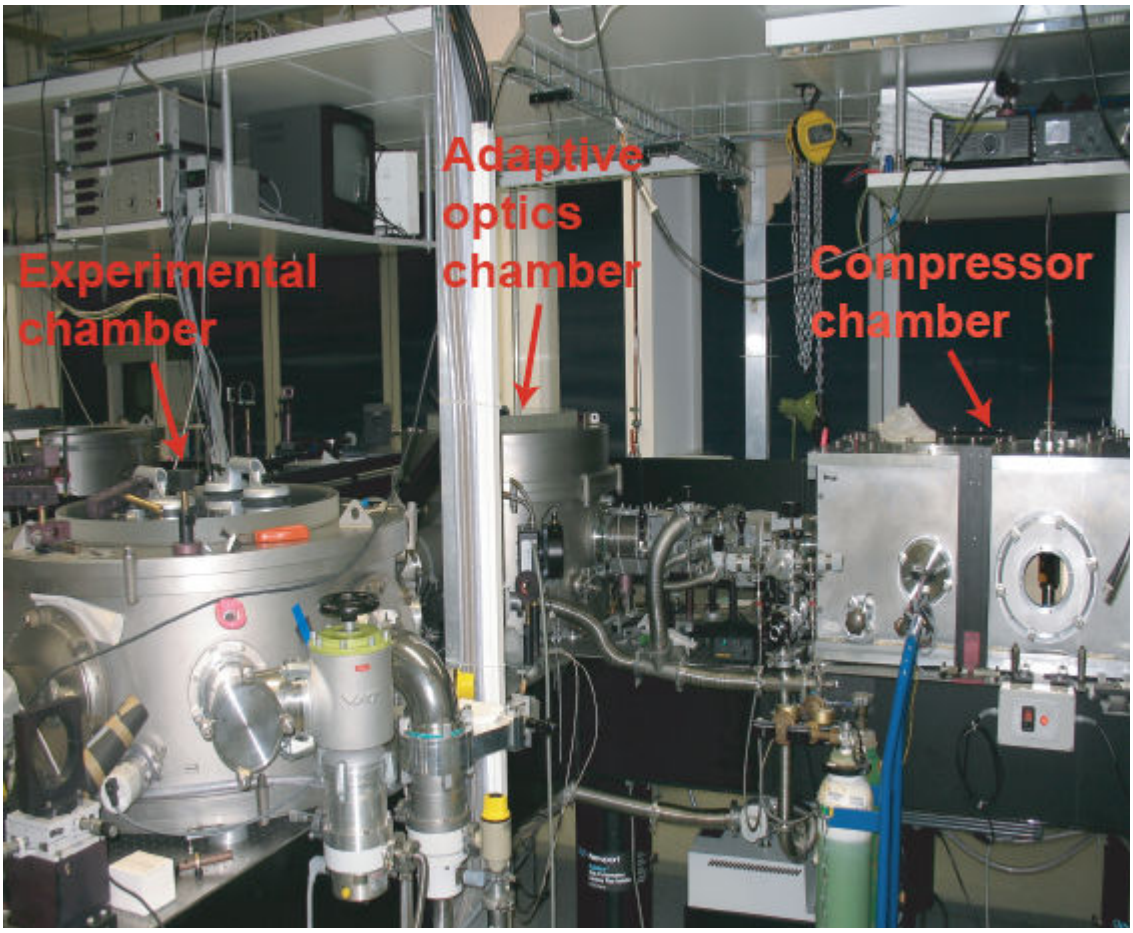

Figure **3.I** Vacuum chambers installed on the optical table: on the right is the compressor chamber, in the middle is the adaptive optics chamber and on the left is the experimental chamber.

Adaptive optics chamber:

After the vacuum compressor the fundamental laser pulses reach the "adaptive optics" chamber (see figure 3.II) where the deformable mirror is installed. Also, in this chamber the second harmonic (SH) beam is generated and the desired polarisations of the fundamental and the SH pulses are prepared.

In the adaptive optics chamber the laser pulses which are characterized in section 2.2 are reflected by the deformable mirror. After reflection from the deformable and the dielectric mirrors (figure 3.II M1, M2, M3) the fundamental beam (figure 3.II red line) is converted to the SH (figure 3.II blue line) in the 0.8 mm thick KDP crystal. Further, the SH beam is reflected by the "beam splitter" towards the experimental chamber.

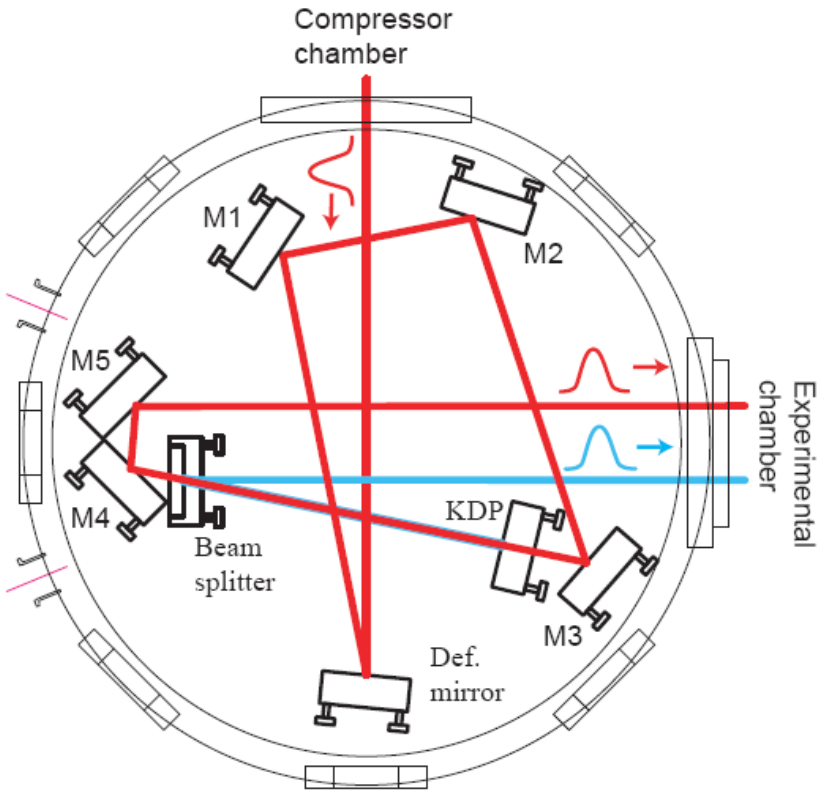

Figure **3.II** Scheme of the adaptive optics chamber. The fundamental beam is denoted by the red lines, the SH beam is denoted by the blue lines. M1-M5 are the dielectric mirrors.

The "beam splitter" is a 3 mm thick suprasil dielectric mirror with a reflectivity of R_{800}=2% for the fundamental and R_{400}=100% for the SH beam. The rear surface of the "beam splitter" is anti reflex coated for the fundamental frequency. The fundamental beam penetrates through the "beam splitter" and is directed to the experimental chamber by the dielectric mirrors M4 and M5.

We used the type I collinear SH generation, i.e. the ordinary fundamental beam is converted to the extraordinary SH one. Thus, the polarization of the generated SH pulses is perpendicular to the polarization of the fundamental pulses. The beam reaching the adaptive optics chamber is horizontally polarized. This means that in this configuration of the adaptive optics chamber, the horizontally polarized fundamental and the vertically polarized SH beams leave the adaptive optics chamber. If in HOHG experiment the horizontally polarized SH

pulse is desired, the mirror M1 has to be replaced by the “four mirrors polarisation flipper” in order to rotate the initially horizontal polarisation of the fundamental beam to the vertical one. In this case the horizontally polarized SH and the vertically polarized fundamental beams are directed to the experimental chamber. The “four mirrors polarisation flipper” is described in appendix A7. Further, if in HOHG experiment two beams, fundamental and SH, have to have the same polarisation, the mirror M5 should be replaced by one additional polarisation flipper to rotate the polarisation of the fundamental beam without changing the polarization of the SH beam. In this way it is possible to choose the polarisation of two beams, fundamental and SH, independently from each other.

Experimental chamber:

In the experimental chamber the SH (figure 3.III blue line) pulse propagates through the optical delay line (figure 3.III mirrors M2 and M3) to adjust the relative arrival time of the fundamental and the SH pulses on the target surface, see figure 3.III. Then both beams are focused with the help of the parabolic mirror on the target surface.

Before focusing the beams are reflected from the dielectric mirrors M5 and M6. These mirrors are fixed in front of the parabolic mirror on the linear translation stage. This makes it possible to shift the beams in a horizontal plane without changing the direction of their propagation. Since the parabolic mirror collects the parallel beams in a focal spot, in the case of parallel beam displacement the focal spot is still be fixed in space. The parallel shift of the beam results in the variation of the incidence angle on the target surface. Consequently, the direction of the generated high order harmonic also changes. In this way it is possible to scan with the generated radiation over the spectrometer and record the angular characteristics of the high order harmonics (figure 3.III). The angular resolution of this scan is ca. 2°.

Part of the second harmonic radiation penetrates though the dielectric mirror M5 and is used to illuminate the wave front sensor of the adaptive optics system (figure 3.III).

In the experiments both beams are focused with the help of the 101.6 mm in diameter, aluminium coated parabolic mirror. The 90° off axis parabolic mirror with an effective focal length of 101.6 mm is delivered by the firm “Janos Technology”.

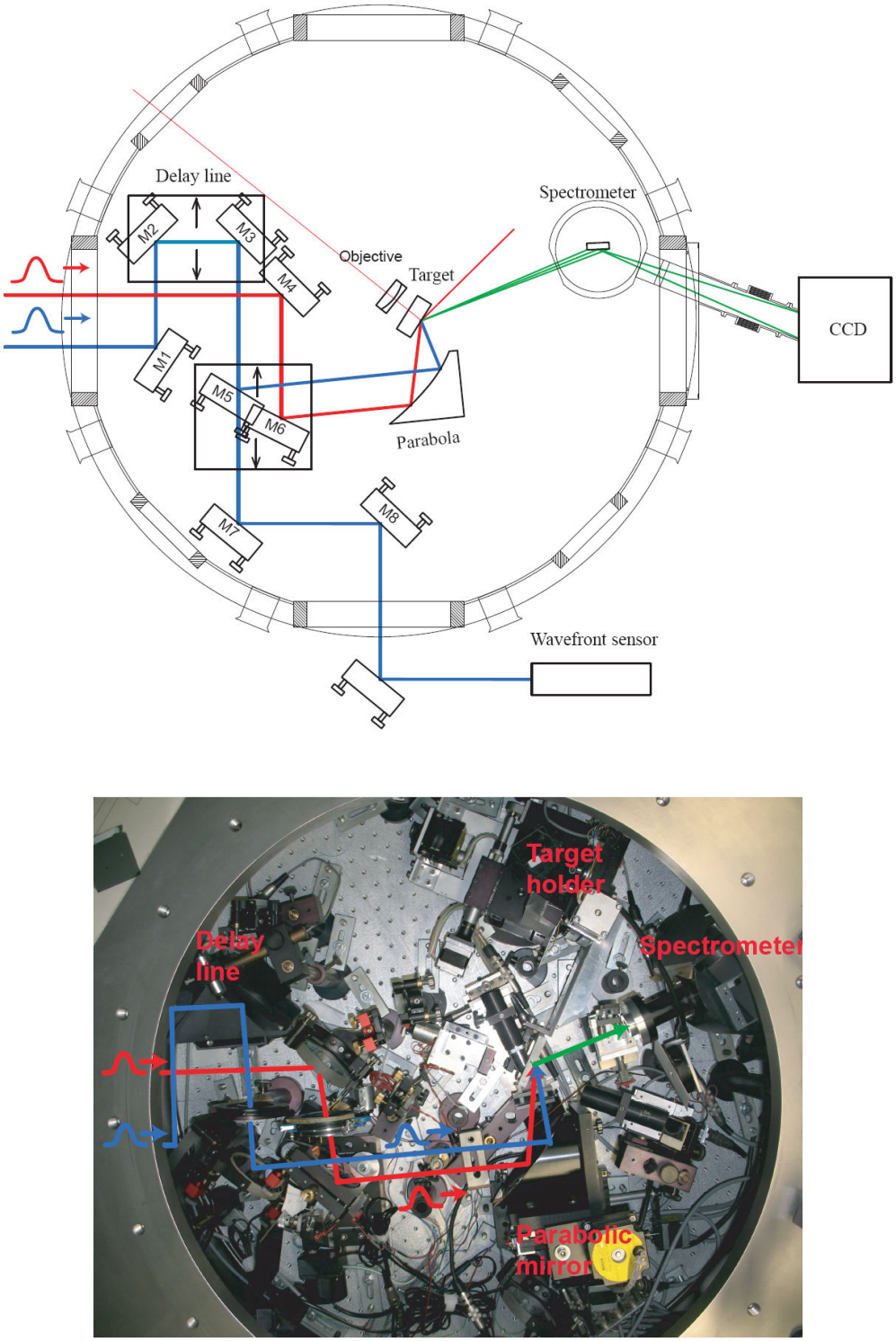

Figure **3.III** Experimental chamber. Upper image: principle scheme; bottom image: photograph. Red lines denote the fundamental beams. Blue lines denote the SH beams. Green lines and arrow are the generated high order harmonic radiation.

The diffraction limited focal spot can be estimated using the relation:

$$d \approx \frac{f\lambda}{D}\frac{2\ln 2}{\pi} \qquad (3.1)$$

Here d is the FWHM size of the focal spot. D is the FWHM of the incident beam. f is the effective focal length of the parabolic mirror. In the case of the SH radiation (λ = 400 nm, f ≈ 76 mm and D ≈ 15 mm) the estimated FWHM diameter of the diffraction limited focal spot is ca. 0.9 µm. The derivation of the relation (3.1) can be found in appendix A8.

Moreover, the calculation of the SH intensity distribution in the focal plane of the parabolic mirror is confirmed numerically with the help of "Matlab" routine, see appendix A8. The obtained intensity distribution in the focal plane is illustrated in figure 3.IV, left. The calculated diameter of the diffraction limited focal spot is 0.9 µm FWHM. The measured diameter of the focal spot is relatively close to the diffraction limited one, 1.3 µm FWHM (figure 3.IV right).

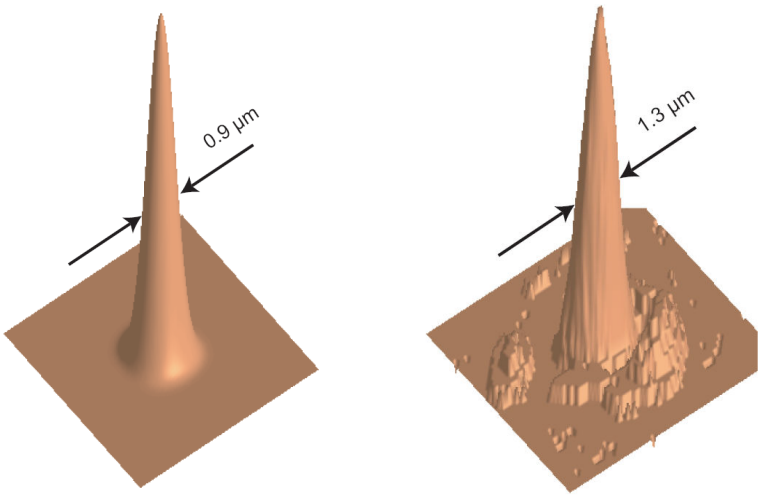

Figure **3.IV** Intensity distribution of the SH beam in the focal plane of the parabolic mirror. Left is the calculated intensity distribution. Right is the measured intensity distribution.

The reasons for the measured focal spot diameter being approx. 1.4 times the diffraction limited one are most probably the wave front aberrations caused by the mirror M5 and the parabolic mirror (figure 3.III) which are not improved by the adaptive optics system.

In the experiments the radiation was focused on the target surface. The target holder is designed to move in the target surface plane, to provide a fresh target surface for each laser pulse. The transverse deviations of the target movement are unacceptably large. Thus, the absolute position of the target surface was permanently observed with the help of a special "target stability monitoring" system (figure 3.V). The deviations down to 0.4 µm could be resolved and compensated by moving the target holder in the opposite direction. Thus, the position of the target surface was stabilized within the wave length of the used radiation (λ_{SH} = 0,4 µm).

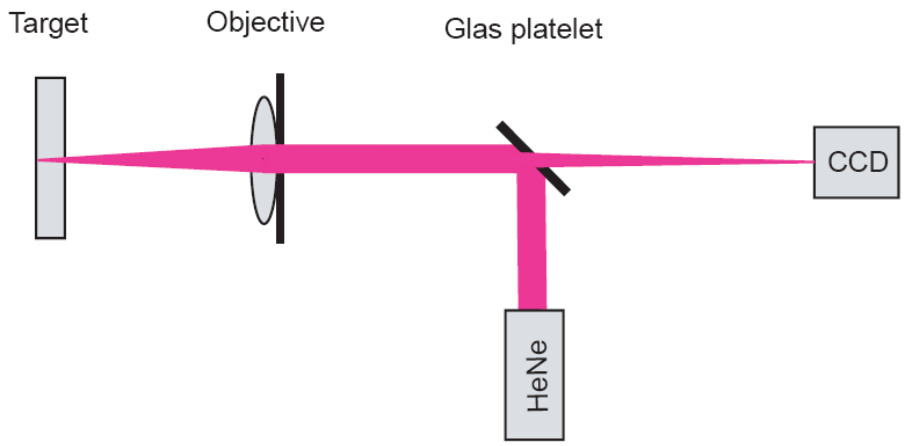

Figure **3.V** Scheme of the "target stability monitoring" system.

To monitor the absolute position of the target surface the HeNe beam was focused with the help of an objective (figure 3.V). The focused radiation was reflected back from the front surface of the target and focused again by the same objective on the CCD chip. The intensity distribution on the CCD chip is very sensitive to the distance variation between the objective and the reflecting target surface. To fix the absolute target position, the reference image was recorded. By comparing the current image with the reference, and moving the target holder the target surface could be placed in the original position.

The spectra of the radiation generated on the target surface, were analyzed with the help of a spectrometer. The spectrometer consists of a toroidal grating and a back-side-illuminated CCD-camera (figure 3.VI). The spectrometer is protected from the scattered fundamental and SH radiations by an aluminium filter. Moreover, it is protected from the reflected SH beam by the arrangement of a disc and an aperture. The disc is placed in front of the parabolic mirror in a way that the image of it covers the aperture which is installed in front of the spectrometer, see figure 3.VI.

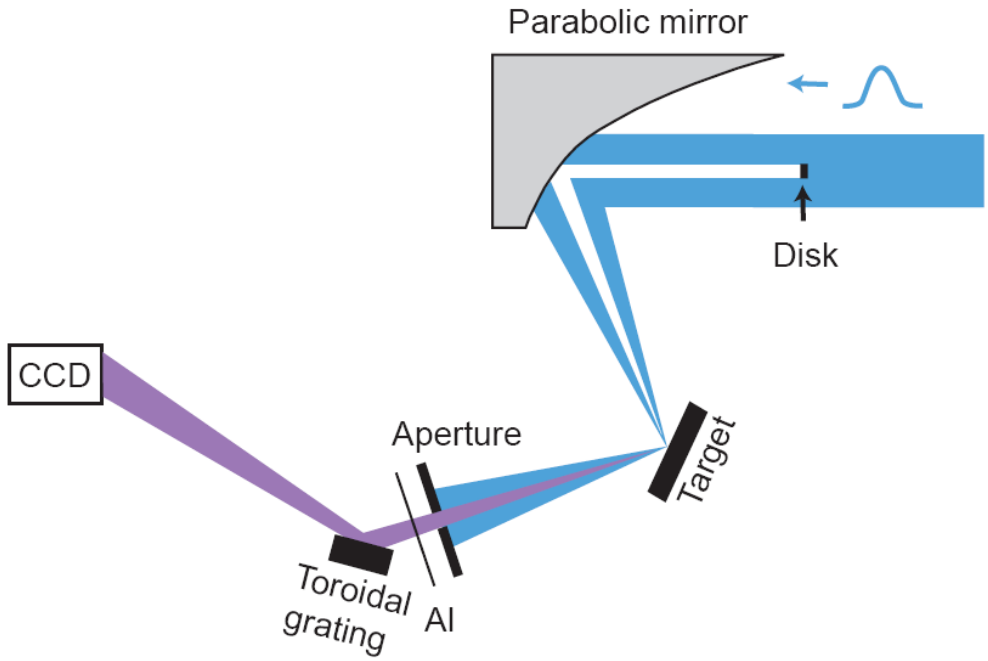

Figure **3.VI** Scheme of the spectrometer setup

We use the commercial toroidal grating produced by Jobin Yvon. The spectrometer works in the range from 100 nm down to 10 nm. The back-side-illuminated CCD which is used in the experiments is manufactured by “Priston instruments”, model: 1024TKB. Before being used, the spectrometer was calibrated with the help of a hollow cathode lamp and argon as working gas. The lamp itself, as well as the calibration procedure is presented in [14, 61-64].

In the experiments described in this chapter polystyrene (C_8H_8) is used as a solid target material. The electron density of the completely ionized polystyrene (n_e=3.2 10^{23} cm^{-3}) and the relation n_e/n_c=48, which corresponds to the SH are calculated. For the obtained plasma frequency (ω_p=3.25 10^{16} s^{-1}) the corresponding light wavelength is 58 nm. The advantage of using the density target material like polystyrene (1 g/cm³) is the substantial reduction in the calculation time for the corresponding PIC simulations making the direct comparison of the experimental and PIC results accessible.

3.2 HOHG below and above the relativistic threshold

In the experiment described in this section HOHG during the interaction of the relativistic and the non-relativistic laser pulses with the overcritical plasma is investigated. As discussed in the theoretical part there are two different mechanisms of HOHG in the cases of laser intensity above (a>1) and below (a<1) the relativistic threshold.

In the non-relativistic case the laser-plasma interaction can be qualitatively described by the "resonant" mechanism of HOHG. According to the "resonant" mechanism of HOHG, the harmonic spectra generated by the p-polarized excitation pulse are cut off at the plasma frequency ω_p. The interaction of the s-polarized pulse with the overdense plasma does not generate any high order harmonics.

In the case of relativistic laser-plasma interaction, the HOHG mechanism described by the "oscillating mirror" model dominates. In this regime the high order harmonics frequencies in the case of the p-polarized excitation pulse are not limited by the plasma frequency ω_p. Additionally, in contrast to the non-relativistic regime the high order harmonics can be generated by the s-polarized pulse interacting with the overdense plasma.

The aim of this experiment is to observe the theoretically predicted transition of HOHG from the non-relativistic to the relativistic regime. The presentation of the experimental results is divided in two parts. In the first part HOHG in the case of the p-polarized excitation pulse is considered. In the second part the experiments with the s-polarized excitation pulse are presented. The experimental results are summarized in conclusion of this section.

In the first part of this experiment the p-polarized beam at 400 nm and approx. 50° incidence angle is focused on the polystyrene target. Pulses with tuneable energy up to 20 mJ and pulse duration of 45fs FWHM are used. The highest achieved peak intensities are in the order of $1.5\ 10^{19}$ W/cm², the corresponding normalised vector potential "a" is 1.3.

Two measured spectra of the high order harmonics and transmission of the aluminium filter are shown in figure 3.VII. In both cases the harmonics were generated with p-polarised excitation pulses at peak intensities of 1.5 10^{19} W/cm^3 (dashed, red line) and 5 10^{18}W/cm³ (solid, green line). The corresponding vector potentials are a=1.3 and a=0.8, respectively.

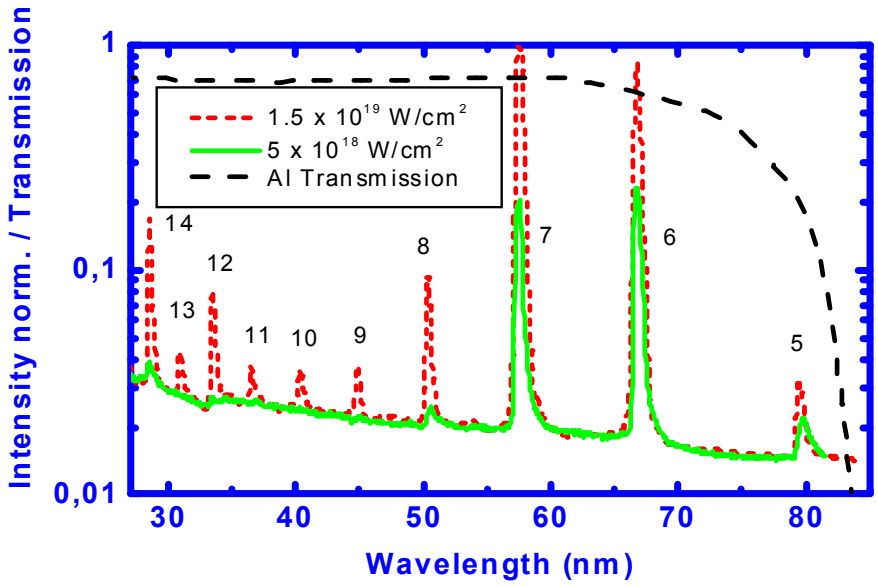

Figure **3.VII** Measured spectra of the generated harmonics above (a=1.3 red curve) and below (a=0.8 green curve) the relativistic threshold. The dashed black line denotes the transmission of the aluminium filter.

Spectra shown in figure 3.VII confirm the theoretical predictions discussed in chapter 2. In the non-relativistic regime (a=0.8) described by the "resonance" mechanism of HOHG the spectrum of the generated radiation cuts off at the plasma frequency ω_p. The plasma frequency corresponds to the optical wavelength 58 nm which is very close to the 7th harmonic (57 nm). In contrast, in the case of the relativistic beam intensity (a=1.3) the harmonics frequencies are not limited by the plasma frequency, as is predicted by the "oscillating mirror" model. Thus, the observation of harmonics with frequencies higher than the plasma frequency is strong evidence of the laser-plasma interaction in the relativistic regime.

Further, the measured energy conversion efficiencies are compared with the results of the PIC simulation, see figure 3.VIII. Following PIC simulation parameters were used: $L/\lambda=0.2$ and normalized vector potentials a=0.3 and a=0.7. The solid line represents the calculated harmonic efficiency. The filled circles correspond to the measured energy conversion efficiency. The dashed line marks the plasma frequency.

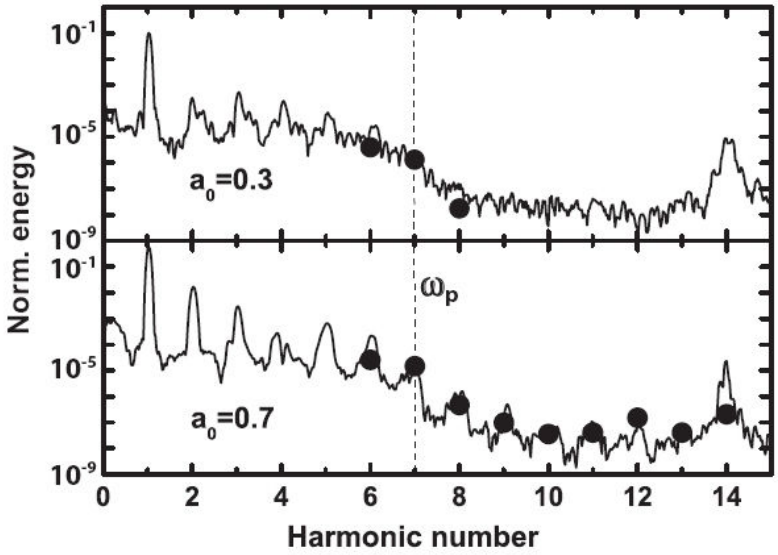

Figure **3.VIII** PIC simulated harmonic spectrum (solid lines) compared with the experimental data (circles). Dashed line marks the plasma frequency. PIC parameters are: $L/\lambda=0.2$, $n/n_c=49$, angle of incidence is 45° and a=0.3, a= 0.7 for the upper and bottom panels, respectively. The data presented in this figure are already published in [16].

In this experiment not only qualitative, but also excellent quantitative agreement of the experimental data with the PIC simulations results was achieved.

Additionally, the angular dependence of the harmonics intensity is measured to study the collimation properties of the generated radiation. The angular dependencies of the 6th and 7th harmonics intensities are measured (figure 3.IX).

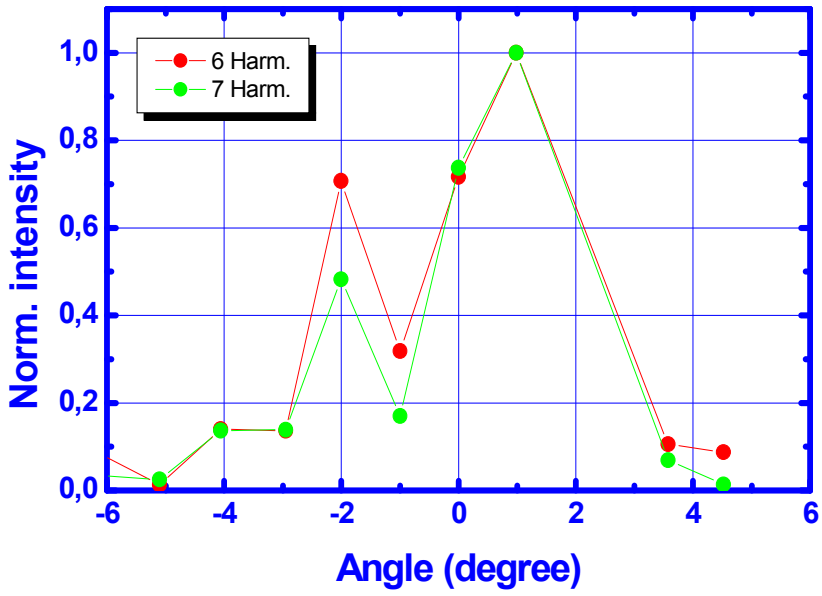

Figure **3.IX** Measured angular intensity dependence of the 6th and 7th harmonics

Assuming HOHG efficiency dependence on the incidence angle to be negligible over that angular range, the following can be concluded. The harmonics are emitted in a cone with the angle of ca. 5 degrees (FWHM), which is significantly smaller than the cone angle of the incident beam approx. 11 degrees (FWHM). The emitted radiation is well collimated and thus it is coherent.

In the second part of this experiment the s-polarized beam at 400 nm and ca. 50° incidence angle is focused on the target surface. Pulses with an energy of 20 mJ and pulse duration of 45fs FWHM are used. The highest achieved peak intensity is in the order of 1.5 10^{19} W/cm², the corresponding normalised vector potential "a" is 1.3.

The measured spectrum of the generated radiation is presented in figure 3.X.

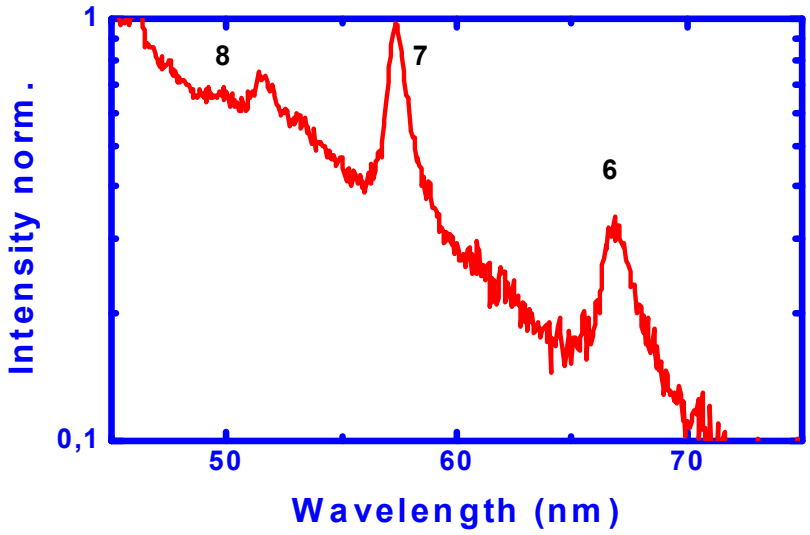

Figure **3.X** Harmonic spectrum integrated over 40 pulses generated by the s-polarised pump beam.

Harmonics with efficiency of approximately 10^{-10} in the relativistic regime (a=1.3) are detected. The presented spectrum is integrated over 40 pulses. To best of our knowledge it is the first experimental verification of HOHG in reflection geometry from solid targets with s-polarized excitation pulses. In the non-relativistic regime no harmonics are detected.
As discussed in the theoretical part concerning the "oscillating mirror" model, in the case of the s-polarized pump beam the reflecting surface oscillations are driven by the magnetic field. Thus, the detected harmonics are clear evidence of the relativistic interaction where $v \times B$ force plays a significant role.

The efficiency of HOHG excited by the p-polarized pulse is much higher than that in the case of the s-polarized excitation pulse. Thus, for the discussion of HOHG during the interaction of the s-polarized excitation pulse with the solid targets it is essential to estimate the pulse polarization in the focus. The problem is that even the pure vertically (s-) polarized beam, through collimation with the short focus off axis parabolic mirror, can produce significant fraction of the horizontally (p-) polarized radiation in the focus.

There are two possible reasons for the appearance of the horizontally polarized electromagnetic wave in the focus. The first one is of pure geometrical origin, the second is based on the phase shift of the reflected beam described by the Fresnell formulas.

The polarization of the radiation in focus is measured in the following way, see figure 3.XI.

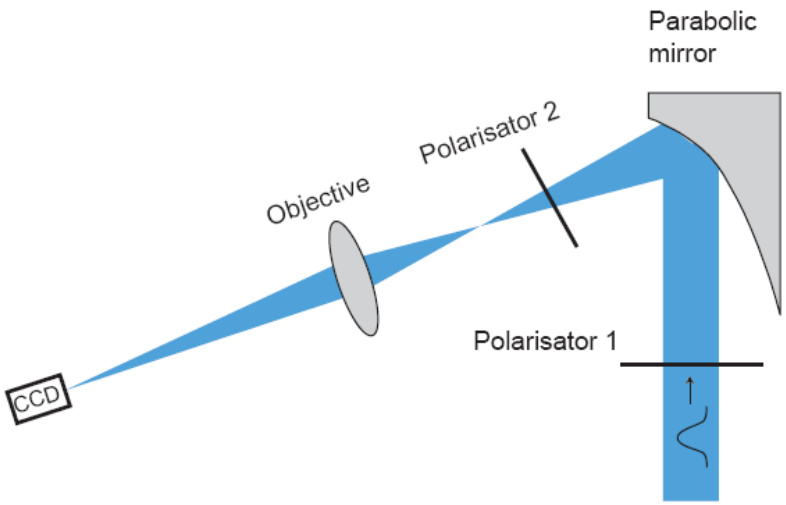

Figure **3.XI** Geometry used to measure the fraction of the horizontally polarized radiation in the focus of the parabolic mirror

The vertically polarized beam is focused with the same parabolic mirror as used in the experiments. The focus is imaged with the help of one objective on the CCD. To ensure the pure vertical polarization of the incident beam one (first) polarisator is installed in front of the parabolic mirror. One additional (second) polarisator is placed shortly before the focus. In the first step the maximal intensity detected by the CCD in the case of the horizontally polarized

radiation transmitted through the second polarizer is recorded. In the second step the same measurement is repeated but with the rotated second polarizer in such a way that only vertically polarized radiation is transmitted. The maximal intensity measured in the first step was 10^{-3} fraction of the intensity measured in the second step, i.e. the fraction of the p-polarized radiation in the focus of the s-polarized beam is 10^{-3}.

Returning to HOHG experiment with the s-polarized pump beam, the intensity of the s-polarized beam is of the order 10^{19} W/cm³. This means that in the focus the intensity of the p-polarized fraction of the radiation is approx. 10^{16} W/cm³. Although we believe it, the conclusion that the harmonics are generated by the s-polarized excitation pulse has to be verified. Nevertheless, the appearance of HOHG in the case of the s-polarized excitation beam is additional evidence of the laser-plasma interaction in the relativistic regime.

In conclusion the experimental results presented in this section are summarized.

In the first part of this experiment the spectra of the high order harmonics in the cases of intensive (a=0.8 and a=1.3) p-polarized excitation pulses are measured (Figure 3.VII). In contrast to the case a=0.8, the spectrum generated at a=1.3 experiences no cut off at the plasma frequency ω_p. The observation of harmonics with frequencies higher than the plasma frequency is strong evidence of laser-plasma interaction in the relativistic regime.
The efficiency of the measured HOHG is in excellent agreement with the results of the PIC calculation, see figure 3.VIII.
The measured high order harmonics are well collimated (figure 3.IX). Thus, in this experiment the generation of **coherent** high order harmonics is observed.

In the second part of this experiment HOHG in the case of excitation with an intensive (a=1.3) s-polarized pulse is verified. To our knowledge, it is the first observation of HOHG in reflection geometry from solid targets with s-polarized excitation pulses. The appearance of HOHG in the case of the s-polarized excitation beam is clear evidence of laser-plasma interaction in the relativistic regime.

Some experimental data, shown in this section are published in [16].

3.3 Two pulse mixing experiment

In this section the results of the pulse mixing experiment are described. The three wave mixing process is well understood and can be found in standard books on non-linear optics [49]. The goal of this experiment is to verify the new wave mixing mechanism. In this experiment the wave mixing occurred as a result of interaction of the laser pulses with an overdense plasma surface in the relativistic regime. The laser plasma interaction in the relativistic regime can be described by the "oscillating mirror" model, see section 1.2. In this section the discussion on the two pulse mixing experiment is based on the "oscillating mirror" model of HOHG.

In numerous reported experiments concerning HOHG in reflection geometry, only one pulse is used [12, 13, 19,20]. From the point of view of the oscillating mirror model, this means that one pulse is used to drive the oscillating mirror and at the same time is reflected on it. The idea is to use an intensive SH pulse to make the mirror oscillate and to reflect a relatively weak fundamental pulse on it. Thus, in the pulse mixing experiment two pulses are used: the relatively weak probe pulse at 800 nm (fundamental) and the intensive pump pulse at 400 nm (SH). With the help of the optical delay line, the pulses were temporarily overlapped. Both beams were focused with one parabolic mirror onto the surface of the polystyrene target. The angles of incidence were ca. 50° and 70° for the SH and the fundamental beams, respectively. The peak intensities of the p-polarized SH and the p-, or s-polarized fundamental pulses were 1.5 10^{19} W/cm^2 and 10^{17}W/cm^2, respectively. The harmonics spectra generated in the pulse mixing experiment are illustrated in figure 3.XII. The spectra shown in the left graph are generated by the p-polarized SH and fundamental pulses. The case of the p-polarized SH pulse and the s-polarized fundamental pulse is presented in the right graph. The spectra generated with the pump and the probe beams simultaneously are shown by the red curves. The green curves represent the spectra produced by the pump (SH) pulse alone. In the case of the excitation with the single probe (fundamental) pulse, no high order harmonics could be detected.

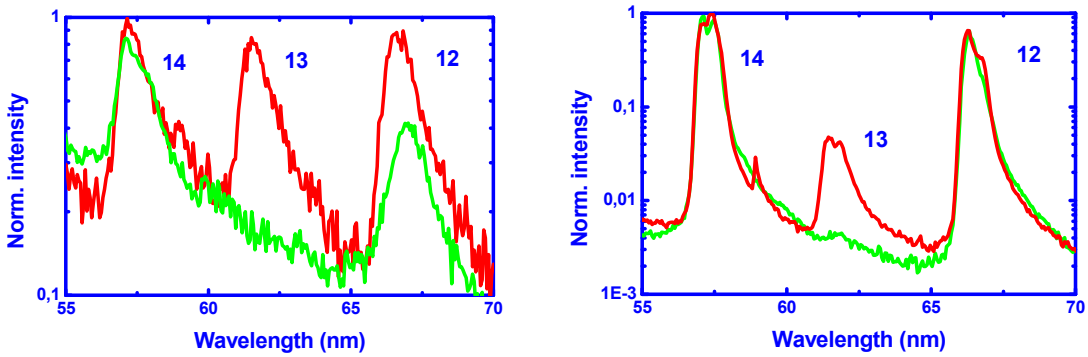

Figure **3.XII** Harmonics spectra produced in two pulse mixing experiment. Left graph: the pump and the probe pulses are p-polarized; Right graph: the pump pulse (SH) is p-polarized; the probe pulse (fundamental) is s-polarised. The spectra produced by the both pulses simultaneously (red curve) are compared with the spectra generated by the SH pulse (green curve).

The appearance of the 13th harmonic (in respect to the 800 nm beam) in the case of two interacting pulses is clear evidence of the modulation of the probe beam by the oscillating plasma mirror.
According to the oscillating mirror model, the frequencies of the mixed harmonics are the sum of the probe beam frequency and the multiples of the mirror oscillation frequency.

$$\omega_{mix} = \omega_{probe} + h\,\omega_{mirror} \qquad (3.2)$$

In this experiment the mirror oscillation is excited by a p-polarized SH pulse. Thus, the mirror oscillates with the optical frequency of the SH ($\omega_{mirror} = 2\omega_0$). The fundamental beam is reflected on the oscillating mirror ($\omega_{probe} = \omega_0$). In this case the total expected harmonics spectrum consists of multiples of SH frequencies (even harmonics) generated by the SH pulse alone, as well as that shifted by the fundamental frequency (odd harmonics) generated by the SH and fundamental pulse together.

Moreover, the intensity of the odd (13th) harmonic is comparable to the intensity of the even harmonics, although the intensity of the probe (fundamental) pulse is two orders of magnitude smaller than the intensity of the pump (SH) pulse.

Further, the angular spread of the generated harmonics is considered.
The direction of harmonic propagation can be obtained from the momentum conservation condition

$$\mathbf{k}_{(2h+1)\omega} = h\mathbf{k}_{2\omega} + \mathbf{k}_{\omega} \qquad (3.3)$$

where $\mathbf{k}_{(2h+1)\omega}$, $\mathbf{k}_{\omega}$ and $\mathbf{k}_{2\omega}$ represent the wave vectors of the $(2h+1)^{th}$ harmonic, the fundamental and the SH beams, respectively. Additionally the direction of the generated harmonic can be calculated using the relation (1.16) discussed in section1.1.

The angle between the 13^{th} harmonic propagation direction and the reflected SH beam direction is calculated using the formula (1.16) to be approx. 1.2°. The even harmonics are assumed to propagate in the specular direction of the SH beam.
The measured angular distributions of the 12^{th} and the 13^{th} harmonics are depicted in figure 3.XIII.

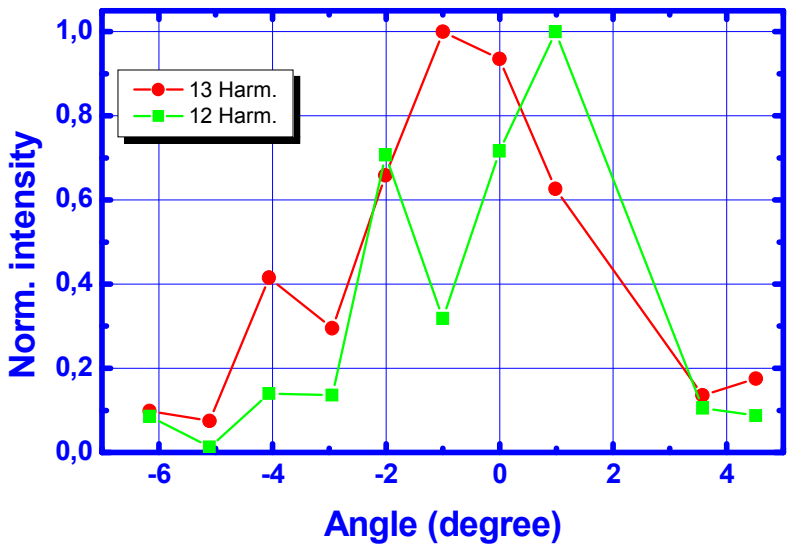

Figure **3.XIII** Measured angular intensity dependence of the 12^{th} and 13^{th} harmonics.

The 12th and the 13th harmonics shown in figure (3.XIII) are shifted in respect to each other by an angle smaller than 2 degrees. The theoretically estimated angle of 1.2 is well within the measurement error. The angular resolution is 2°.
Further, the 13th harmonic is emitted in a cone with an angle of ca. 5° FWHM. That angle is smaller than the cone angles of incident beams, 11° FWHM in the case of the SH and 8° in the case of the fundamental pulse. Thus, the produced 13th harmonic is well collimated, and consequently the emitted radiation is coherent.

According to the picture of the "oscillating mirror" model, the (mixed) 13th harmonic should be the result of the simultaneous interaction of the SH and the fundamental pulses with the overdense plasma. To verify this statement the intensity of 13th harmonic is recorded as a function of the delay time between the incident pulses (figure 3.XIV).

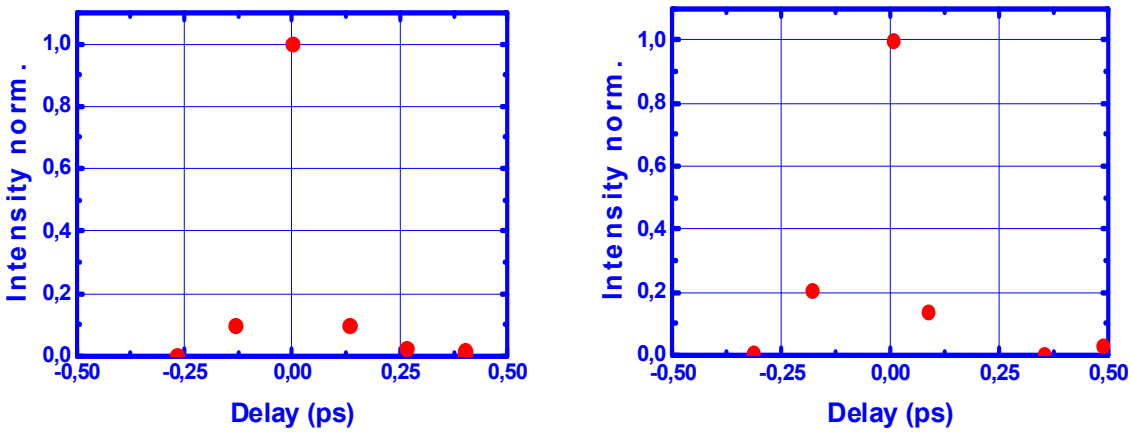

Figure **3.XIV** Intensity of the 13th harmonic as a function of the delay time between the incident pulses. Left graph: pump and probe pulses are p-polarized; Right graph: p-polarized pump and s-polarized probe pulses.

The graphs in figure 3.XIV confirm that the 13th harmonic is generated only during the simultaneous interaction of the incident pump and probe pulses with the plasma, in the way it was predicted by the "oscillating mirror" model.

In conclusion of this section the experimental results of the pulse mixing experiment are summarized. Firstly, the results of the "wave mixing" experiment are in a good qualitative agreement with the "oscillating mirror" model.

The spectra presented in this section reveal the appearance of the odd harmonics generated only in the case of the simultaneous interaction of the probe and pump pulses with the overdense plasma.

Secondly, the measured intensity dependence of the odd harmonics on the delay time between the pump and probe pulses confirm the necessity of the simultaneous interaction of the both pulses for the generation of the mixed harmonics.

The measured angular distribution of the mixed harmonic reveals the collimation of the radiation within the cone of 5° FWHM, and consequently confirms the coherence of it.

Moreover the intensity of the mixed (odd) harmonics is comparable to the intensity of the even harmonics, although the intensity of the probe pulse is 2 orders of magnitude smaller than the intensity of the pump pulse.

Finally, the data recorded in this experiment are qualitatively independent on the polarisation of the probe beam.

3.4 Measurement of HOHG efficiency as a function of the scale length L

In this experiment the scale length dependence of HOHG efficiency is investigated. For this purpose the p-polarized fundamental and SH pulses were focused on the target surface. The angles of incidence were approx. 50° and 70° for the SH and the fundamental beams, respectively. The peak intensities of the SH and fundamental pulses were 1.5 10^{19} W/cm^2 and 10^{16} W/cm^2, respectively. The fundamental pulse was used as an artificial prepulse to produce the plasma. Thus, the plasma generated by the fundamental pulse expanded to scale length L before the delayed SH pulse interacted with it. The estimated electron temperature in the plasma generated by the intensive (10^{17}W/cm²) pulse is in the order of T_e=1.6 10^{-16} J (T_e= 10^3 eV) [60]. According to the isotherm model of the plasma expansion in vacuum (described in [33]) the expansion velocity of the plasma ($v_{th} = \delta L/\delta t$) is

$$v_{th} = \sqrt{Z \cdot T_e / M} \ . \qquad (3.4)$$

The equation 3.4 evaluated for the polystyrene (C_8H_8), assuming complete ionization, yields the expansion velocity v_{th}= 0.088 λ/ps (λ = 400nm). Z and M are the charge number and the mass of the polystyrene molecule. Thus, the delay time Δt corresponding to the plasma scale length L can be obtained according to $L = v_{th}\,\Delta t$.

The energy of the harmonic pulses as a function of the time delay between the pulses is recorded, i.e. the efficiency of HOHG is measured as a function of the scale length L (figure 3.XV).

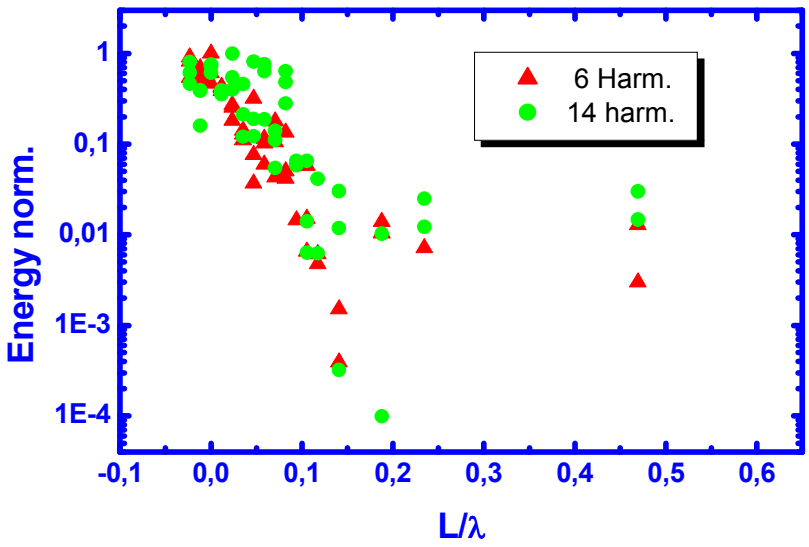

Figure **3.XV** Measured energy dependence of the 6th and the 14th harmonics on the normalized scale length L (λ = 400 nm).

Qualitatively the measured dependence of HOHG efficiency on the scale length is in good agreement with the calculated one, figures 1.XII and 3.XV.

According to the PIC calculation presented in chapter 1.4 two regions with qualitatively different mechanisms of HOHG can be distinguished:

In the first region ($0<L/\lambda<0.1$) the high order harmonics are generated in a non-relativistic regime. The corresponding laser plasma interaction can be described by the "resonant" mechanism of HOHG. In this scale length region the plasma restoring force is very strong. Thus the origin of the high order harmonics can be attributed to the strongly nonlinear motion of the plasma electrons (nonlinear currents).

In the second region ($0.1<L/\lambda<0.5$) the high order harmonics are generated in a relativistic regime. HOHG in this case can be described by the "oscillating mirror" model. In this scale length region the plasma restoring force in the tail of the expanded plasma is significantly weaker compared with the restoring force in the first region, resulting in the electron

excursion being comparable to the wavelength λ. The generation of the high order harmonics in this case can be contributed to the relativistic retardation effects.

In conclusion of this section the result of this experiment is shortly interpreted.
In the previous measurements only in the first scale length region of the generation of the high order harmonics could be experimentally verified [10]. In contrast to the earlier experiments in this experiment HOHG in both PIC predicted regions was observed. The appearance of significant HOHG efficiency in the second region is an additional proof of the relativistic laser-plasma interaction regime in these experiments.

The experimental data, shown in this section are published in [16].

4 Conclusion

In the interaction experiments of laser pulses with an overdense plasma surface the generation of **coherent high order harmonics in the relativistic regime** has been verified.

In particular, the observation of harmonics generation with optical frequencies higher than the plasma frequency ω_p is strong evidence of laser plasma interaction in the relativistic regime (section 3.2). Moreover, the experimentally proved generation of high order harmonics in the case of s-polarized excitation pulses is clear evidence of the relativistic HOHG regime (section 3.2). Finally the experimentally verified appearance of HOHG in the second scale length region is additional strong evidence of the relativistic laser-plasma interaction regime in these experiments (section 3.4).

Additionally, the relativistic pulse mixing mechanism has been observed (section 3.3). The results of the pulse mixing experiment open up additional options and ways of generating the single attosecond pulses.

In general the presented experimental results are in good agreement with the predictions of the PIC simulations and the “oscillating mirror” model.

References

1 G. Mourou, T. Tajima, S. Bulanov, *Optics in the relativistic regime*, Rev. Mod. Phys. 78, 309, (2006)

2 N. M. Naumova, J. A. Nees, I. V. Sokolov, B. Hou, G. A. Mourou, *Relativistic Generation of Isolated Attosecond Pulses in a λ^3 Focal Volume*, Phys. Rev. Lett., 92, 063902 (2004)

3 G. Tsakiris, K. Eidmann, J. Meyer-ter-Vehn, F. Krausz, *Route to intense single attosecond pulses*, New J. Phys., 8, 19 (2006)

4 S. Gordienko, A. Pukhov, O. Shorokhov, T. Baeva, *Relativistic Doppler Effect: Universal Spectra and Zeptosecond Pulses*, Phys. Rev. Lett. **93**, (11) 115002 (2004)

5 S. Gordienko, A. Pukhov, O. Shorokhov, T. Baeva, T. Baeva, *Coherent Focusing of High Harmonics: A New Way Towards the Extreme Intensities*, Phys. Rev. Lett. 94 103903 (2005)

6 E. Chang, A. Rundquist, H. Wang, M. Murnane, H. Kapteyn, *Generation of Coherent Soft X Rays at 2.7 nm Using High Harmonics*, Phys. Rev. Lett. **79**, 2967-2970 (1997)

7 U. Shymanovich *Direct observation of ultra fast atomic motion using time-resolved X-ray diffraction Dissertation* (2007).

8 P.Maine, D. Strickland, P. Bado, M. Pessot, G Mourou, *Generation of ultrahigh Piak Power Pulses by Chirped Pulse Amplification*, IEEE J. of Qual. Electr. QE-24 (2), 398-403 (1998)

9 S. Backus, G. Durfee, H. C. Kapteyn, and M. M. Murnane, *High Power Ultrafast Laser*, Rev. Sci. Instr. 69, 1207-1220 (1998)

10 C. Dietrich, *Erzeugung Harmonischer hoher Ordnung an steilen Plasma-Dichtegradienten*, Dissertation (2004)

11 A. Tarasevitch, C Dietrich, D. von der Linde, *High order Harmonics from Plasma Surfaces* Lectures in Strong Field Physics, ed. T. Brabec and H. Kapteyn, Springer Verlag 2007

12 D. von der Linde, K. Rzazewski, *High-order harmonic generation from solid surfaces*, App. Physics B **63**, 135-319 (1998)

13 D. von der Linde, *Generation of High Order Optical Harmonics from Solid Surfaces*, Appl. Physics B 68, 315-319 (1998)

14 A. Orisch, *Erzeugung hoher Harmonischer an Festkörperoberflächen mit fs-Laserimpulsen*, Dissertation (2000)

15 A. Tarasevitch, C. Dietrich, C. Blume, K Sokolowski-Tinten, D. von der Linde, *3/2 harmonic generation by femtosecond laser pulses in steep-gradient plasmas*, Phys. Rev. E **68** 02641 (2003)

16 A. Tarasevitch, K. Lobov, C. Dietrich, D. von der Linde, *Transition to the Relativistic Regime in High Order Harmonic Generation*, Phys. Rev. Lett. **98**, 103902 (2007).

17 P. A. Norreys*, Efficient Extreme UV Harmonics Generated from Picosecond Laser Pulse Interactions with Solid Targets*, Phys Rev Let. **76**, 1832 (1996)

18 G. D. Tsakiris, K. Eidmann, J. Meyer-ter-Vehn, F. Krausz, *Route to intense single attosecond pulses*, New Journal of Phys **8** (2006)

19 M Zepf, et al. *Role of the plasma scale length in the harmonic generation from solid targets*, Phys. Rev E **58**, 5254 (1998).

20 A. Tarasevitch et al. *Generation of high-order spatially coherent harmonics from solid targets by femtosecond laser pulses* Phys. Rev. A 62, 023816 (2000)

21 L. Rosso, L. Plaja, K. Rzazwski, D. v. d. Linde, *Beyond the moving mirror model: Attosecond pulses from a relativistically moving plasma*, Laser and Particles Beams, Cambridge University Press (2000)

22 P. Gibbon, *High-Order Harmonic Generation in Plasmas*, IEEE of QE **33**, 1915-1924 (1997)

23 R. Lichters, J. Meyer-ter-Vehn, A. Pukhov, *Short-pulse laser harmonics from oscillating plasma surfaces driven at relativistic intensity*, Phys. Plasmas **3** (9), 3425-3437 (1996)

24 S.V. Bulanov, N. M. Naumova, Pegoraro, *Interaction of an ultrashort, relativistically strong laser pulse with an overdense plasma*, Phys. Plasma **1** (3), 745-754 (1994)

25 F. Quéré, C. Thaury, P. Monot, S. Dobosz, Ph Martin, Coherent Wake Emission of High-Order Harmonics from overdense Plasmas, Phys Rev. Lett. **96**, 125004 (2006).

26 R. Bezzarides, D. Jones, W. Forslund, *Plasma Mechanism for Ultraviolet Harmonic Radiation Due to Intense CO_2 Light*, Phys. Rev. Lett., **49**, 202 (1982)

27 C. Birdsall, A. Langdon, *Computer simulations doing plasma physics*, IOP Publishing Ltd (1991)

28 R. L. Carman, D. W. Forslund, J. M. Kindel, Visible Harmonic Emission as a Way of Measuring Profile Steepening, Phy. Rev. Lett **49**, 202 (1981)

29 K. Rzazewski, L. Plaja, L. Rolo, D. von der Linde*, Probe-field reflection on a plasma surface driven by a strong electromagnetic field*, J Phys. B **33**, 2549-2558 (2000)

30 V. Vshivkov, N. Naumova, F. Pegoraro, S. Bulanov, *Nonlinear electrodynamics of the interaction of ultra-intense laser pulses with a thin foil*, Phys of plasmas **5** (7) 2727-2741 (1998)

31 L. Landau, E. Lifshitz, *The classical theory of fields*, Pergamon press, Oxford, (1975)

32 R. Lichters, *Relativistische Wechselwirkung intensiver kurzer Laserpulse mit überdichten Plasmen: Erzeugung hoher Harmonischer*, Dissertation (1997).

33 W. Kruer, *The interaction of laser with plasma*, Addision Wesley (1980)

34 K. Eidman, R. Sigel, *Second-Harmonic Generation in an Inhomogeneous Laser-Produced Plasma*, Phys. Rev. Lett. **34**, 799 (1975)

35 E. A. McLean, J. A. Stamper, B. H. Rippin, H. R. Griem, J. McMahon, S. E. Bodner, *Harmonic generation in Nd : laser-produced plasmas*, Appl. Phys. Lett. **31,** 825 (1977).

36 N. H. Burnett, H. A Baldes, *Harmonic generation in CO2 laser target interaction*, Appl. Phys. Lett. **31,** 172 (1977).

37 R. L. Carman, D. W. Froslund, J. M. Kindel, *Visible Harmonic Emission as a Way of Measuring Profile Steepening*, Phys. Rev. Lett. **46,** 29 (1981)

38 R. L. Carman, C. K. Rhodes, R. F Benjamin, *Observation of harmonics in the visible and ultraviolet created in CO2-laser-produced plasmas*, Phys. Rev. A **24,** 2649 (1981)

39 Z. M. Sheng, K. Mima, J. Zhang, H. Sanuki, *Emission of Electromagnetic Pulses from Laser Wakefields through Linear Mode Conversion*, Rhys. Rev. Lett. **94**, 095003 (2005)

40 Z. M Sheng, K. Mima, J. Zhang, *Powerful terahertz emission from laser wake fields excited in inhomogeneous plasmas*, Phys. Plasmas **12**, 123103 (2005)

41 D. von der Linde, *Second harmonic production from solid targets*, Lecture in Laser interactions with Atoms, Solids, and Plasmas, ed. M. More, Plenum Press (1994)

42 U. Teubner et al., *Harmonic Emission from the Rear Side of Thin Overdense Foils Irradiated with Intense Ultrashort Laser Pulses*, Phys. Rev. Lett. 92, 185001 (2004)

43 K. Eidmann et al., *Fundamental and harmonic emission from the rear side of a thin overdense foil irradiated by an intense ultrashort laser pulse*, Phys. Rev. E **72**, 036413 (2005)

44 R. Lichters, J. Meyer-ter-Vehn, High Laser Harmonics from Plasma Surfaces: *Intensity and Angular dependence, Cutoffs and Resonance Layers at Density Ramps*, Institute of Physics Conference Series **154**, Inst. Phys. Publ. Bristol, 221-230 (1997)

45 W. E. White, F. G. Patterson, *Compensation of higher-order frequency-dependent phase terms in chirped pulse amplification systems*, Optics Letters **18**, 1343-1354 (1993)

46 C Dietrich, *Erzeugung ultrakurzer Laserimpulse und deren Verstärkung in den Terawatt Bereich*, Diploma (1999)

47 O. Svelto, *Principles of Lasers*, Plenum Press (1989)

48 J. Queneuille, F. Druon, A. Maksimchuk, G. Cheriaux, G. Mourou, *Second-harmonic generation and wave-front correction of a terawatt laser system*, Opt. Let. **25**, 508-510 (2000)

49 Y. Shen, The *Principles of Nonlinear Optics*, Willey-Interscience Publication (1984)

50 W. L. Kruer, *The Physics of Laser Plasma Interactions*, Addison-Wesley (1988).

51 N. G. Denisov, *On a singularity of the field of an electromagnetic wave propagated in an inhomogeneous plasma*, Sov, Phys. JETP **4**, 544 (1975)

52 V. L. Ginzburg, *Propagation of Electromagnetic Waves in Plasma*, Gordon and Brach, New York (1961).

53 E. Sidick, A. Knoesen and A. Dienes, *Ultrashort-pulse second-harmonic generation I. Transform-limited fundamental pulses*, J.Opt. Soc. Am. B **12**, 1704-1712 (1995)

54 E. Sidick, A. Knoesen and A. Dienes, *Ultrashort-pulse second-harmonic generation II. Non-transform-limited fundamental pulses*, J.Opt. Soc. Am. B **12**, 1713-1722 (1995)

55 A. Marcinkevicius, R Tommasini, G. D. Tsakiris, K.J, Witte, E. Gaizauskas, U Teubner, *Frequency doubling of multi-terawatt femtosecond pulses,* Appl. Phys. B **79**, 547-554 (2004)

56 V. Krylov, A. Rebane, A. G. Kalintsev, H. Schwoerer, U. P. Wild, *Second-harmonic generation of amplified femtosecond Ti:sapphire laser pulses*, Optics lett. **20**, 198 (1995)

57 I. A. Begishev, M. Kalashnikov, V. Karpov, P. Nickles, H. Schönnagel, I. A. Kulagin, T. Usmanov, *Limitation of second-harmonic generation of femtosecond Ti:sapphire laser pulses*. J. Opt. Sec. Am. B **21**, 318 (2004)

58 SNLO nonlinear optics code available from A. V. Smith, Sandia National Laboratories, Albeqerque, NM87185-1423

59 A Wloka, *Steuerung der Parameter der hochintensiven femtosekunden Laserstrahlung mit Hilfe eines adaptiven optischen Systems*, Diploma (2005)

60 U. Teubner, C. Wülker, W. Theobald, E. Förster*, X-ray spectra from high-intensity subpicosecond laser produced plasmas*, Phys. Plasmas **2**, 972 (1995)

61 J. Hollandt, M. Kühne, B. Wende, *High-current hollow-cathode source as a radiant intensity standard in the 40-125-nm wavelength range, Applied optics* **33,** 68 (1994)

62 V. Kaufman, W Whaling, *Improved Wavelengths and Energy Levels of Doubly-Ionized Argon (AR III)* J. Res. Natl. Stand. Technol. **101,** 961 (1996)

63 W. Whaling, W Anderson, M. Carle, J Brault, H. Zarem, *Argon I Lines Produced in a Hollow Cathode Source, 332nm to 5865 nm*, J. Res. Natl. Inst. Stand. Technol. **107**, 149-169 (2002)

64 V. Baggio-Scheid, A. Paes, J. Neri, *Study of Excitation Rates in a Hollow Cathode Discharge*, Braz. J. Phys. **33**, 336 (2003)

65 M. Born, E. Wolf, *Principles of Optics*, sixth edition, Pergammon, section 9.2. (1980).

66 F. Zernike, *Beugungstheorie des Schneidenverfahrens und Seiner Verbesserten Form, der Phasenkontrast-methode*. Physica **1**, 689. (1934).

67 P. Y. Maeda, *Zernike Polynomials and their use in describing the wavefront aberrations of the Human Eye*, Course Project, Psych 221/EE 362 Stanford University (2003).

68 M. A. Murison, *Expansion of Wavefront Errors in an Infinite Series of Zernike Polynomials*, SAO Technical Memorandum TM95-04. (1995).

69 Articles in the encyclopedia "Wikipedia" at URL: www.wikipedia.org.

70 Saleh, Bahaa, Teich, Malvin, *Fundamentals of Photonics*, New York: John Wiley & Sons. (1991).

71 Mandel, Leonard, Wolf, Emil, *Optical Coherence and Quantum Optics*, Cambridge: Cambridge University Press (1995).

72 Siegman, Anthony, *Lasers*, University Science Books (1986).

73 F. Chen, *Introduction to plasma physics and controlled fusion*, Plenum Press (1974).

Appendixes

Appendix A1

Wave coupling (resonance absorption)

It can be shown that in the case of inhomogeneous plasma ($\nabla n \neq 0$), under certain conditions, the transverse electromagnetic and longitudinal electrostatic waves couple with each other. In the layer with the critical density $\omega = \omega_p$ it provides an efficient way of converting an electromagnetic wave into a localized electrostatic one. The consideration of the resonance absorption in this section is based on [41].

At the beginning some simplifying assumptions are made:

1) A one-dimensional, static ion density profile is assumed.
2) The electromagnetic wave incident on the plasma is quasi-monochromatic, and its amplitude is constant.
3) Absorption of light is taken into account by introducing a damping constant.

The light-plasma interaction is described by the Maxwell equations

$$\nabla \cdot \mathbf{E} = -4\pi e(n - ZN) \tag{A1.1a}$$

$$\nabla \cdot \mathbf{B} = 0 \tag{A1.1b}$$

$$\nabla \times \mathbf{E} = -\frac{1}{c}\frac{\partial}{\partial t}\mathbf{B} \tag{A1.1c}$$

$$\nabla \times \mathbf{B} = -\frac{4\pi}{c} en\mathbf{v} + \frac{1}{c}\frac{\partial}{\partial t}\mathbf{E} \tag{A1.1d}$$

combined with the equation of motion and continuity equation for the electrons

$$\frac{\partial}{\partial t}\mathbf{v} + \nu\mathbf{v} + (\mathbf{v}\cdot\nabla)\mathbf{v} = -u^2\frac{1}{n}\nabla n - \frac{e}{m}(\mathbf{E} + \frac{1}{c}\mathbf{v}\times\mathbf{B}) \qquad \text{(A1.1e)}$$

$$\frac{\partial}{\partial t}n + \nabla(n\mathbf{v}) = 0\,. \qquad \text{(A1.1f)}$$

Here **E**(x, t) and **B** (x, t) are magnetic- and electric fields strength. Z and N are the ion charge number and the ion-density, respectively. The electron-ion collision frequency and the electron velocity are denoted by ν and **v**. The first term on the r. h. s. of (A1.1e) represents the pressure force, where $u=(k_bT_e/m)^{1/2}$ is the mean thermal velocity. k_b is the Boltzmann constant and T_e is the electron temperature. In the equation of motion (A1.1e) for the electrons

(I)	the Lorenz force	e n (**E** + **v**/c × **B**),
(II)	the pressure gradient force	-∇p, and
(III)	the damping force	–m n ν **v**

are taken into account. Detailed derivation of (A1.1e) can be found in [49]. The electron acceleration is given by the total time derivative of the velocity:

$$\frac{d}{dt}\mathbf{v}(x,t) = \frac{\partial}{\partial t}\mathbf{v} + (\mathbf{v}\cdot\nabla)\mathbf{v} \qquad \text{(A1.2)}$$

The relation between the electron pressure p and the density n is given by the isothermal equation of state for the one-dimensional electron gas [50]:

$$p = nk_bT_e \qquad \text{(A1.3)}$$

The sources driving the electric and magnetic fields are represented by the term on the r.h.s. of (A1.1a) (the electric charge density) and the first term on the r.h.s. of (A1.1d) (the current density). Note, that the system of equations (A1.1) is nonlinear because of the product terms in the last three equations. These nonlinearities make it difficult to solve the set of coupled differential equations (A1.1) analytically. Further approximations have to be made.

If the charge density and the current density induced by the applied external fields are small in some sense, the response of the plasma may be obtained from perturbation treatment. In this case the electronic density and the velocity can be written in the form of a perturbation expansion:

$$n=n^{(0)}+n^{(1)}+n^{(3)}+\ldots \tag{A1.4a}$$

$$\mathbf{v}=\mathbf{v}^{(0)}+\mathbf{v}^{(1)}+\mathbf{v}^{(3)}+\ldots \tag{A1.4b}$$

Here, $n^{(0)}$ and $\mathbf{v}^{(0)}$ are the unperturbed values. The charge neutrality requires $n^{(0)}=ZN$, and $\mathbf{v}^{(0)}=0$ for a static ion distribution. The successive approximations can be calculated in the usual way by inserting (A.1.4) into (A1.1).

Let us now assume a periodic perturbation proportional to $\exp(-i\omega t)$, caused by the optical wave incident on the plasma. Inserting (A1.4) into (A1.1) and keeping terms up to the first order we obtain:

$$\nabla\mathbf{E}_1 = -4\pi e n_1^{(1)} \tag{A1.5a}$$

$$\nabla\mathbf{B}_1 = 0 \tag{A1.5b}$$

$$\nabla\times\mathbf{E}_1 = \frac{i\omega}{c}B_1 \tag{A1.5c}$$

$$\nabla\times\mathbf{B}_1 = \frac{4\pi}{c}(-en^{(0)}\mathbf{v}_1^{(1)}) - \frac{i\omega}{c}\mathbf{E}_1 \tag{A1.5d}$$

$$(-iw+\nu)\mathbf{v}_1^{(1)}n^{(0)} = -u^2\nabla n_1^{(1)} - \frac{e}{m}n^{(0)}\mathbf{E}_1 \tag{A1.5e}$$

Subscripts denote the Fourier components, i.e. $\mathbf{E}_1=\mathbf{E}(\omega)$ etc., and superscripts the order of the perturbation. Using (A1.5a) to substitute $n_1^{(1)}$ in (A1.5e) and taking into account the plasma frequency ω_p definition

$$w_p = \sqrt{\frac{4\pi e^2 n^{(0)}}{m}} \tag{A1.6}$$

and the expansion of the current **J**

$$\mathbf{J} = en\mathbf{v} = \mathbf{J}^{(1)} + \mathbf{J}^{(2)} + \ldots = -en^{(0)}\mathbf{v}^{(1)} - e(n^{(0)}\mathbf{v}^{(2)} + n^{(1)}\mathbf{v}^{(1)}) + \ldots \tag{A1.7}$$

the first order current density can be written as follows

$$\mathbf{J}_1^{(1)} = \frac{1}{4\pi}\frac{i}{\omega + i\nu}(\omega_p^2\mathbf{E}_1 - u^2\nabla\nabla\mathbf{E}_1) \tag{A1.8}$$

Further, equations (A1.5c), (A1.5d) and (A1.8) can be combined to obtain the following equation for the electric field $\mathbf{E}_1$.

$$\nabla\times\nabla\times\mathbf{E}_1 = \frac{\omega^2}{c^2}\varepsilon_1\mathbf{E}_1 + \frac{\omega}{\omega + i\nu}\frac{u^2}{c^2}\nabla\nabla\mathbf{E}_1 \tag{A1.9}$$

Here the Drude dielectric function $\varepsilon_1 = \varepsilon(\omega)$

$$\varepsilon(\omega) = 1 - \frac{\omega_p^2}{\omega(\omega + i\nu)} \tag{A1.10}$$

is introduced. The plasmas support both transverse electromagnetic and longitudinal quasi-electrostatic waves [73]. E_1 can be decomposed into two different components

$$E_1 = E_1^t + E_1^l, \tag{A1.11}$$

where E_1^t is the transverse, electromagnetic part with $\nabla E_1^t = 0$ and $\nabla \times E_1^t \neq 0$. And E_1^l is the longitudinal, "electrostatic" part with $\nabla E_1^l \neq 0$ and $\nabla \times E_1^l = 0$. Inserting the (A1.11) into (A1.9) and applying ∇ and $\nabla\times$ on the equation (A1.9) two coupled equations for the transverse and the longitudinal fields can be obtained.

$$(\Delta + \frac{\omega^2}{c^2}\varepsilon_1)(\nabla \times \mathbf{E}_1^t) = -\frac{\omega^2}{c^2}\nabla\varepsilon_1 \times (\mathbf{E}_1^t + \mathbf{E}_1^l) \qquad \text{(A1.12a)}$$

$$(\Delta + \frac{\omega^2}{u^2}\varepsilon_1)(\nabla \cdot \mathbf{E}_1^l) = -\frac{\omega^2}{u^2}\nabla\varepsilon_1 \cdot (\mathbf{E}_1^t + \mathbf{E}_1^l) \qquad \text{(A1.12b)}$$

Here the condition $\nu << \omega$ is assumed. Thus, $\varepsilon_1 \approx 1-\omega_p^2/\omega^2$ and the factor $\omega/(\omega+i\nu)$ in front of the ∇-operator in (A1.12b) is neglected. Since the quantities $\nabla\times \mathbf{E}_1^t$ and $\nabla\cdot\mathbf{E}_1^l$ are essentially magnetic field and electric charge density, the equations (A1.12a) and (A1.12b) can be considered as the wave equation of electromagnetic and charge density (plasma or Langmuir) waves.

In a homogeneous medium ($\nabla\varepsilon_1 = 0$) the equations (A1.12) are not coupled. In the inhomogeneous medium ($\nabla\varepsilon_1 \neq 0$) the electron plasma and electromagnetic waves are coupled. Thus, the inhomogeneous plasma with plasma waves will emit electromagnetic radiation, and vice versa. This process is efficient only if the resonance condition $\omega=\omega_p$ is satisfied. The transfer of energy from electromagnetic waves to the plasma waves is called resonant absorption. Some times it is also called linear conversion [51, 52].

Let us assume a flat plasma surface and the plasma electron density gradient normal to it. There is an important difference between the incident s- and p-polarized radiations interacting with the plasma. In the case of s-polarized light the polarisation vector of the radiation is parallel to the surface, thus in equation (A1.12b) $\mathbf{E}_1\cdot\nabla\varepsilon_1 = 0$, and consequently no wave coupling occurs. For the p-polarization $\mathbf{E}_1\cdot\nabla\varepsilon_1 \neq 0$, thus the p-polarized wave excites the electron plasma oscillation as discussed above.

Appendix A2

Hard Kerr-lens mode locked laser oscillator

An optical oscillator (optical cavity or optical resonator) is an arrangement of mirrors that forms a standing wave cavity resonator for the light waves, surrounding the gain medium (the active medium). The scheme of the Ti:Sa hard Kerr lens mode locked oscillator is shown in figure A2.I. In this case the resonator consists of two flat mirrors to reflect the radiation back, and two spherical mirrors to focus it in the gain medium (Ti:Sa crystal).

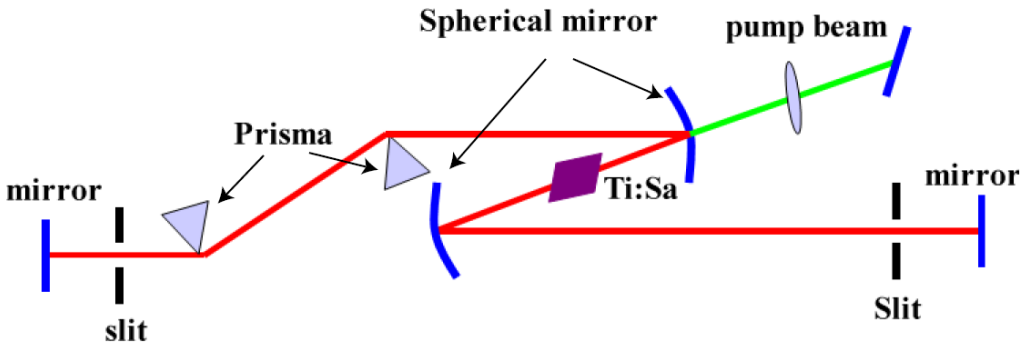

Figure **A2.I** Scheme of the Ti:Sa hard Kerr lens mode locked oscillator

The light confined in the resonator is reflected multiple times from the mirrors, and due to the interference, only certain patterns and frequencies of the radiation are sustained by the resonator. The others are suppressed by destructive interference. In general, the radiation patterns which are reproduced on every round-trip of the light through the resonator are the most stable and are the “eigenmodes”, known as the modes, of the resonator.
Resonator modes can be divided into two types: longitudinal modes, which differ in frequency from each other; and transverse modes, which may differ in both frequency and the transverse intensity pattern of the light. In the basic or fundamental transverse mode of resonator the beam has a Gaussian intensity profile.

Further, to discuss the hard Kerr-lens mode locked laser oscillator the Kerr effect has to be explained. The Kerr effect is the basis for the Kerr-lens modelocking. It was discovered in

1875 by John Kerr, a Scottish physicist. The Kerr effect or the quadratic electro-optic effect is a change in the refractive index of a material in response to an electric field. The induced index change is proportional to the square of the electric field. The optical Kerr effect (or AC Kerr effect) is the case in which the refrective index of material is changed because of the electric field of the light itself. This causes a variation in the index of refraction which is proportional to the local intensity of the light. The refractive index variation is responsible for the nonlinear optical effects such as self focusing and self-phase modulation.
Because of the Gaussian intensity distribution in a fundamental transverse mode of the resonator, the refractive index changes in the Ti:Sa crystal across the beam profile. The refractive index experienced by the beam is greater in the centre of the beam than at the edge. Therefore a rod of an active Kerr medium works like a lens for the high intensity light. This results in self-focusing and in extreme cases leads to material destruction.

In the laser cavity, because of their high peak intensity (and Kerr effect) the short laser pulses will be generated with a different intensity profile as continuous waves (cw). The oscillator could be made to favor the pulse over the cw regime (or mode). Such oscillators are called “mode-locked” oscillators. There are two types of mode locking.
In hard mode locked resonators the cw mode is simply cut by the aperture, or slit (figure A2.I, A2.II on the r.h.s). Thus the losses in the cw mode is higher than that in the pulse mode. In soft mode locked resonators the overlap between the pumped region of the gain medium and the beam in the pulse mode is better than the overlap between the pumped region and the beam in the cw mode, resulting in the higher gain of the pulse mode.

The shortest pulse length of the resonator is limited by the dispersion in the active medium. In order to reach the shortest pulse length, the dispersion of the second order is minimized with the help of a two prisms compressor (figure A2.I).

In the oscillator at the IEP the Ti:Sa crystal is “pumped” by the second harmonic Nd:YAG cw laser at λ=532 nm (figure A2.I green line).
The material of this section is based on [69].
A photograph of the oscillator which is installed at the IEP can be seen in figure A2.II

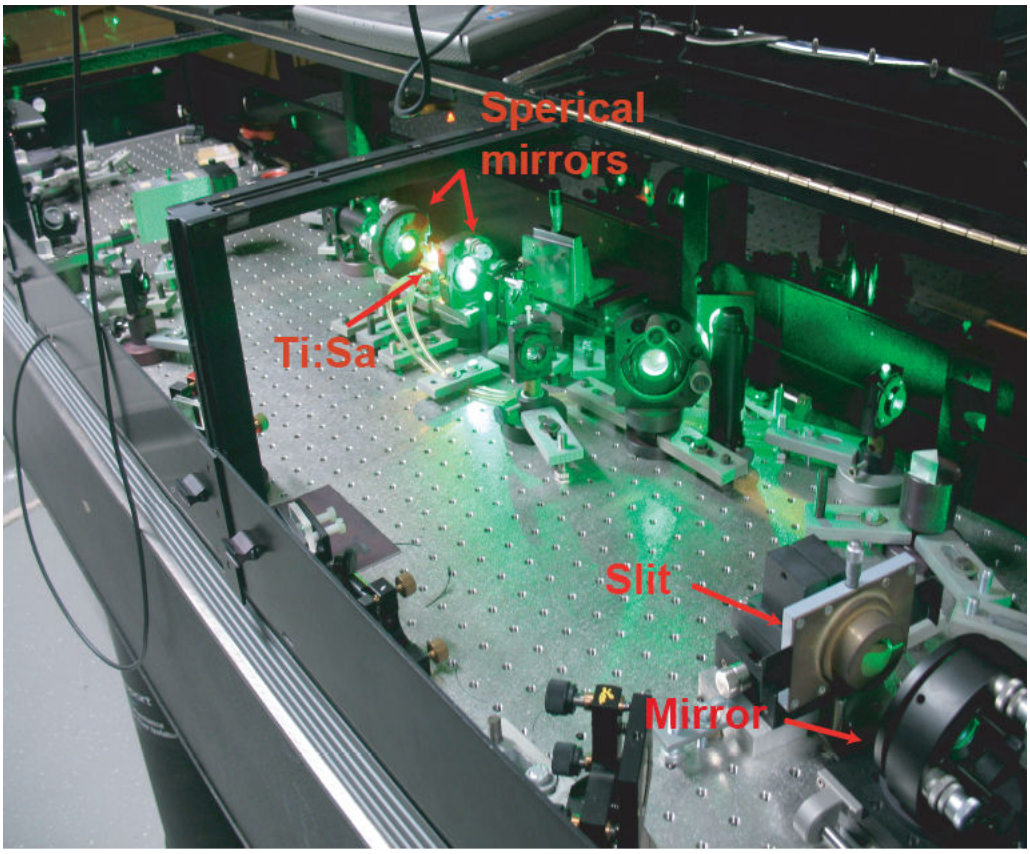

Figure **A2.II** Ti:Sa hard Kerr lens mode locked oscillator at the IEP

Appendix A3

Estimation of the bandwidth limited pulse duration

In the case of bandwidth-limited pulses (also known as Fourier-transform-limited pulses, or more commonly, transform-limited pulses) the Fourier transformation is the well known relation between the pulse shapes in the time and frequency domains. The Fourier transformation of a Gaussian function is a Gaussian function. Thus, assuming the Gaussian pulse intensity envelope in the time domain

$$I(t) = I_o \exp(-\frac{t^2}{b}) \qquad \text{(A3.1)}$$

one gets

$$E(t) = \sqrt{I(t)} = E_0 \exp(-\frac{t^2}{2b}) \qquad \text{(A3.2)}$$

where b is a positive constant. The following relations are valid in the frequency domain:

$$\widetilde{E}(\omega) \propto \exp(-\frac{\omega^2 b}{2}) \qquad \text{(A3.3)}$$

and

$$\widetilde{I}(\omega) \propto \exp(-\omega^2 b)\,. \qquad \text{(A3.4)}$$

Using relations (A3.1) and (A3.4) the FWHM values in the time (Δt) and frequency ($\Delta\omega$) domains can be calculated. First, the FWHM value in the time domain (see figure A3.I left) is figured out.

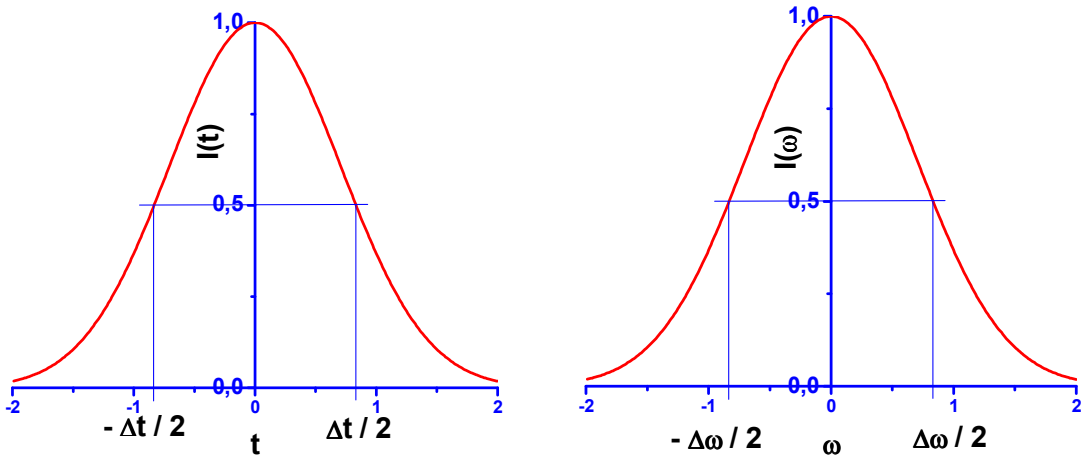

Figure **A3.I** Gaussian intensity distribution in the time domain (left) and in the frequency domain (right). In these graphs the constant $b = 1s^2$.

Starting from

$$\frac{1}{2}I_0 = I_0 \exp(-\frac{(\Delta t/2)^2}{b}) \qquad \text{(A3.5)}$$

the relation

$$\ln(2) = \frac{(\Delta t/2)^2}{b} \qquad \text{(A3.6)}$$

and the formula

$$\Delta t^2 = 4b\ln(2) \qquad \text{(A3.7)}$$

can be obtained. Analogously in the frequency domain (figure A3.I right), starting from

$$\frac{1}{2}\tilde{I}_0 = \tilde{I}_0 \exp(-(\Delta\omega/2)^2 b) \qquad \text{(A3.8)}$$

the relations

$$\ln(2) = \frac{\Delta\omega^2 b}{4} \tag{A3.9}$$

and

$$\Delta\omega^2 = \frac{4\ln(2)}{b} \tag{A3.10}$$

can be obtained. The product of the FWHM values in time (Δt) and frequency ($\Delta\omega$) domains is constant.

$$\Delta\omega\Delta t = 4\ln(2), \text{ or} \tag{A3.11}$$

$$\Delta\nu\Delta t = \frac{2\ln(2)}{\pi} \approx 0.44 \tag{A3.12}$$

here $2\pi\nu = \omega$. Thus, using the relation above it is easy to estimate the pulse duration FWHM of the bandwidth-limited pulse to the corresponding Gaussian spectrum. The same relation can be written in terms of the wavelength instead of the frequency using the following estimation. In the case of the middle wave length being much larger than the spectral bandwidth $\lambda >> \Delta\lambda$:

$$\Delta\omega = \omega_2 - \omega_1 = \frac{c}{2\pi}\left(\frac{1}{\lambda_2} - \frac{1}{\lambda_1}\right) = \frac{c(\lambda_1 - \lambda_2)}{2\pi\lambda_2\lambda_1} \approx -\frac{c\Delta\lambda}{2\pi\lambda^2}$$

$$\left|\Delta\lambda\Delta t\right| = \frac{2\lambda^2\ln(2)}{\pi c} \approx \frac{\lambda^2}{c}0.44$$

where λ_1, λ_1 and ω_1, ω_2 are the wavelengths and frequencies corresponding to the half of the peak intensity in the Gaussian spectral intensity distribution of the pulse (Figure A3.II).

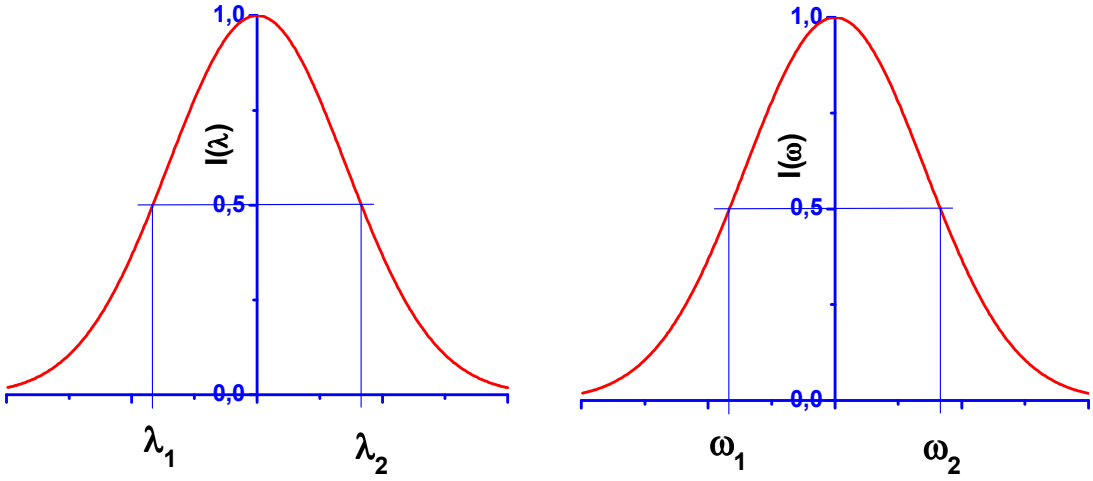

Figure **A3.II** Wavelengths λ_1, λ_1 and frequencies ω_1, ω_2 corresponding to the half of the peak intensity in the Gaussian spectral intensity distribution.

In case of the fundamental pulses (λ=800nm) the product

$\Delta\lambda\Delta t$ = 938 nm fs,

in case of the SH pulse (λ=400nm) this product is four times smaller.

$\Delta\lambda\Delta t$ = 234.5 nm fs.

Appendix A4

Autocorrelators

The main idea behind the autocorrelator is to scan the pulse with itself. Thus in the autocorrelator of the second order the pulse is divided into two equal pulses with the help of a beam splitter (see the figure A4.I). Further, two pulses are focused in a nonlinear crystal (for instance KDP). The intensity of the generated non-collinear second harmonic, which is proportional to the product of the electric fields of the incident beams, is recorded as a function of the delay time between the two focused pulses.

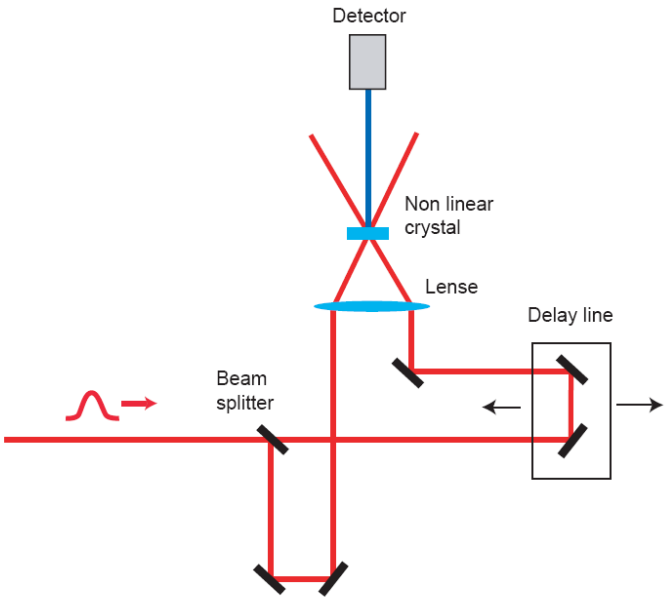

Figure **A4.I** Scheme of the autocorrelator of the second order

The autocorrelator of the third order works in a similar way to the autocorrelator of the second order. But one of the pulses is converted to the second harmonic (SH) before focusing in the nonlinear crystal, see figure A4.II. Since the polarisation of the generated SH pulse is perpendicular to the polarisation of the fundamental pulse, one λ/2 platelet is installed in order to provide both pulses with the same polarisation. In this case the intensity of the non-collinear harmonic of the third order is measured as a function of the delay time between the focused SH and the fundamental pulses.

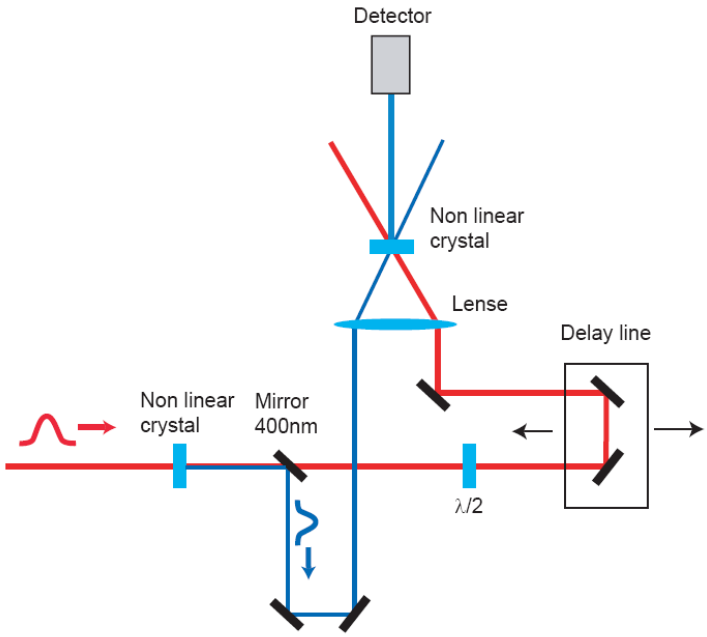

Figure **A4.II** Scheme of the autocorrelator of the third order

Appendix A5

Stretcher and compressor of the T³ laser

There are several ways to construct compressors and stretchers. A typical Ti:Sa-based chirped-pulse amplifier requires the pulses to be stretched to several hundred picoseconds. This means that the different wavelength components must experience about 10 cm difference in a path length. The most practical way to achieve this is to use grating-based stretchers and compressors.

Stretchers and compressors are characterized by their dispersion. With negative dispersion, light with higher frequencies (shorter wavelengths) takes less time to travel through the device than light with lower frequencies (longer wavelengths). With positive dispersion, it is the other way around. In a CPA, the dispersions of the stretcher and compressor should cancel out. For practical reasons, the stretcher is usually designed with positive dispersion and the compressor with negative dispersion.

Each component in the whole chain from the oscillator to the output of the compressor contributes to the dispersion.

Figure A5.I A) shows the simplest grating configuration, where long-wavelength components pass a larger distance than the short-wavelength components (negative dispersion). Often, in this arrangement only two gratings and an extra mirror (or retro reflector), placed at the position marked by the vertical line in figure A5.I A) are used, see figures A5.I B and A5.III. In this way the beam hits each grating twice instead of once. This setup is normally used as a compressor, since it does not involve components that could lead to unwanted side-effects when dealing with high-intensity pulses. The dispersion can be tuned easily by changing the incidence angle on the gratings and the distance between the gratings (figure A5.I B).

Figure A5.II A) shows a more complicated grating configuration that involves focusing elements, here depicted as lenses. The lenses are placed at a distance 2f from each other (they act as a 1:1 telescope), and at a distance L from the gratings. If $L < f$ the setup acts as a positive-dispersion stretcher and if $L > f$, it is a negative-dispersion stretcher. The case $L = f$ is used in the pulse shaper. With the additional mirror placed at the position marked by the vertical black line (figure A5.II A) it is possible to use two instead of four gratings (figure A5.II B). Further simplification can be achieved by installing one more mirror in

the focus of the first lens and replacing the lenses by a spherical mirror (figures A5.II C and A5.IV).

This setup requires the beam diameter to be very small compared with the length of the telescope; otherwise undesirable aberrations will be introduced. For this reason, it is normally used as a stretcher before the amplification stage, since the low-intensity pulses can be collimated to a beam with a small diameter.
The material in this section is based on [69].

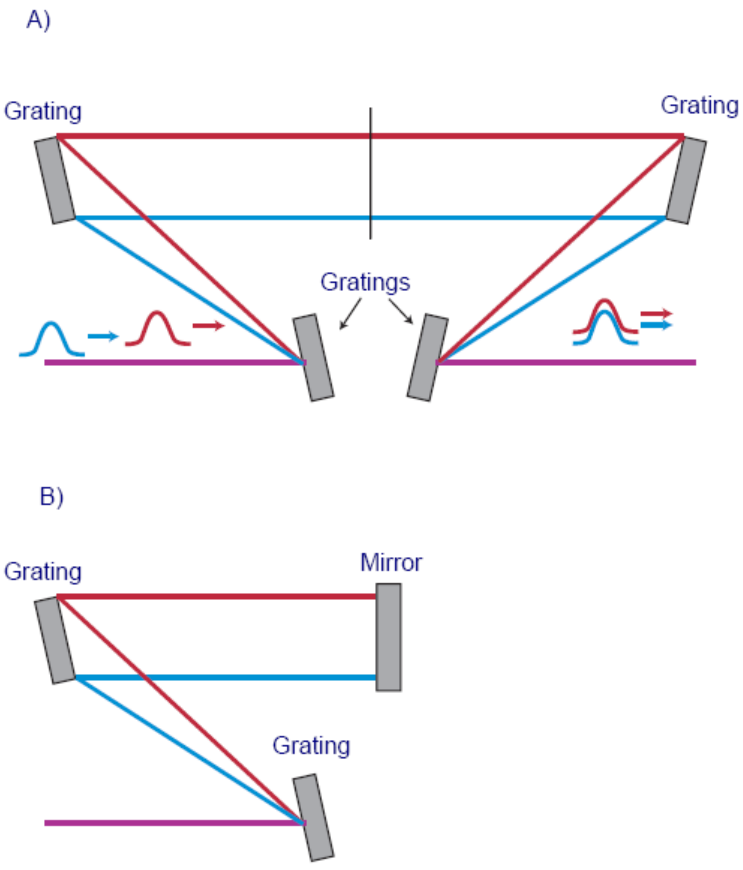

Figure **A5.I** Working principle of compressor

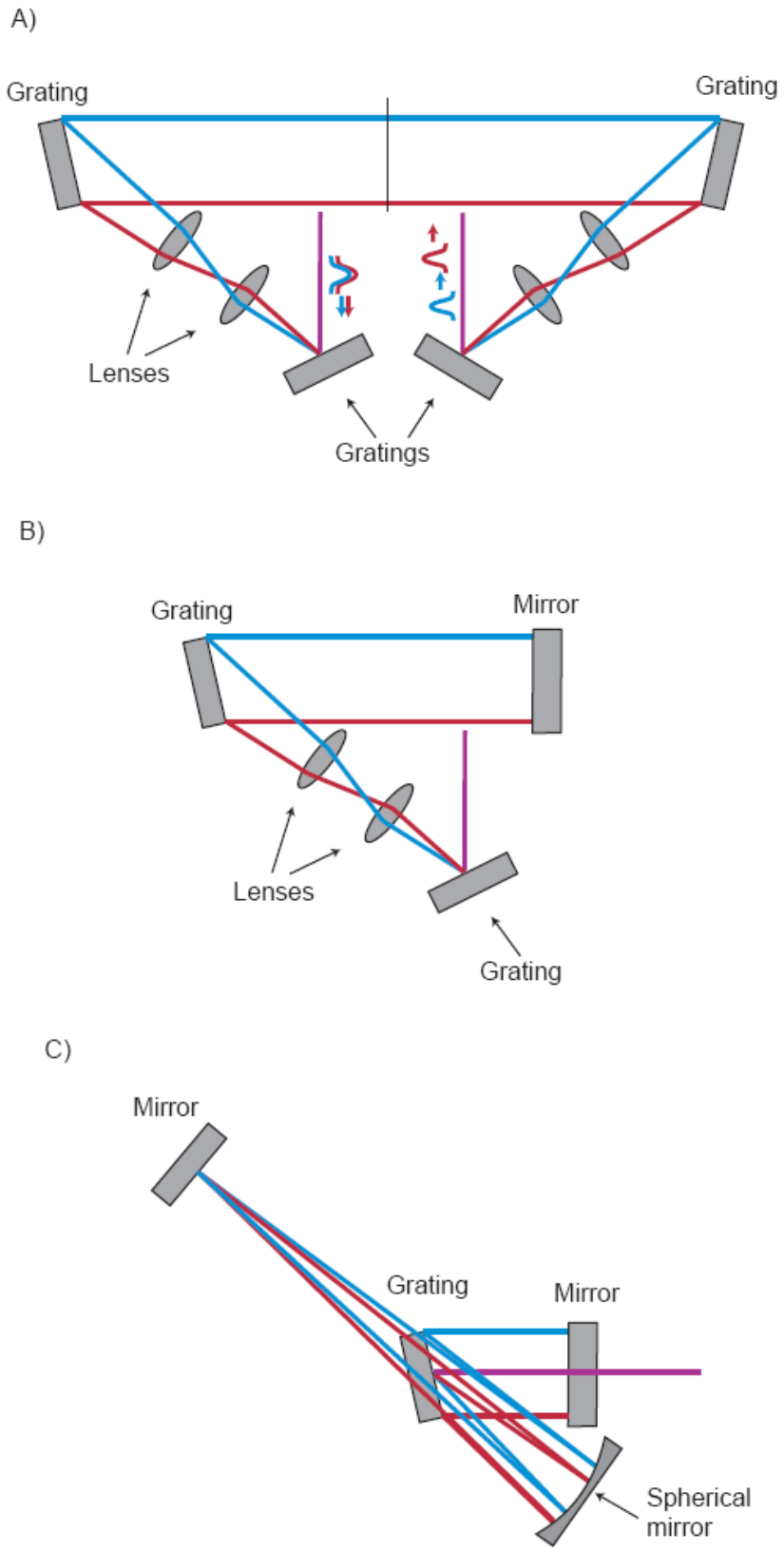

Figure **A5.II** Working principle of stretcher

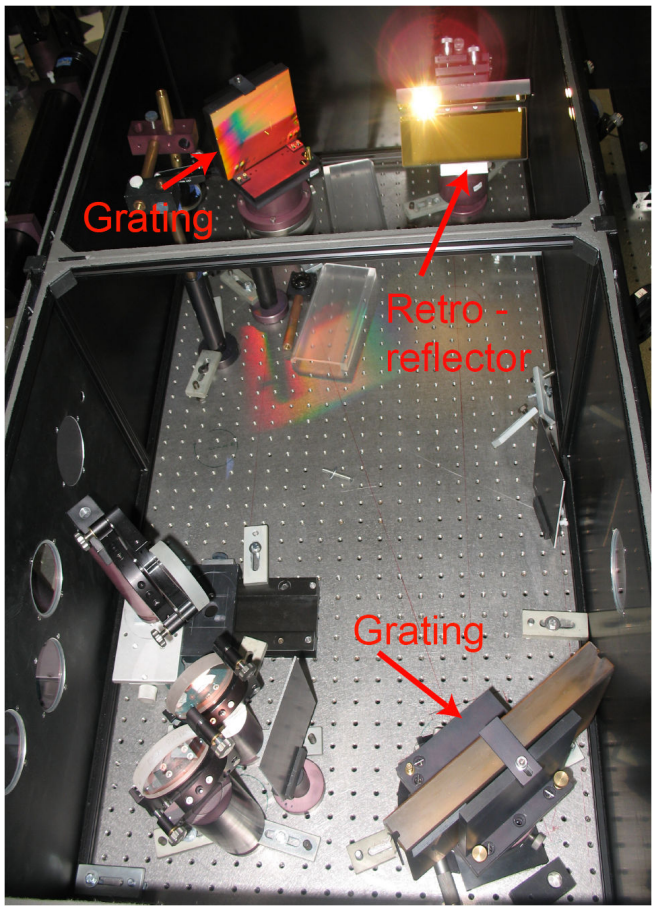

Figure **A5.III** Compressor of the T³ laser system at the IEP

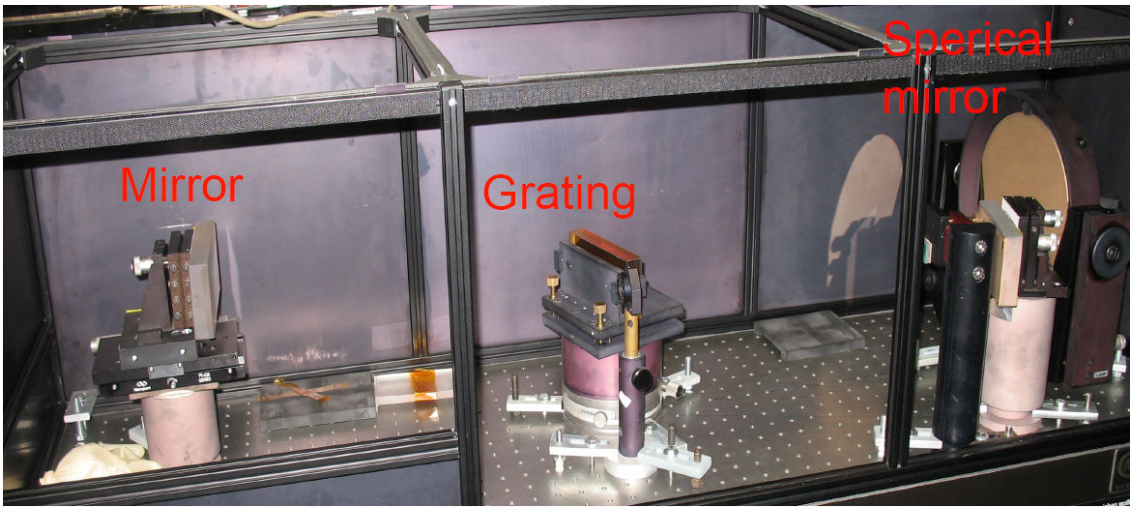

Figure **A5.IV** Stretcher of the T³ laser system at IEP

Appendix A6

Wave front aberrations

The flat or aberrations-free wave front of the beam is a necessary condition for diffraction limited focusing.

An arbitrary wave front can be represented with the help of a series of Zernike polynomials. The Zernike series representation of a wave front is extremely convenient, instructive, and a helpful aid in the analysis of perturbed wave fronts. In particular, the Zernike series representation is useful for providing explicit expressions for the well-known low-order wave front aberrations such as coma, astigmatism, defocus, and so on. This turns out to be an appealing way of converting the often large and inscrutable wave front expressions into tidy, intuitively understandable results. In general, the $m = \pm 1$ terms correspond to coma, and the $m = \pm 2$ terms correspond to astigmatism. Zernike circle polynomials represent a complete orthogonal set over the interior of the unit circle. Hence an arbitrary function $W(\rho,\Theta)$, where radius ρ is restricted to the range $0 < \rho < 1$, may be completely represented by an infinite series of Zernike polynomials.

See Murison [68] for a discussion, including determination of the coefficients and examples. See also Born and Wolf [65] and Zernike [66] for more information on Zernike polynomials.

Some of the wave front aberrations and the corresponding Zernike polynomials representation $Z_n^m(\rho,\Theta)$ are listed in figure A6.I and illustrated in figure A6.II. ρ and Θ denote the radius and the angle in the polar coordinates, respectively.

mode	order	frequency		
j	n	m	$Z_n^m(\rho,\theta)$	Meaning
0	0	0	1	Constant term, or Piston
1	1	-1	$2\rho\sin(\theta)$	Tilt in y - direction, Distortion
2	1	1	$2\rho\cos(\theta)$	Tilt in x - direction, Distortion
3	2	-2	$\sqrt{6}\rho^2\sin(2\theta)$	Astigmatis m with axis at $\pm 45^\circ$
4	2	0	$\sqrt{3}(2\rho^2-1)$	Field curvature, Defocus
5	2	2	$\sqrt{6}\rho^2\cos(2\theta)$	Astigmatis m with axis at 0° or 90°
6	3	-3	$\sqrt{8}\rho^3\sin(3\theta)$	
7	3	-1	$\sqrt{8}(3\rho^3-2\rho)\sin(\theta)$	Coma along y - axis
8	3	1	$\sqrt{8}(3\rho^3-2\rho)\cos(\theta)$	Coma along x - axis
9	3	3	$\sqrt{8}\rho^3\cos(3\theta)$	
10	4	-4	$\sqrt{10}\rho^4\sin(4\theta)$	
11	4	-2	$\sqrt{10}(4\rho^4-3\rho^2)\sin(2\theta)$	Secondary Astigmatis m
12	4	0	$\sqrt{5}(6\rho^4-6\rho^2+1)$	Spherical Aberration, Defocus
13	4	2	$\sqrt{10}(4\rho^4-3\rho^2)\cos(2\theta)$	Secondary Astigmatis m
14	4	4	$\sqrt{10}\rho^4\cos(4\theta)$	
⋮	⋮	⋮	⋮	

Figure **A6.I** List of Zernike polynomials. Table is taken from [67]

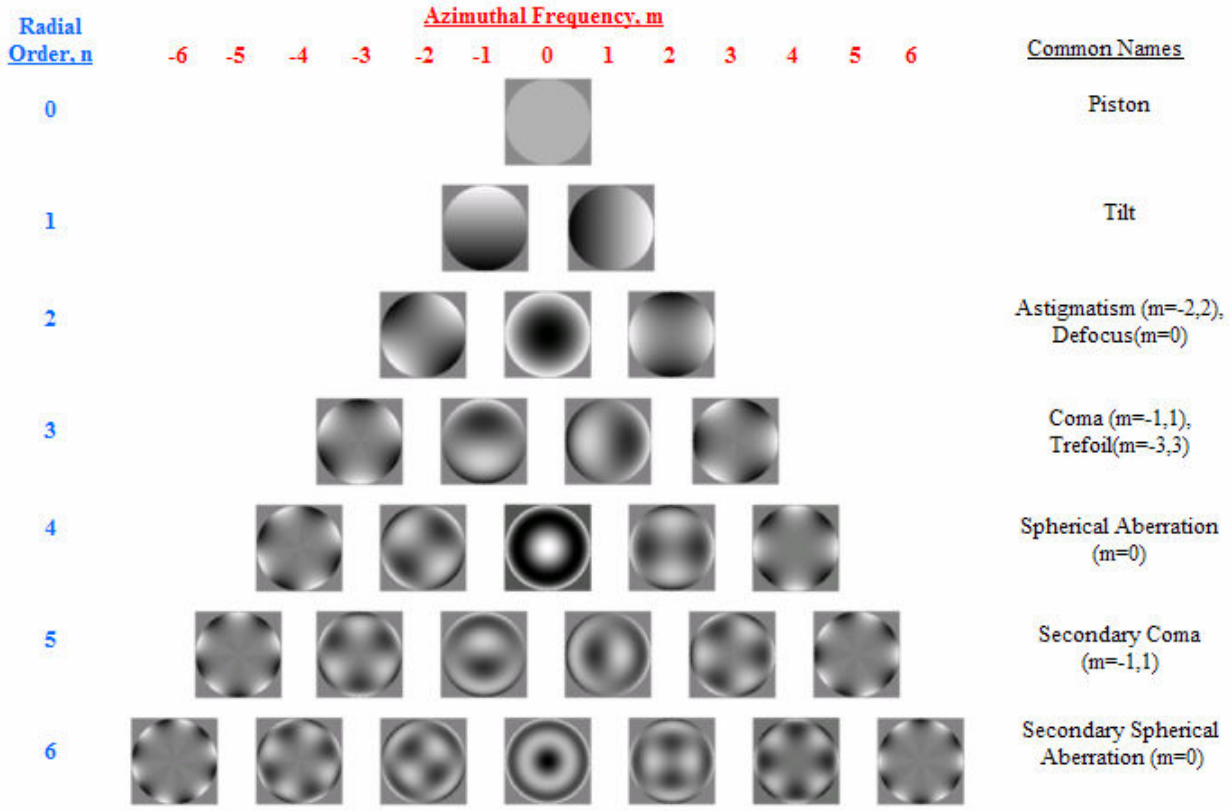

Figure **A6.II** Illustration of the Zernike polynomials and corresponding wave front aberrations. Figure is taken from [67].

Appendix A7

Four mirror polarizations flipper

The "four mirrors polarization flipper" is an arrangement of four mirrors which flips the polarization of the incident beam from horizontal to vertical and vice versa.

For the illustration of the "four mirror polarizations flipper" let us consider the horizontally polarized (in the X direction) beam which propagates in the Y direction (figure A7.I). After reflection from the first mirror (M1) this beam propagates down (in the negative Z direction), the polarization is still in the X direction. Further, the Mirror M2 reflects the considered beam in the X direction. Now the polarization is vertical (in the Z direction). The third (M3) mirror reflects the beam up (in the Z direction) and the polarization is turned to the X direction. After the last reflection (on the mirror M4) the beam is vertically polarized (in the Z direction) and propagates in the X direction. The polarization flipper at the IEP is presented in figure A7.II.

In the case of a vertically polarized incident beam it works analogously.

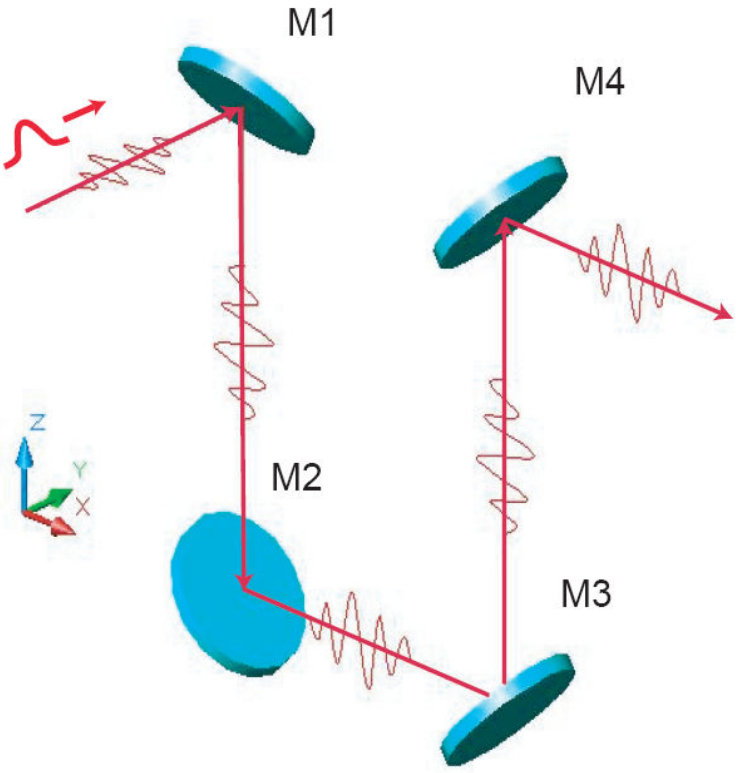

Figure **A7.I** Scheme of the "four mirror polarisation flipper"

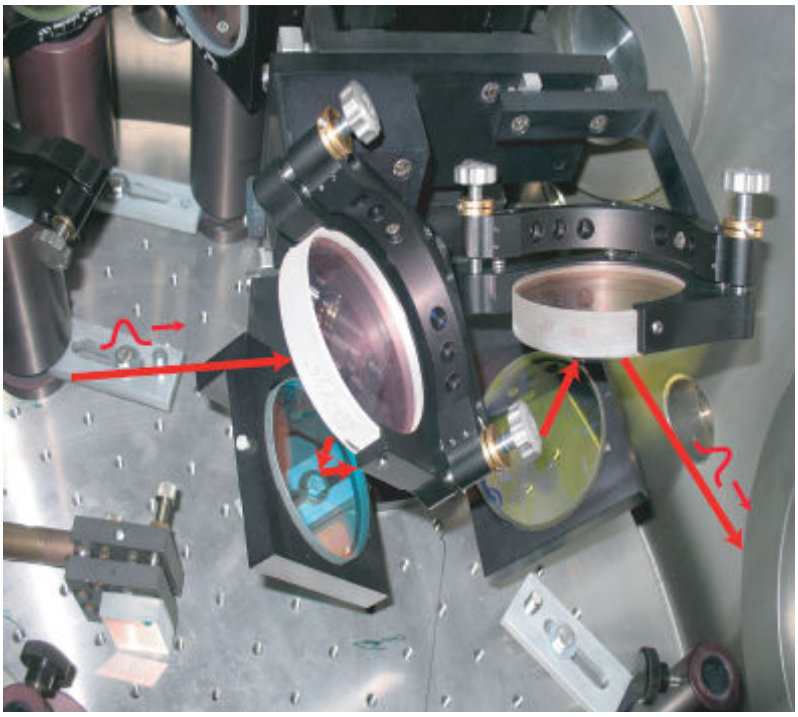

Figure **A7.II** Four mirror polarisation flipper installed in the adaptive optics chamber at the IEP

Appendix A8

Calculation of the diffraction limited focal spot of the parabolic mirror

Assuming the Gaussian beam profile, the electric field dependence on the radius r is given by relation

$$E(r) = E_0 e^{-\frac{r^2}{\sigma^2}} \quad . \tag{A8.1}$$

σ is a positive constant. The corresponding intensity dependence is

$$I(r) = I_0 e^{-\frac{2r^2}{\sigma^2}} \tag{A8.2}$$

Using the relation (A8.2) the FWHM diameter R can be defined,

$$\frac{1}{2} I_0 = I_0 e^{-\frac{2(R/2)^2}{\sigma^2}} \tag{A8.3}$$

and consequently the relation between R and σ

$$\sigma\sqrt{2\ln 2} = R \tag{A8.4}$$

is obtained. According to the references [70-72] for the Gaussian beam the dependence (A8.5) is valid.

$$\sigma(z) = \sigma_0 \sqrt{1 + (\frac{\lambda z}{\pi \sigma_0^2})^2} \tag{A8.5}$$

z is the distance from the position with the smallest beam "diameter" ($\sigma(0) = \sigma_0$) along the symmetry axis (z-axis) of the beam. In the case of $z >> \sigma_0^2/\lambda$ the (A8.5) can be written as:

$$\sigma(z) = \frac{\lambda z}{\pi \sigma_0} \tag{A8.6}$$

Using (A8.4) the relation (A8.6) can be expressed in terms of the FWHM values R.

$$R(z) = \frac{\lambda z}{R_0}\frac{2\ln 2}{\pi} \qquad \text{(A8.7)}$$

To use the dependence (A8.7) for the calculation of the diffraction limited focal spot, the distance z has to be replaced by the focal length (f = z). The values R(f) and R_0 can be interpreted as the intensity FWHM of the beams before focusing and in the focal plane, respectively.

For the numerical calculation of the intensity distribution in the focal plane of the ideal parabolic mirror, the geometry illustrated in figure A8.I is used. The incident beam which is assumed to be with the flat wave front and the Gaussian beam profile propagates in the negative "Z" direction, towards the parabolic mirror. The incident beam is divided into a large number of "sub beams" with the corresponding intensity (black vertical lines). Each point on the parabolic mirror which is illuminated by a sub beam is assumed to be an origin of the spherical wave according to the Huygens – Fresnel principle. To obtain the electric field E in each point of the focal plane, the contributions of all spherical waves are summed up. Note, here the phase of the individual wave plays a key role. The intensity in each point is calculated using the relation $I = |E|^2$.

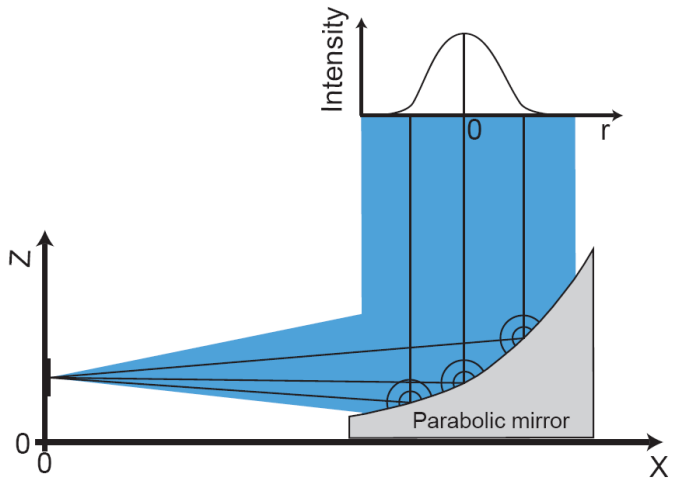

Figure **A8.I** Geometry used in the calculation of the intensity distribution in the focal plane of the parabolic mirror.

In the “Matlab” routine the following parameters are used:

Beam aperture	50 mm
Beam width (intensity FWHM)	15 mm
Wave length	400 nm
Number of sub beams	30 x 30
Incident beam position X (effective focal length)	76 mm
Observed area in the focal plane	6x6 µm²
Number of points in the plane	150x150
Parameter of the parabolic mirror	1/203.2 mm^{-1}

In conclusion of Appendix A8 the “Matlab” code is presented:

```
clear all;

% General parameters
lambda=4.0e-4;              % in mm Wavelength
K=2*pi/lambda;
a=1/203.2;                  % in 1/mm parameter of the parabolic mirror

% Incident beam parameters
b_apertur=50;               % in mm beam aperture in mm
I_FWHM=15;                  % in mm (intensity) width FWHM of beam profile
N_beams=30;                 % # of sub beams
x_middle=76;                % in mm the X coordinate of the middle of the beam

% Focal plane parameters

interval=0.006;             % in mm length and width of the observed area in the focal plane
XB=0;                       % in mm position of the middle of the focal plane
YB=0;
ZB=50.8;
N_points=150;               % # of points in the interval


Gauss_w=I_FWHM/sqrt(2*log(2));     %in mm Width of the incident beam (electric field)
Gauss_a=1;

dr=b_apertur/N_beams;
db=interval/N_points;

xb=XB;

for m=1:N_points
   yb=YB-interval/2+m*db;

   m

   for n=1:N_points
      zb=ZB-interval/2+n*db;
      feld(m,n)=0;

      for i=1:N_beams


         for k=1:N_beams
```

```
            x=x_middle-b_apertur/2+k*dr;

            y=-b_apertur/2+i*dr;

            P(i,k)=a*(x^2+y^2);

            G(i,k)=Gauss_a*exp( -((x-x_middle)^2 + y^2) / Gauss_w^2);        % electric field!

            opt_weg=sqrt((x-xb)^2+(y-yb)^2+(P(i,k)-zb)^2);                   % optical path

            Phase_ges(m,n)=K*(opt_weg-P(i,k));

            feld(m,n)=feld(m,n)+(G(i,k)/opt_weg)*exp(-j*Phase_ges(m,n));

            intensity(m,n)=feld(m,n)*conj(feld(m,n));
          end
       end
    end
end

I_max=max(intensity);
Imax2=max(I_max)
intensity=intensity/Imax2;



figure;
surfl(-(interval-db)*500:db*1000:+(interval-db)*500,-(interval-db)*500:db*1000:+(interval-
db)*500,intensity);
axis([-interval*500 interval*500 -interval*500 interval*500 0 1]);
xlabel('z in µm');
ylabel('y in µm');
zlabel('Intensity');
%colorbar;
%grid off;
%axis off;
shading interp;
colormap copper;
```